UNIVERSITY OF TOKYO

An exclusive study of the Supersymmetric model using a novel soft tau identification method with the ATLAS detector

Mark Musashi Hashimoto

A thesis submitted in partial fulfillment for the degree of Master of Science

in the
Graduate School of Science

February 2010

Abstract

Mark Musashi Hashimoto

This thesis presents an exclusive analysis of the mSUGRA coannihilation region di-tau "golden" decay chain using Monte Carlo simulations of the ATLAS detector. The aim of the analysis is to reconstruct the invariant mass distribution of the two taus which arise from this chain, $M_{\tau,\tau}$, and to estimate the distribution's endpoint. The determination of this endpoint is very important for ascertaining whether the mSUGRA coannihilation region is the correct description of the universe, and then for determining the model's parameters. The first tau of this decay chain is relatively hard and it is efficiently reconstructed by the standard ATLAS tau reconstruction algorithm. On the other hand the second tau is very soft, and as such it is inefficiently reconstructed due to the algorithms' relatively high seed thresholds and stringent identification requirements. We develop a new analysis specific method for reconstructing this soft tau which employs a number of novel techniques, and which is optimised for the low energy region. We find that by using the two algorithms to reconstruct the respective taus, we are able to reconstruct the $M_{\tau,\tau}$ endpoint better than by simply using the ATLAS algorithm for both of them. We obtain a final result of $M_{\tau,\tau\, endpoint} = 58 \pm 16$ (stat) ± 5 (sys) GeV at the ATLAS coannihilation reference point with $E_{CM} = 10$TeV and an integrated luminosity of 63 fb^{-1}.

Acknowledgements

First and foremost I would like to offer sincere thanks to my project supervisor Tomio Kobayashi for giving me the opportunity to perform this research at ICEPP. It has been a very edifying experience and I will take with me a great number of lessons and new skills. My deep thanks also to Shoji Asai for his many hours of discussions and directions which helped to shape the path of this research. I would like to express my gratitude to Naoko Kanaya for putting up with many-a-tiring email from me, and who was also very helpful to me on my visits to CERN. Thanks also to Junichi Tanaka for his many suggestions and helpful discussions and to Toshio Namba for early instruction in the details of experimental physics. I would also like to thank Tetsuro Mashimo who was very helpful to me with with the details of the ICEPP computing system. Finally for the people at ICEPP I would like to thank my fellow students for help with technical details of ATLAS analysis, and for generally helpful discussions about physics, and also the ICEPP secretaries for making the day-to-day run so smoothly.

This research was performed in collaboration with a number of colleagues at Freiburg University. I would like to express my gratitude to Karl Jakob, Michel Janus, Xavier Portell and Jochen Dingfelder for many useful discussions and suggestions. I would like to give particular thanks to Stan Lai for his enthusiastic help and support over the period of this research.

During my time in Japan I was supported financially by a scholarship from the Japanese Ministry of Education, Culture, Sport, Science and Technology (MEXT). I would like to offer my thanks for this opportunity to study in Japan.

Last but certainly not least my deep gratitude to my family. Their unwavering support for me is the reason that I am at this point. Also, thank you to my Phoebe. It would have been a much steeper road without you.

Contents

List of Figures

List of Tables

Abbreviations

AOD	**A**nalysis **O**bject **D**ata
ATLAS	**A** **T**oroidal **L**HC **A**apparatu**S**
ATLFAST	**ATL**as **FAST** simulation
BG	**B**ack**G**round
CERN	**C**onseil **E**uropéen pour la **R**echerche **N**ucléaire
	(European Organisation for Nuclear Research)
CERN	**A** **T**oroidal **L**HC **A**apparatu**S**
CSC	**C**athode **S**trip **C**hambers
CSC	**C**omputer **S**ystem **C**ommisioning
DAQ	**D**ata **A**c**Q**uisition
EM	**E**lectro**M**agnetic
ESD	**E**vent **S**ummary **D**ata
GUT	**G**rand **U**nified **T**heory
LAr	**L**iquid **Ar**gon
LEP	**L**arge **E**lectron **P**ositron collider
LHC	**L**arge **H**adron **C**ollider
LLH	**L**og **L**ikeli**H**ood
LSP	**L**ightest **S**upersymmetric **P**article
MDT	**M**onitored **D**rift **T**ubes
MSSM	**M**inimal **S**upersymmetric **S**tandard **M**odel
mSUGRA	**m**inimal **S**uper**GRA**vity (model)
NLSP	**N**ext to **L**ightest **S**upersymmetric **P**article
OS	**O**pposite **S**ign
PDF	**P**robability **D**istribution **F**unction
QCD	**Q**uantum **C**hromo**D**ynamics

QED	**Q**uantum **E**lectro**D**ynamics
RPC	**R**esistive **P**late **C**hambers
SCT	**S**emi**C**onductor **T**racker
SS	**S**ame **S**ign
SUSY	**SU**per**SY**mmetry
TGC	**T**hin **G**ap **C**hambers
TRT	**T**ransition **R**adiation **T**racker
VEV	**V**acuum **E**xpectation **V**alue
WMAP	**W**ilkinson **M**icrowave **A**nisotropy **P**robe

For my Poppa

Chapter 1

Theory and Motivation

For the few hundred years since the birth of Science scientists have striven for ever deeper intuition and understanding of the mechanisms which give rise to the observed dynamics of the universe, backed up by a rigorous and uncompromising demand for experimental verification. The story of science, and in particular of the fundamental studies of physics, has been a ever deepening probe in to the structure of the material universe and the dimensions within which it manifests.

It has also been a story which may begin with the study of individual and seemingly disparate phenomena, but always leads to a deeper and more general understanding of the ways in which these seemingly unrelated phenomena , at their base, follow the same patterns which arise from the same general laws. It is a story of descriptions of very limited scope, being combined or generalised to a description of more general applicability.

The standard model of particle physics as developed and rigorously tested in the latter half of the twentieth century is the culmination of these efforts, and describes to an extreme accuracy a great deal of the structures and dynamics of the universe. At the same time it is widely agreed that this theory can not be a “final” description of the universe. It’s most blaring emission is any mention of the force with which the whole enterprise of physics began, gravity. Besides this though there are a number of other unsatisfactory aspects to the theory which are signs that the path is wide open for the next step in the development of particle physics. This new physics is expected to manifest at the newest generation particle accelerator facility at CERN, the Large Hadron Collider (LHC), thus it is widely predicted that the next tens of years will yield a new paradigm for particle physics development.

This chapter will begin with a general description of the standard model which will culminate with a discussion of its deficiencies which are the motivation for the quest for a new theory. This will lead on to the discussion of one of the most promising theoretical candidates for beyond-the-standard-model physics, so-called “supersymmetry”. The focus will be on the minimal gravity mediated version of the theory, and also only on a particular region of its parameter space, the so-called coannihilation region. This will set the context for the next chapter which is devoted to the discussion of the Large Hadron Collider experiment, and one of it multi-purpose detectors, the ATLAS detector.

1.1 The Standard Model

1.1.1 Overview

The standard model (SM) of particle physics was developed in the 1970s and is a theory which describes the structure and dynamics of the fundamental constituents of matter by combining two of the most important breakthroughs of the early twentieth century, namely special relativity and quantum mechanics. The result is a description of both matter and the forces which govern them in terms of point like particles (matter) exchanging other point like particles (the forces). The theory predicts that these particles possess an internal degree of freedom which exhibits many of the properties of angular momentum, and thus is named “spin”. The amount of spin which the particle possesses determines whether it is a matter particle, or “fermion” (half integer spin), or a force particle, or “boson” (integer spin).

It is understood that in the present universe there are four distinct forces which mediate all interactions of matter: The so-called strong and weak forces, which, due to their extremely short range are unfamiliar to our everyday experience, and the electromagnetic force and gravity. The SM is actually an internally consistent combination of two so-called “gauge field theories”, quantum chromodynamics (QCD) which describes the strong force, and quantum electroweak theory, which is a unified description of the electromagnetic and weak forces. As mentioned above the SM does not describe the gravitational force and *its* best description is still Einstein’s theory of general relativity, which is laid out in a seemingly completely distinct formalism to its standard model counterparts.

One subtlety of the SM is in its description of mass. Directly incorporating mass terms in to the SM Lagrangian breaks its gauge invariance resulting in a theory with diverging parameters which are not recoverable through renormalisation. It is obvious that particles indeed do have mass though and so a different mechanism is required to describe it

Generation	1	2	3	Charge	Mass
Leptons	$\begin{pmatrix} e \\ \nu_e \end{pmatrix}$,	$\begin{pmatrix} \mu \\ \nu_\mu \end{pmatrix}$,	$\begin{pmatrix} \tau \\ \nu_\tau \end{pmatrix}$	-1 0	511keV, 105.7MeV, 1.78GeV < 2eV
Quarks	$\begin{pmatrix} u \\ d \end{pmatrix}$,	$\begin{pmatrix} c \\ s \end{pmatrix}$,	$\begin{pmatrix} t \\ b \end{pmatrix}$	$+2/3$ $-1/3$	$1.5 - 3.3$MeV, 1.27GeV, 171.3GeV $3.5 - 6.0$MeV, 105MeV, 4.20GeV

TABLE 1.1: The Standard Model particles listed by lepton/quark category, and by generation, and grouped in to their doublets. The electric charge and the masses of the particles are included. [1]

within the theory. The best candidate for this is the so-called Higgs mechanism whereby particles gain mass through so-called "spontaneous symmetry breaking".

The standard model has been extremely rigorously tested over the past few decades at ever higher energy particle accelerators and other experiments, and the result of every test has found to be consistent with it.

1.1.2 Matter and Forces

The fermions of the SM can be distinctly divided in to two categories: those which feel the strong force (quarks) and those which don't (leptons). These are further subdivided in to three so-called generations with each successive generation having larger and larger masses. The origin of this three generation structure is not understood and is one of a number of unsatisfactory (though not invalidating) aspects of the SM. The second and third generations are inherently unstable and decay very quickly to the first generation meaning that virtually all of the matter in the universe is composed of the first generation fermions. The matter particles grouped by category and generation are shown in Table 1.1

As alluded to above the standard model is a "gauge theory" of matter and forces. Forces naturally arise out of the gauge formalism when the Lagrangian that describes the matter field is required to be invariant under certain local transformations. The forms of these transformations are not necessarily self-evident but have been motivated by experiment. Here a local transformation means that the transformation is space-time dependent.

The simplest example to consider is the local $U(1)_Q$ gauge transformation for the QED electron field, where the Q denotes that the conserved quantity in the interaction is the electric charge. The form of this transformation is $\psi \rightarrow e^{i\theta(x)}\psi$, where the x dependence makes explicit the local nature of the transformation. This particular transformation corresponds to a simple local rotation of the phase of the electron field. In order to maintain the invariance of the Lagrangian under this rotation a term is added which describes an interaction with a massless boson, a so-called "gauge boson". This boson turns out to be the photon which is the mediator of the electromagnetic interaction. The interaction of matter and forces thus arises very naturally out of a symmetry of the Lagrangian.

A similar procedure is followed for deriving the weak interaction, except that this time the fermions are grouped in to so-called doublets (see Table 1.1). These doublets share a similar behaviour under the weak interaction so that, for example, a charged lepton can emit or absorb a W boson and convert in to the corresponding neutrino. The analogue of electric charge for the weak interaction is the "weak isospin", which is conserved in the interaction. The gauge transformation for the weak interaction is SU(2), and the result this time is three vector bosons. Of particular interest for the weak formalism is the vector-axial form of the interaction, $\frac{1}{2}(1-\gamma_5)$, which only selects the left handed components of the particles (right handed components of anti-particles) , thus violating the parity symmetry.

The unification of the electromagnetic and weak interaction is achieved by requiring invariance of the Lagrangian under the gauge group $SU(2)_L \times U(1)_Y$, where the subscript L makes explicit that only the left handed components of the particles transform under $SU(2)$ and the subscript Y indicates that the $U(1)$ transformation of this unified electroweak group is not the same as the QED group discussed above, and the conserved quantity is the so-called "weak hypercharge" (Y). This procedure results in 4 massless vector bosons, $W_\mu^{1,2,3}$ coming from the $SU(2)_L$ symmetry group and B_μ coming from the $U(1)_Y$ group.

The strong force only affects the quark sector of the SM particles and it conserves so-called "colour" charge. Each quark (anti-quark) listed in Table 1.1 comes in three varieties of this colour. Their interaction arises from imposing invariance under the $SU(3)$ symmetry group. From this arises the eight massless QCD gluons which mediate the strong force between the quarks. Of particular interest is the non-observation of free quarks or gluons which leads to the idea of "colour confinement", the mechanism by which quarks are bound in to colourless hadrons.

1.1.3 Mass and the Higgs mechanism

Up to this point we have only discussed gauge particle theory in terms of massless fermions and bosons. Of course many of the fermions and bosons do have mass and in particular, the masses of the vector bosons which mediate the weak force have been shown through precise measurements at the Super Proton Synchrotron (SPS) collider in the 1980s to be rather large. A naive approach for generating masses for the weak bosons would be to explicitly add mass term for them to the Lagrangian. Such mass terms in the Lagrangian do not respect the $SU(2) \times U(1)$ gauge symmetry and lead to a non-renormalisable theory.

A different approach is to generate mass through the so called "Higgs Mechanism". The basic idea of this approach is to introduce mass terms in to the Lagrangian byway of introducing a new field, which is an $SU(2)$ doublet (and as such has four degrees of freedom). This field has a potential of the form

$$V(\Phi) = -\mu^2 \Phi_i^\dagger \Phi^i + \lambda(\Phi_i^\dagger \Phi^i)^2 \tag{1.1}$$

$(\mu^2, \lambda > 0)$ which has a local maxima at $\Phi = 0$ and thus a non-zero vacuum expectation value. Instead there are infinite degenerate minima of the potential at $\Phi^\dagger \Phi = \frac{1}{2}\mu^2/\lambda$. This is the famous "Mexican hat" potential. "Spontaneous symmetry breaking" occurs when we choose a particular minimum around which to perform the expansion of Φ. Reinserting this expansion in to the Lagrangian turns out to result in one of the degrees of freedom of the Higgs field becoming a massive boson of mass $M_H = \sqrt{2}\mu$ [1] . The remaining degrees of freedom mix with the massless electroweak vector bosons to result in 3 massive weak vector bosons ($W^\pm$ and Z) and the massless electromagnetic boson (the photon).

The masses of the W bosons are predicted to be

$$m_W = g_2 \nu / 2 \tag{1.2}$$

where g_2 is the coupling strength of the bosons W_μ^i, and $\nu = \mu/\sqrt{\lambda}$. The mass of the Z boson is related to m_W via

$$m_Z = m_W / \cos\theta_W \tag{1.3}$$

where $\tan\theta_W = g_1/g_2$ is the ratio of the coupling constants for the bosons B_μ and W_μ^i. θ_W, or the Weinberg angle, is a measure of the amount of mixing between B_μ and W_μ^3. This ratio is one of the predictions of the Higgs theory which it has been possible to test (though the Higgs boson itself is still elusive).

The generation of mass for the massive fermions is achieved by adding so-called Yukawa terms to the Lagrangian of the form

$$\mathcal{L}_{yukawa} = -G_e \overline{e}_L^i \Phi_i e_R + \text{h.c.} \tag{1.4}$$

[1] μ is a free parameter of the theory and as such the Higgs mass is not determined.

where h.c. denotes the hermitian conjugate. This is an interaction between the left handed electron doublet, the right handed electron and the scalar doublet Φ_i. G_e is a coupling constant which parameterises the strength of the interaction and is determined by experiment. Substituting the expansion of the Higgs field in to the above equation yields mass terms like $-G_e \nu/\sqrt{2} \times \bar{e}e$ where we can see that the mass of the fermion is proportional to the Yukawa coupling G_e. Thus we see that the strength of the Higgs coupling for fermions is proportional to the mass of the fermions (square of masses for vector bosons) which is a characteristic feature of the Higgs coupling.

1.1.4 The tau lepton

Of particular importance to this study is the SM tau lepton (symbol τ) so some details of it follow. The tau is the 3rd generation equivalent of the electron and similarly has a corresponding neutrino ν_τ. The tau itself was discovered in 1975 by Martin Lewis Perl *et al.* at the SPEAR electron-positron collider ring at SLAC using the LBL magnetic detector [2]. The current combined experimental value of its mass is 1776.84 ± 0.17 MeV while its mean lifetime is $(290.6 \pm 1.0) \times 10^{-15}$ s ($c\tau = 87.11 \mu$m) [1]. This appreciable lifetime means that the decay length significance is expected to be appreciable at the ATLAS detector, and measurements of it are expected to help to discriminate taus from background objects (see Section 4.2.7.3).

The large mass of the tau means that it is the only lepton which can decay to hadrons, and as such it has a rich spectrum of decay modes. The main decay modes are listed in Table 1.2 but they can be succinctly summarised as follows. All tau decays are via the weak interaction and in order to conserve lepton number a tau neutrino always results which escapes detection. The tau goes to leptons about one third of the time (half muon, half electron) while the remaining two thirds go to hadrons. As will be described in Section 4.2.7.1 it is these hadronic modes which are the measured signal for most tau measurements at ATLAS. Of these about 70% are so called "single prong" where the tau decays to a single $\pi^\pm$ plus some number of π^0, while 21% are "three prong" where the tau decay to 3 $\pi^\pm$ plus some number of π^0. There are a small fraction of analogous $K^\pm$ modes and some small fraction of higher odd number prong modes which are not included in the table.

1.1.5 Problems with the Standard Model

We conclude this review of the SM with a description of the problems which it has. These problems form the motivation for the development of SUSY, which is the subject of the next section.

DECAY MODE	BRANCH
$\mu^-\overline{\nu}_\mu\nu_\tau$	$(17.36 \pm 0.05)\%$
$e^-\overline{\nu}_e\nu_\tau$	$(17.85 \pm 0.05)\%$
$\pi^-\nu_\tau$	$(10.91 \pm 0.07)\%$
$\pi^-\pi^0\nu_\tau$	$(25.51 \pm 0.09)\%$
$\pi^-2\pi^0\nu_\tau$	$(9.29 \pm 0.11)\%$
$2\pi^-\pi^+\nu_\tau$	$(9.32 \pm 0.07)\%$
$2\pi^-\pi^+\pi^0\nu_\tau$	$(4.61 \pm 0.06)\%$

TABLE 1.2: The main tau decay modes and branches [1]. Modes are listed for τ^-, but the exactly analogous modes exist for τ^+.

As mentioned before, prior to any internal problems with the SM, there is the "elephant in the room" problem that it completely ignores the gravitational force. If one assumes that all of the fundamental constituents of the universe are describable under one "theory of everything", then this problem alone is enough to lead one to believe that the SM is incomplete.

Other features of the universe which the SM fails to address are the dark matter (23% of the energy of the universe), and the dark energy (72% of the energy of the universe), which are both experimentally observed phenomena.

Another "problem" with the SM, is not exactly a problem, but an issue of the displeasure that one feels at the seeming arbitrariness of such features as the number of free parameters of the theory (19) and the 3 generation structure of the fermions. In analogy to the periodic table structure, one is drawn to believe that there is some deeper underlying and more "simple" structure which is responsible for these features.

Finally the major internal feature of the theory which leads one to the "incomplete" hypothesis is the so-called "hierarchy problem". There are a number theoretical and experimental arguments which place constraints on the Higgs mass. These suggest that the mass should be somewhere in the range 130-190 GeV. Unfortunately for the SM a fermion of mass m_f and Yukawa coupling λ_f contributes to the square of the Higgs mass via

$$\Delta M_H^2 = -\frac{|\lambda_f|^2}{8\pi^2}(\Lambda_{UV}^2 + \cdots) \tag{1.5}$$

where Λ_{UV} is the so-called "ultra-violet cut-off" and is the energy scale at which new physics enters. Summing these contributions leads to quadratic divergences in M_H^2 and, if we set Λ_{UV} to the Planck scale, a large Higgs mass results. The only way to avoid this problem within the SM model requires a high level of fine-tuning which leads one to seek other solutions to the problem.

1.2 Supersymmetry

1.2.1 Overview

As mentioned in the previous section, there are a number of issues with the SM which form the motivation for theoretical extensions to it. The most popular and promising of these extensions is supersymmetry. [3]

We have seen in the formulation of the SM model the important role that symmetries and their breaking mechanisms have played. Supersymmetry extends these ideas to encompass a new symmetry; It is posited that the universe respects a symmetry between fermions and bosons. In terms of the theoretical formulation, this is equivalent to saying that the theory is invariant under a operator which transforms fermionic states to bosonic states *i.e.* an operator which changes half integer spin particles in to integer spin particles, and vice versa. Thus in an unbroken supersymmetric model, every SM fermion has a bosonic "superpartner" with the same mass and quantum numbers, and vice versa.

One of the main reasons that it is expected that some form of supersymmetry will be correct is that it solves the above-mentioned hierarchy problem in a natural way. It turns out that the new superpartner states of the SM fermions can add radiative corrections terms to the Higgs mass which cancel the terms coming from the SM fermions, thus rendering the Higgs mass safe from such corrections.

Another attractive property of supersymmetry is that it allows the gauge coupling strengths of the SM to become unified at the GUT scale. This comes about since the running of the gauge coupling strengths from the electroweak to the GUT scale is dependent on the particles which are manifest over that energy range. If SUSY exists at the electroweak scale then these runnings are affected in such a way the three couplings converge at the GUT scale. It is expected that in the Grand Unified Theory these coupling constants should unify at the GUT scale. This is a very compelling piece of theoretical evidence for weak scale supersymmetry.

Finally supersymmetric theories which respect R-parity (see Section 1.2.3). provide an excellent candidate for dark matter. This is because the lightest supersymmetric particle (LSP) is required to be stable, and, given that it has the correct properties, such as being neutral, it can explain the observed excess in mass in the universe above that which is visible. We will see in section Section 1.2.6 that requiring the LSP to be the dark matter particle helps to constrain the phase space of supersymmetric models.

Particle	Symbol	Spin	Superpartner	Symbol	Spin
Quark	q	$\frac{1}{2}$	Squark	$\tilde{q}$	0
Lepton	l	$\frac{1}{2}$	Slepton	$\tilde{l}$	0
W	W	1	Wino	$\tilde{W}$	$\frac{1}{2}$
B	B	1	Bino	$\tilde{B}$	$\frac{1}{2}$
Gluon	g	1	Gluino	$\tilde{g}$	$\frac{1}{2}$
Higgs	H_u, H_d	0	Higgsino	$\tilde{H}_u, \tilde{H}_d$	$\frac{1}{2}$

Table 1.3: The particle spectrum which results from the MSSM.

1.2.2 The Minimal Supersymmetric Standard Model

The minimal supersymmetric standard model (MSSM) is the supersymmetric extension to the standard model which results in the minimum number of extra particles. These particles are listed next to their SM counterparts in Table 1.3. The names of the superpartners of fermions are given by placing an "s" in front of the fermion name, while for the bosons the name is suffixed with an "ino". Superpartners are denoted symbolically by placing a tilde over the corresponding particle symbol.

While the doubling of most of the SM particles is relatively simple, the Higgs requires special attention. It turns out that a single Higgs is not sufficient in the MSSM to explain the coupling between the Higgs and up and down type quarks. Instead it is required that there are two complex $SU(2)_L$ doublets h_u and h_d where the subscripts u and d denote that each Higgs couples to up and down type quarks respectively. This then results in eight degrees of freedom for the Higgs sector, and, when electroweak symmetry breaking occurs within the MSSM framework, three of these mix with the W and B bosons to give $W^{\pm}, Z$ while the remainder become Higgs scalar mass eigenstates which are denoted h^0, H^0, A^0 and $H^{\pm}$.

Below is listed the ways in which all of the SUSY states listed in Table 1.3 mix to form the physical eigenstates. Note that the subscripts L and R refer to the superpartner of the respective chiral components of the SM fermions (the superpartners do not have chiral components since they are spin zero). Also note that the mixing in the squark and sfermion sectors is typically proportional to the mass of the associated SM fermion, and thus it is large for the third generation.

$$H_u^0, H_d^0, H_u^+, H_d^- \rightarrow h^0, H^0, A^0, H^{\pm} \text{ (Higgs)}$$

$$\tilde{t}_L, \tilde{t}_R, \tilde{b}_L, \tilde{b}_R \rightarrow \tilde{t}_1, \tilde{t}_2, \tilde{b}_1, \tilde{b}_2 \text{ (Stop/Sbottom)}$$

$$\tilde{\tau}_L, \tilde{\tau}_R \rightarrow \tilde{\tau}_1, \tilde{\tau}_2 \text{ (Staus)}$$

$$\tilde{B}^0, \tilde{W}^0, \tilde{H}_u^0, \tilde{H}_d^0 \rightarrow \tilde{\chi}_1^0, \tilde{\chi}_2^0, \tilde{\chi}_3^0, \tilde{\chi}_4^0 \text{ (Neutralinos)}$$

$$\tilde{W}^{\pm}, \tilde{H}_u^+, \tilde{H}_d^- \rightarrow \tilde{\chi}_1^{\pm}, \tilde{\chi}_2^{\pm} \text{ (Charginos)}$$

1.2.3 R-parity

R-parity is defined as

$$P_R = (-1)^{3(B-L)+2s} \tag{1.6}$$

where B is baryon number, L is lepton number and s is spin. It is introduced in to the MSSM as a conserved multiplicative quantum number assigned to each particle in order that such phenomena as the measured lower limit of the proton lifetime can be explained. The SM particles acquire an R-parity of +1 while the SUSY particles acquire an R-parity of -1. Conservation of R-parity has a number of consequences for the phenomenology of SUSY events, of which the most important are listed below:

1. In accelerator collisions sparticles must be created in pairs
2. The LSP must be stable
3. All sparticles must decay to states with an odd number of sparticles (usually one)

1.2.4 SUSY breaking

If the supersymmetry were a perfect symmetry of nature, then the masses of the superpartners would be exactly the same as those of their SM counterparts, and thus they would have already been observed in collider experiments (no spin 1 particle has ever been observed with the same mass as the electron). Thus, in order to remain viable, the supersymmetry must be broken somehow, resulting in the masses of the superpartners becoming large. This is analogous to the spontaneous symmetry breaking of electroweak theory. In order to break the supersymmetry without spoiling the desired cancellations to the radiative corrections of the Higgs mass, the mass differences between the SM and SUSY particles must not be too large. Thus the breaking terms must be "soft". It is thus postulated that the breaking is mediated to the MSSM from a "hidden sector" of particles where these particles have little or no direct coupling to the supersymmetric particles. The SUSY Lagrangian can thus be written

$$\mathcal{L} = \mathcal{L}_{SUSY} + \mathcal{L}_{soft} \tag{1.7}$$

where the $\mathcal{L}_{SUSY}$ component is invariant under supersymmetry, while the $\mathcal{L}_{soft}$ component breaks it by introducing mass terms for the sparticles. This soft component introduces an unwieldy 105 new parameters to the theory.

Though supersymmetry is required to be broken in order to result in the large sparticle masses, the exact mechanism of this breaking is open to speculation.

1.2.5 Minimal supergravity

One popular candidate for mediating supersymmetry breaking is so-called "supergravity". Here we focus on the minimal supergravity model (mSUGRA) which is the SUSY model studied in this thesis. In this scheme the breaking is mediated from the hidden sector by the graviton. A number of constraints are placed on the MSSM which results in the theory being parametrised in five variables. They are

- m_0: The universal scalar mass at the GUT scale.
- $m_{1/2}$: The universal gaugino mass at the GUT scale.
- A_0: The universal trilinear coupling strength of sfermions and Higgs at the GUT scale.
- $\tan\beta$: β is the ratio of the VEVs of H_u and H_d.
- sign(μ) The sign of the Higgsino mass parameter.

One of the attractive features of the mSUGRA model, and the reason why it is the focus of a large portion of SUSY phenomenological research, is its predictive power from just these five variables. Furthermore a number of constraints can be placed on these variables from existing experimental data. One of the important open areas of the phase space is the so-called "coannihilation region", which is the focus of this study, and which is the subject of the next section.

1.2.6 The coannihilation region

1.2.6.1 Experimental constraints on mSUGRA phase space

As mentioned above the mSUGRA phase space can be constrained by existing experimental data. The strongest of these constraints, given that the LSP is the source of dark matter, is provided by the WMAP satellite which has measured the dark matter density to be $\Omega_{CDM}h^2 = 0.1126^{+0.0161}_{-0.0181}$.[4] Given some input parameters to mSUGRA, the density of the LSP arising from the processes in the early universe can be calculated, and this is required to be consistent with the measured value. Other constraints on the phase space include the lower limit placed on the mass of the lightest charged sparticle provided by direct SUSY searches, the lower limit on the Higgs mass from direct Higgs searches, and the measurement of $b \rightarrow s\gamma$ decay.

Figure 1.1 show the allowed regions of the mSUGRA phase space under these constraints where for this plot, $\tan\beta$ has been set to 10, $\text{sign}(\mu) > 0$ and $A_0 = 0$. The thin strip allowed right on the border where the LSP becomes charged (becomes the stau) is known as the "coannihilation region". In this border region the lightest neutralino becomes near mass degenerate with the stau. It is for this reason that the region is allowed, since, when the masses of these two particles are near degenerate, their coannihilation in the early universe is efficient enough to account for the observed amount of dark matter.

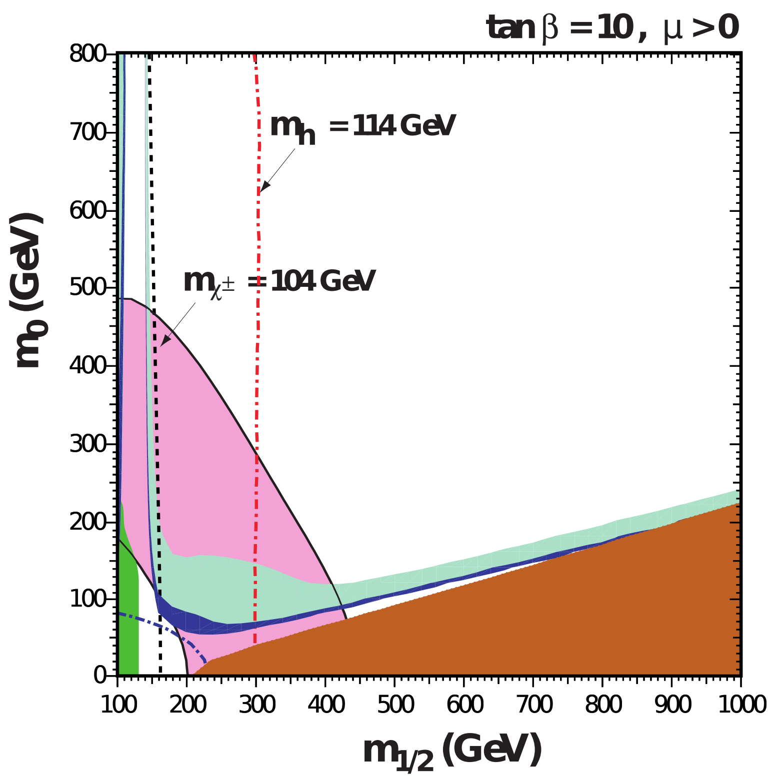

FIGURE 1.1: The constraints on the mSUGRA phase space provided by existing experimental data. For this plot $\tan\beta = 10, \mu > 0$ and $A_0 = 0$. The dark blue regions are the allowed regions from the WMAP measurement of the dark matter density (the lighter blue is the region that was constrained by the data previous to WMAP). The brown shaded areas are where the LSP is charged. Green regions are disallowed by $b \rightarrow s\gamma$ measurements. Pink regions are favoured by measurements of the anomalous magnetic moment of the muon. Also included are the constraints provided by the lower limits on the Higgs mass (114GeV) and the $\chi_1^{\pm}$ mass (104GeV). [5]

	Mass[GeV]		Mass[GeV]
$\tilde{g}$	829		
$\tilde{u}_L$	761	$\tilde{u}_R$	736
$\tilde{d}_L$	765	$\tilde{d}_R$	734
$\tilde{b}_1$	702	$\tilde{b}_2$	732
$\tilde{t}_1$	565	$\tilde{t}_2$	756
$\tilde{l}_L$	252	$\tilde{l}_R$	153
$\tilde{\tau}_1$	147	$\tilde{\tau}_2$	253
$\tilde{\nu}_L$	237	$\tilde{\nu}_\tau$	235
$\tilde{\chi}_1^0$	140	$\tilde{\chi}_2^0$	262
$\tilde{\chi}_3^0$	462	$\tilde{\chi}_4^0$	480
$\tilde{\chi}_1^\pm$	262	$\tilde{\chi}_2^\pm$	479

TABLE 1.4: The ATLAS coannihilation region reference point mass spectrum (Isajet 7.79), where $\tilde{u} \sim \tilde{c}$, $\tilde{d} \sim \tilde{s}$, $\tilde{e} \sim \tilde{\mu} = \tilde{l}$ and $\tilde{\nu}_e \sim \tilde{\nu}_\mu = \tilde{\nu}_L$.

1.2.6.2 The coannihilation region reference point used for this analysis

For this study the following parameter point in the coannihilation region was used

- $m_0 = 70\text{GeV}$
- $m_{1/2} = 350\text{GeV}$
- $\tan\beta = 10$ (1.8)
- $A = 0$
- $\mu > 0$

This is the standard ATLAS coannihilation region reference point (known in ATLAS parlance as "SU1"). It has a cross section of 2.58 pb at $E_{CM} = 10\text{TeV}$, which is the LHC collision energy used for this study (see Section 4.1).

Table 1.4 lists the resulting mass spectrum for this point while Table 1.5 lists the coannihilation region decay branches which are most relevant for this analysis. In particular we note the small mass difference between the $\tilde{\tau}_1$ and the $\tilde{\chi}_1^0$ which, as discussed above, allows for the efficient coannihilation of these two particles in the early universe. On the other hand, from a collider experiment point of view, it means that a $\tilde{\tau}_1$ produced in a collision will decay to an extremely soft tau. It is the reconstruction of this very soft tau, and the resulting reconstruction of the "golden decay" $M_{\tau,\tau}$ spectrum endpoint, which is the focus of this thesis (see Section 3.2.1).

	Decay	BR	Decay	BR
$\tilde{g}$	$\tilde{q}_L, q$	19%	$\tilde{q}_L \to \tilde{\chi}_2^0, q$	31-32%
	$\tilde{q}_R, q$	37%	$\tilde{q}_R \to \tilde{\chi}_2^0, q$	3%
	$\tilde{b}_1, b$	16%	$\tilde{b}_1 \to \tilde{\chi}_2^0, b$	23%
	$\tilde{b}_2, b$	10%	$\tilde{b}_2 \to \tilde{\chi}_2^0, b$	8%
	$\tilde{t}_1, t$	18%	$\tilde{t}_1 \to \tilde{\chi}_2^0, t$	15%
			$\tilde{t}_2 \to \tilde{\chi}_2^0, t$	10%

	Decay	BR	Decay	BR
$\tilde{\chi}_2^0$	$\tilde{l}_L, l$	7%	$\tilde{l}_R, l$	3%
	$\tilde{\tau}_1, \tau$	21%	$\tilde{\tau}_2, \tau$	3%
	$\tilde{\nu}_L, \nu$	38%	$\tilde{\nu}_\tau, \nu_\tau$	23%

Decay	BR
$\tilde{\tau}_1 \to \tilde{\chi}_1^0, \tau$	100%

TABLE 1.5: The relevant decay branches of the ATLAS coannihilation region reference point (Isajet 7.79).

Chapter 2

The LHC and the ATLAS detector

Since its inception in post-war 1950's Europe, the European Organisation for Nuclear Research (CERN) has been one of the main focus points for high energy frontier fundamental physics, and international scientific collaboration. Its experiments have pushed the boundaries of our fundamental knowledge of the universe for the last fifty years with a number of them resulting in Nobel Prizes. At the end of 2009 after a couple of technical hiccups the Large Hadron Collider (LHC), the latest of these great experiments came online and was able to successfully circulate and collide beams at a world record setting energy of 1.18 TeV per beam. The following chapter gives a brief outline of this machine, followed by some technical details of one of its multipurpose detectors, the ATLAS detector.

2.1 The LHC

The LHC is a high energy proton proton collider constructed in the old LEP experiment tunnel which is 27km in circumference and approximately 100 metres below the Franco-Swiss border. It has a design proton-proton collision energy of 14TeV with a peak luminosity of $10^{34}\text{cm}^{-2}\text{s}^{-1}$ making it the worlds most powerful particle accelerator, by a factor of seven in energy and 100 in luminosity. These beams will be collided at the locations of the four main detector around the collider ring. Prior to the protons being injected in to the LHC they are accelerated to an injection energy of 450GeV in 3 stages: an initial linac and booster, the Proton Synchrotron (PS) and the Super Proton Synchrotron (SPS). For some short periods the LHC will also be used as a heavy ion collider, colliding lead ions in order to study the postulated quark-gluon plasma. Figure 2.1 shows the overall layout of the machine and its main detectors.

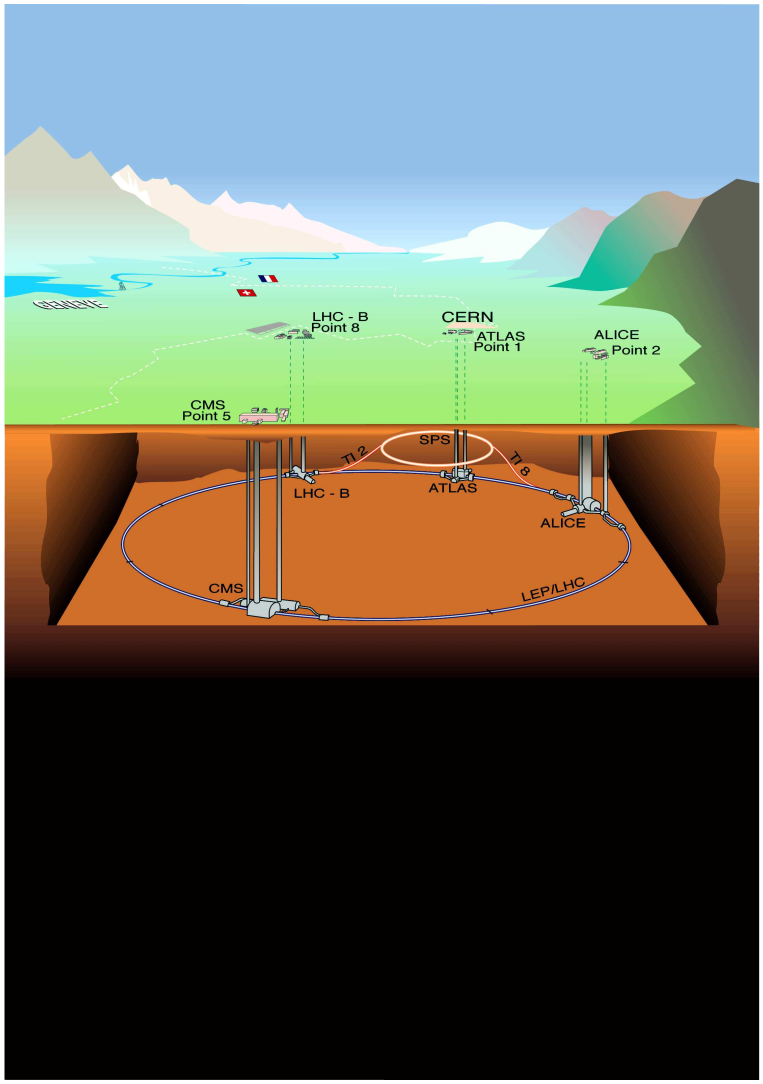

FIGURE 2.1: A map of the LHC with its four main detectors located around its ring. [6]

The accelerator itself consist of two interleaved synchrotron rings which share the same mechanical structure and cryostat. The circulating beams are bent with 1232 8.2T superconducting NbTi dipole magnets, while focussing is achieved with 858 quadrupole magnets. In addition there are over 6000 other magnets for correcting the beam dynamics. All of these magnets must operate at a super-fluid helium temperature of 1.9K making the engineering requirements of the machine particularly challenging. Acceleration is achieved with 8 RF cavities per beam with a maximum field strength of 5.5 MV/m. Figure 2.2 depicts an LHC dipole magnet with its various components visible.

Some of the other parameters of the machine are summarised in Table 2.1

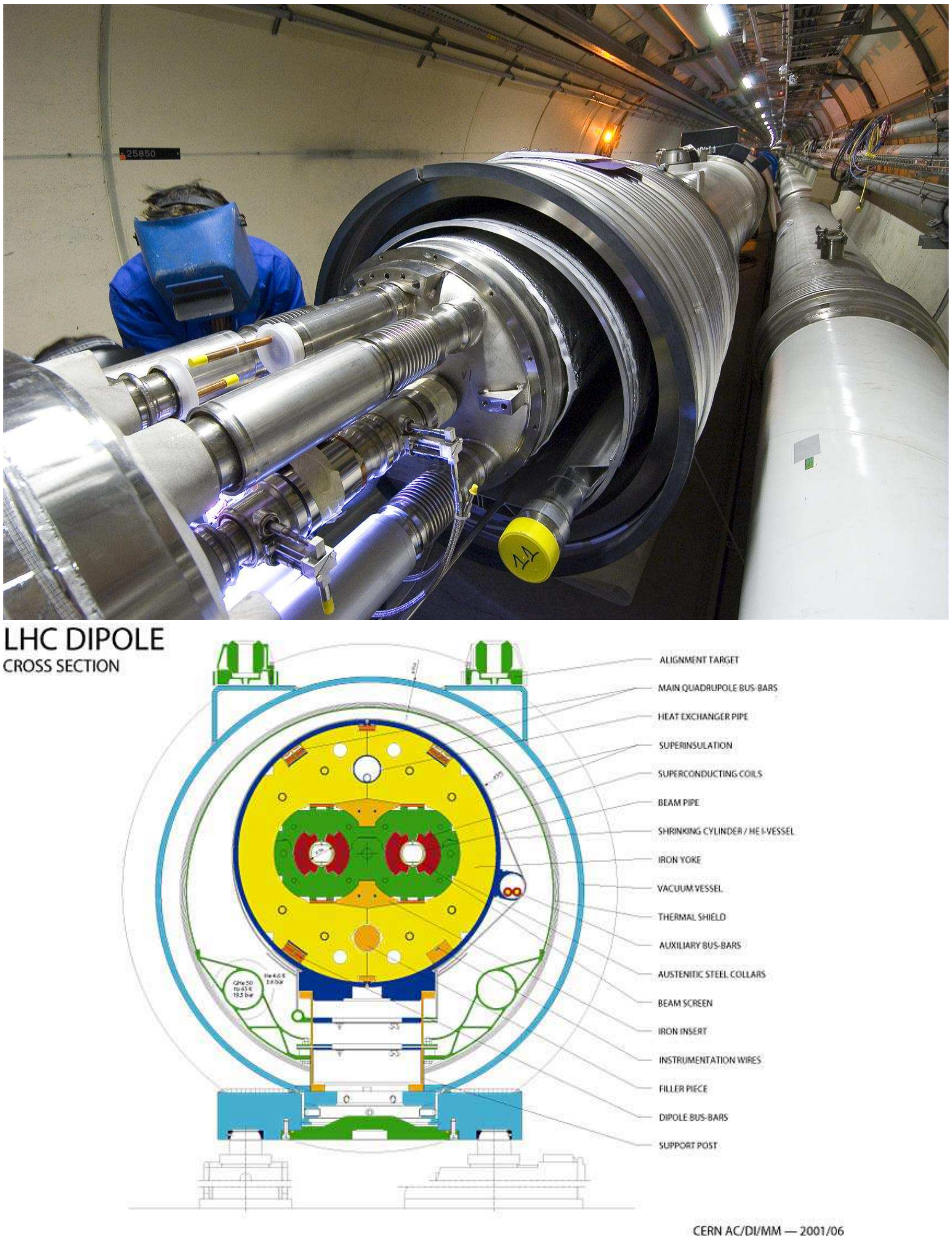

FIGURE 2.2: The photo on the top shows the first interconnection being made between LHC cryomagnets. [7] The figure on the bottom shows the cross-section of the LHC dipole magnet. [8]

Parameter	Value	
Beam collision energy	7 TeV	
Beam injection energy	0.45 TeV	
Machine circumference	26658.833 m	
Design Luminosity	$10^{34}\text{cm}^{-2}\text{s}^{-1}$	
Protons per bunch	1.15×10^{11}	
Bunch period	25ns	
Bunches per beam	2835	
Dipole field at 7TeV	8.33 T	
Maximum RF Cavity strength	5.5 MV/m	
Power consumption	120 MW	

Table 2.1: Some of the LHC parameters. Most parameters are for design luminosity.

2.2 The ATLAS detector

In the following a brief outline of the ATLAS detector will be given. Particular attention will be paid to the subsystems which are most relevant to this thesis, which are the inner detector tracker and the EM calorimetry system. For further details the reader is referred to [9].

2.2.1 Physics goals and detector overview

The ATLAS detector (A Toroidal Lhc ApparatuS) is the largest of the LHC detectors and is one of its two multipurpose detectors. Its main physics goals are

- The search for the Higgs boson, or some other mechanism for electroweak symmetry breaking
- The search for physics beyond the SM (SUSY, extra dimensions etc.)
- The search for the source of the large CP violation
- Further precision measurements of known SM phenomena

The small cross sections for many of the interesting events ($\sim 1 - 100$ pb) against the backdrop of a large proton proton inelastic cross section (~ 10 mb) places very high demands on the performance of the ATLAS detector. Not only will ATLAS have to trigger on interesting events out of 10^9 inelastic events/s, it will have to do so in pile up conditions where an average of 23 inelastic events will arise in each bunch crossing at design luminosity. Precision measurements of the resulting particles of interesting events is also a high priority. The various subsystems of the detector have been designed in order to achieve these exacting standards and each plays a different role in the accurate measurement and identification of particles. The inner detector tracker and the solenoid magnet provide precise momentum, direction and vertexing information for the charged particles in an event, as well as electron identification. The EM and hadronic calorimeters provide energy and direction measurements of photons, electrons, taus and jets, and also identification information for objects from their energy deposit shapes. Finally the muon and the outer toroidal magnet systems provide information on the event's muons. Figure 2.3 show the general layout of the ATLAS detector, with a cutaway showing where each of the above components is located within it. Each of these components will be further discussed in coming sections.

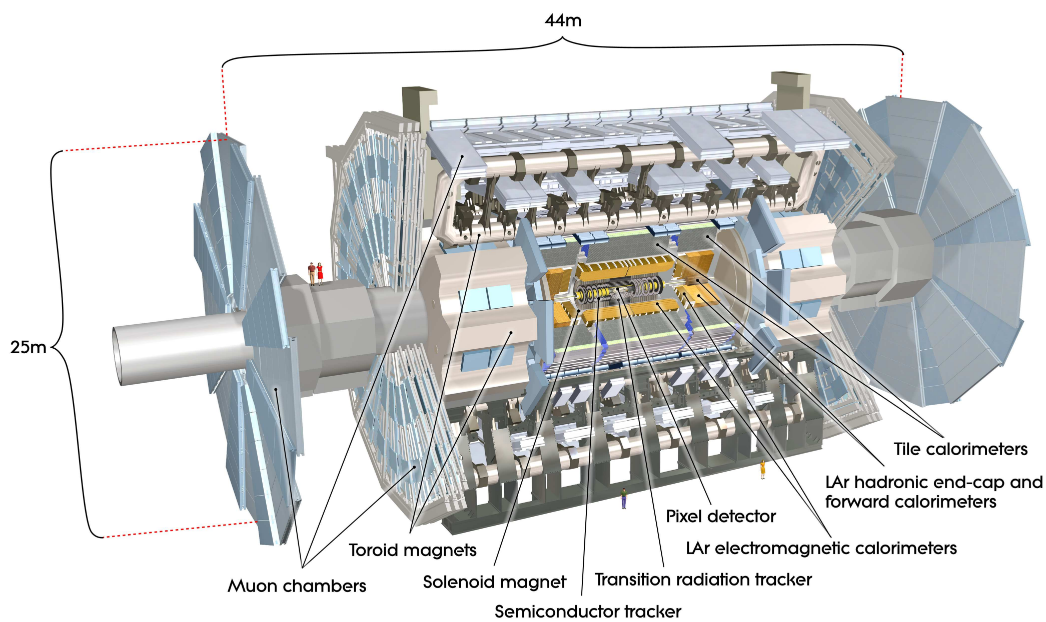

FIGURE 2.3: A cutaway overview of the ATLAS detector showing the locations of its various components. [9]

The coordinate system for the ATLAS detector is defined with respect to the interaction point with the z-axis pointing in the direction of the beam, the x-axis toward the centre of the LHC and the y-axis upwards. In polar coordinates, θ is the angle made with the z-axis while the azimuthal angle ϕ is measured around the beam axis. Instead of the polar angle the more useful pseudorapidity, $\eta = -\ln\tan\theta/2$, is usually used. The distance ΔR in η, ϕ space is defined as $\Delta R = \sqrt{\Delta\eta^2 + \Delta\phi^2}$. Generally speaking, the ATLAS detector is constructed in three "sections". The "barrel" section components cover the regions of small $|\eta|$, and are constructed in barrel shapes which are concentric with the beam. The "endcap" section components cover larger $|\eta|$ regions and are constructed in wheels which are coaxial with the beam and placed some distance in z from the interaction point. The "forward" components (consisting of the forward calorimeters) are for measurements at very large $|\eta|$, and are constructed similarly to the "endcap" components. η coverage for each component depends on its radial distance from the beam.

2.2.2 The magnet systems

The ATLAS detector is fitted with two distinct magnet system. The first is the inner detector NbTi superconducting solenoid which provides standard bending of charge particles in the inner detector for momentum measurements and charge discrimination. It is 5 tonnes, 5.3m in length, 2.4 m in diameter and provides a 2 T field along the beam line, enough to provide an accurate measurement of particles up to a momentum of 100 GeV. All of this is achieved with a thickness of only 45 mm (0.66 radiation lengths). A thin solenoid magnet is essential in order to minimise the amount of dead material before the calorimeters.

The second magnet system is rather peculiar to the ATLAS detector and comprises the outer toroidal magnets which are designed to provide bending to muons for the muon system. There are 3 such toroids, the barrel toroid and two endcap toroids, providing fields of 1 T and 0.5 T respectively. The fields for each toroid are provided by 8 NbTi superconducting "racetrack" shape coils assembled radially and symmetrically around the beam axis. The barrel toroid is 25.3 m in length and 20.1 m in diameter, while the endcap toroids are a more modest 5 m in length and are inserted in to the ends of the barrel toroid to provide overlap in the "transition" region. The bending provided by the toroids is essentially in the $R-\eta$ plane. The toroid system provides for measurements of muons of up to a momentum of $\sim$ 6TeV.

The relative layout of the components of the magnet systems is illustrated in Figure 2.4

2.2.3 The ATLAS inner detector

The accurate measurement of charged particle momentum and charge is achieved in ATLAS with its three component inner detector system in combination with the solenoid magnetic field. This system provides measurements of charged particles up to $|\eta| < 2.5$ and down to a p_T of ≈ 0.5 GeV.

The extreme density of particles close to the interaction point means that high granularity is required in the inner layers of the tracker in order to discriminate individual particles. High granularity is also a prerequisite for achieving the precise momentum and vertex measurements which will enable the aforementioned physics goals to be met. The pixel and microstrip layers (SCT) of the inner detector enable ATLAS to achieve

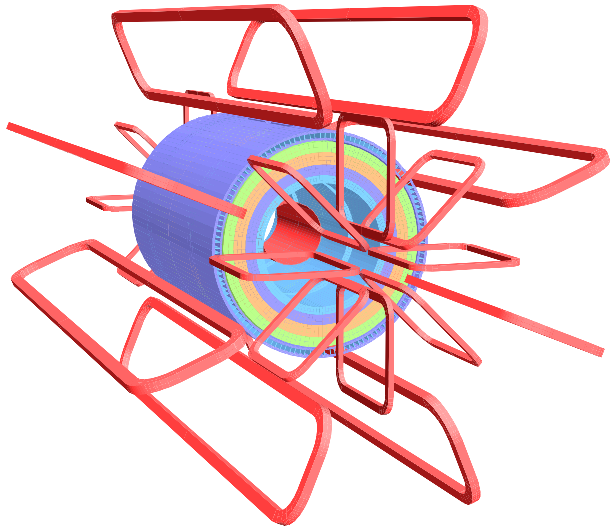

FIGURE 2.4: The ATLAS magnet system layout. The magnet systems are highlighted in red. The central solenoid is located inside the calorimeter volumes. The large barrel toroid is visible with the smaller endcap toroids inserted in to the spaces at its end.[9]

these goals. The transition radiation detector exterior to these silicon based systems supplements these measurements, and also offers the benefit of electron discrimination capabilities. Figure 2.5 shows a plan view of one of the quadrants of the inner detector, showing the dimensions and coverage of each of its components.

Figure 2.6 shows 3-D images depicting charged tracks traversing the barrel inner detector and the endcap inner detector.

2.2.3.1 The pixel and SCT detectors

Precision tracking is performed by the two inner most silicon semiconductor based systems.

The highest granularity pixel layers are the closest to the interaction point and consist of three layers in the barrel region concentric around the beampipe, and three layers in each of the endcap regions, placed in disks perpendicular to the beam pipe. Typically three layers are crossed by each particle. The layers are constructed from 1744 modules each containing 46080 effective pixels of a minimum size in $R-\phi \times z(R)$ in the barrel (endcap) of $50 \times 400\mu\mathrm{m}^2$ (90% of pixels). In each module pixel arrays are bump bonded to 16 front end integrated read out circuits, each of which serve 18×160 pixel diodes. The result is a total of 80.4 million read out channels. The intrinsic accuracies per module are $10\mu\mathrm{m}(R-\phi)$ and $115\mu m(z)$ in the barrel and $10\mu\mathrm{m}(R-\phi)$ and $115\mu m(R)$ in the endcaps. The measurement of the inner most pixel layer mostly determines the

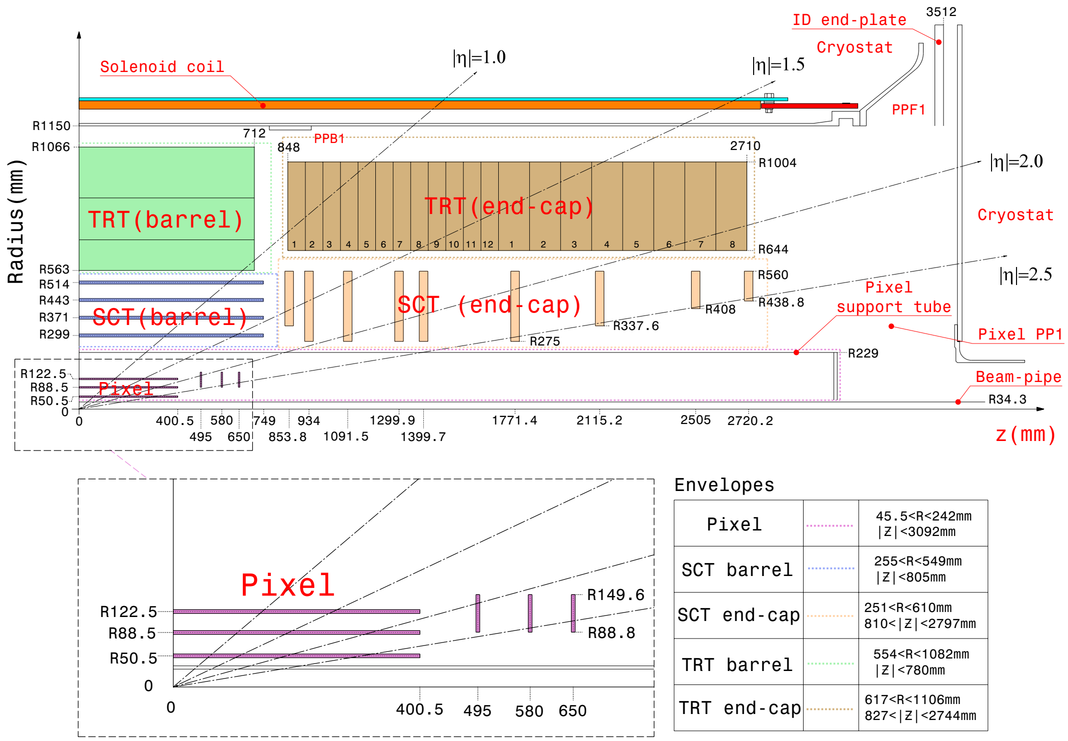

FIGURE 2.5: Plan view of a quadrant of the ATLAS inner detector showing the dimensions and coverage of each of its components.[9]

accuracy of secondary vertex measurements, which are important for tau discrimination due to the taus finite decay length. This first layer is known as the "B" layer.

As the distance from the beam pipe increases the density of traversing particles decreases meaning that the discrimination of individual particles is less sensitive to the granularity of the tracker. As such the SCT layers of the inner detector are composed of modules containing silicon strips of 63.6 mm length and 80μm pitch. Wafers containing these strips are placed back to back giving an effective strip length of 123.2 mm. In the barrel the SCT contains four layers, with each layer composed of two sets of wafers. One set in each layer has the strips running parallel to the beam such that the $R - \phi$ direction is accurately measured. The other set is placed at a stereo angle of 40 mrad with respect to the other which allows a z-direction measurement of $\sim$ 2mm resolution. The endcap set ups are similar but this time the wafers are placed in 9 disks with the $R - \phi$ measurement performed by wafers placed with tapered strips running radially. The intrinsic accuracies per module are 17μm$(R - \phi)$ and 580$\mu m(z)$ in the barrel and 17μm$(R - \phi)$ and 580$\mu m(R)$ in the endcaps. The total number of readout channels in the SCT is 6.3 million.

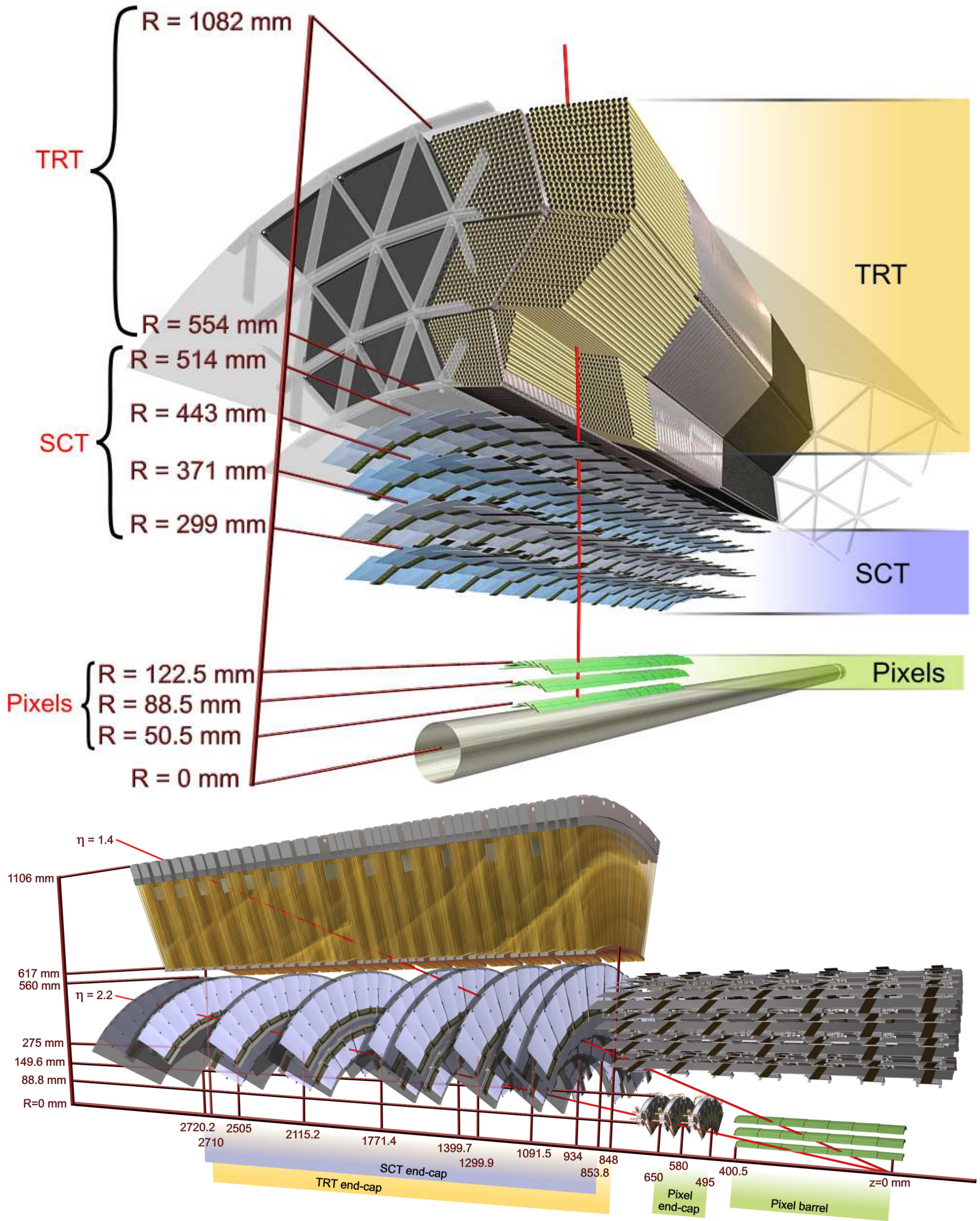

FIGURE 2.6: 3D view of charged particles traversing the inner detector elements. The top figure depicts a 10 GeV p_T charged track propagating at $\eta = 0.3$. The bottom figure depicts two 10 GeV p_T charged tracks propagating at $\eta = 1.4$ and $\eta = 2.2$. Note that the TRT only extends to $\eta = 2$.[9]

2.2.3.2 The transition radiation tracker

The transition radiation tracker is a drift tube tracking system which allows tracks to be followed out to about a radial distance of a metre in the barrel. It was devised as a cheap alternative to silicon systems for the outer track measurements but still provides a high number of relatively accurate measurements in the $R - \phi$ direction. The basic components of the system are 4 mm diameter "straw" drift tubes which have $31\mu m$ diameter gold-plated tungsten wire running down their centre acting as the anode, and aluminium plated inner walls which act as the cathode. Straws are layered in the direction of the beam axis in the barrel region while in the endcaps they are directed in the radial direction. In the barrel the wires are electrically split in the middle near $\eta = 0$. The straws are filled with a mixture of Xe CO_2 and O_2. Amplification of ionised particles is $\sim 2.5 \times 10^4$ and this charge is read out at each end of the straw, thus only information in $R - \phi$ is obtained. The accuracy is expected to be $170\mu m$ per straw.

A particularly interesting feature of the TRT is its electron discrimination capability which is achieved by stimulating "transition radiation" between the straws. Transition radiation is a phenomenon whereby relativistic charged particles crossing the boundary between materials of different dielectric constants emit photons. This phenomenon can be thought of as the charged particle "shaking off" the difference in its electric field as it crosses such a boundary. The energy loss on a transition is dependant on the Lorentz factor of the particle, E/mc^2, and as such, for a given energy, lighter charged particles such as electrons will emit much more transition radiation than, for example, hadrons. In order to stimulate significant transition radiation, the space between the straws is filled with a polypropylene/polyethylene fibre. The photons thus emitted by electrons are in the x-ray region, and the Xe within the straws present a high interaction cross section to these. Thus a number of "high" threshold hits in the TRT is characteristic of an electron traversing it. Electron identification with this method alone is expected to be 90% for a pion rejection of ≈ 100. Such measurements will be used in tau identification methods of this study in order to avoid considering the electrons arising from π^0 γ-ray conversion when determining the isolation of tau single prong modes (Section 5.1.1).

2.2.4 Calorimeters

The ATLAS calorimeters are situated outside of the solenoid and the inner detector. They can be generally divided in to two components: The EM calorimeters and the hadronic calorimeters. The EM calorimeters' primary purpose is to measure electron and photon energy while the hadronic calorimeters are designed to measure the energy of the hadronic components of jets. All combined they provide coverage up to $|\eta| < 4.9$.

All of the ATLAS calorimeters are so-called "sampling" calorimeters, meaning that inactive layers of the calorimeters stimulate showering while active layers measure a fraction of this shower energy. It should also be noted that all ATLAS calorimeters are non-compensating, so that correction of hadronic energy deposits must be done at the software level. Figure 2.7 shows the layout of the entire calorimetry system.

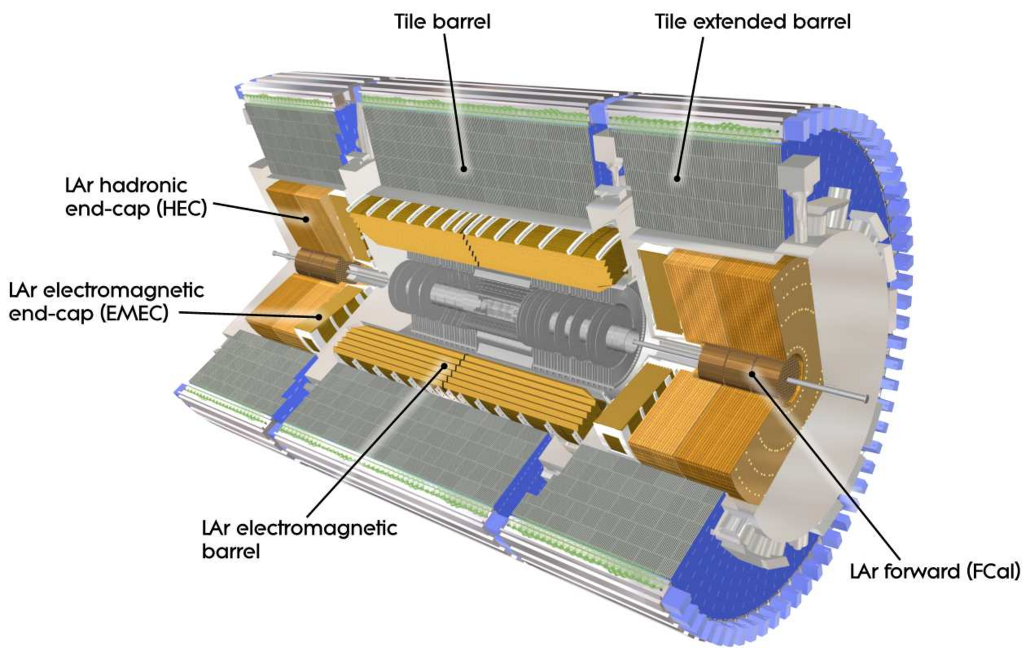

FIGURE 2.7: A cutaway view of the ATLAS calorimetry system.[9]

2.2.4.1 The EM calorimeters

The ATLAS EM calorimeter covers a range up to $|\eta| < 3.2$ and is divided in to a barrel component ($|\eta| < 1.475$) and two endcap components ($1.375 < |\eta| < 3.2$). The barrel component of the calorimeter is indeed a "barrel" shape concentric with the beam pipe, while the two endcaps are each composed of two coaxial wheels. The region where these two components meet is known as the "crack" region, and has a degraded performance due to the presence of considerable dead material (≈ 7 radiation lengths) from services. This has a significant effect on physics analyses in this region, as will be shown throughout this study.

The EM calorimeters are lead-liquid argon (LAr) sampling calorimeters with a characteristic accordion shape which enables complete ϕ coverage with no gaps. In the precision physics region of $|\eta| < 2.5$ the calorimeter is segmented longitudinally into successively coarser grained (laterally) layers: the "strip" layer, "middle" layer and "third" layer.

This geometry is shown in Figure 2.8. Combined, the EM calorimeter presents $\approx 22-24$ radiation lengths to particles entering it.

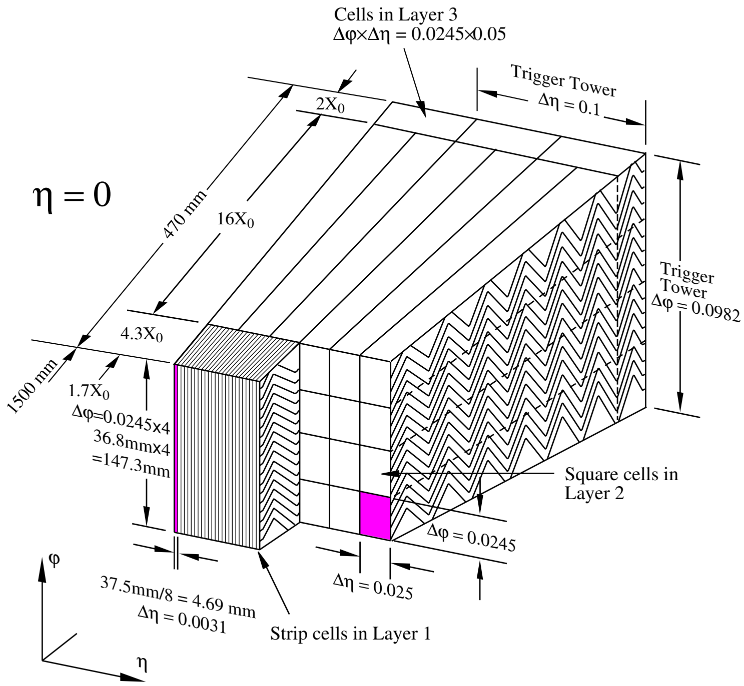

Figure 2.8: A sketch of a section of the barrel EM calorimeter. We can see the fine granularity in the first or "strip" layer. The granularity becomes increasingly coarser in the middle and third layers.[9]

The fine granularity of the EM calorimeter allows for good separation of clusters arising from close by particles (see for example the description of the topological clustering algorithm of Section 4.2.2), and also good discrimination of, for example, photons and hadrons, based on shower shape. Such shower shape information will be utilised in the tau identification algorithm of Section 5.1.2 in order to identify π^0 clusters arising from tau decay.

2.2.4.2 The hadronic calorimeters

The hadronic calorimeters can be divided in to three subsystems, the tile calorimeters, the hadronic endcap calorimeters and the forward calorimeters.

The tile calorimeter is located directly exterior to the barrel EM calorimeter. Its barrel covers the range $|\eta| < 1.0$ while the "extended" barrels cover the range $0.8 < |\eta| < 1.7$. It too is divided longitudinally and laterally to provide for jet shape measurements. Steel absorbers are used while scintillating tiles providing the active medium.

The hadronic endcap calorimeters cover the region $1.5 < |\eta| < 3.2$ and are located behind the EM endcaps. Like the EM calorimeters they are LAr calorimeters but of a simpler plate design using copper as as the absorption medium.

The forward calorimeters cover $3.1 < |\eta| < 4.9$ and ensure a high coverage of the η range. For accurate measurement of the missing transverse energy, an important signal for SUSY events, this high coverage is very important. The calorimeter is a high density copper and tungsten + LAr construction ensuring a high level of forward jet containment.

2.2.5 The muon spectrometer

There are two essential function of the ATLAS muon system. The first is the precision measurement of charged particles which exit the calorimetry system. This is performed by the Monitored drift tubes (MDTs) and the Cathode strip chambers (CSCs). The second role is to provide a fast trigger for the ATLAS experiment in the event of such particles, and this is achieved with Resistive plate chambers (RPCs) and Thin gap chambers (TGCs). The layout of the entire muon system is depicted in Figure 2.9. We can see that as with the rest of the detector, the low $|\eta|$ barrel systems are arranged concentrically around the beam pipe, in three layers. The high $|\eta|$ endcap systems are arranged in to four coaxial wheels.

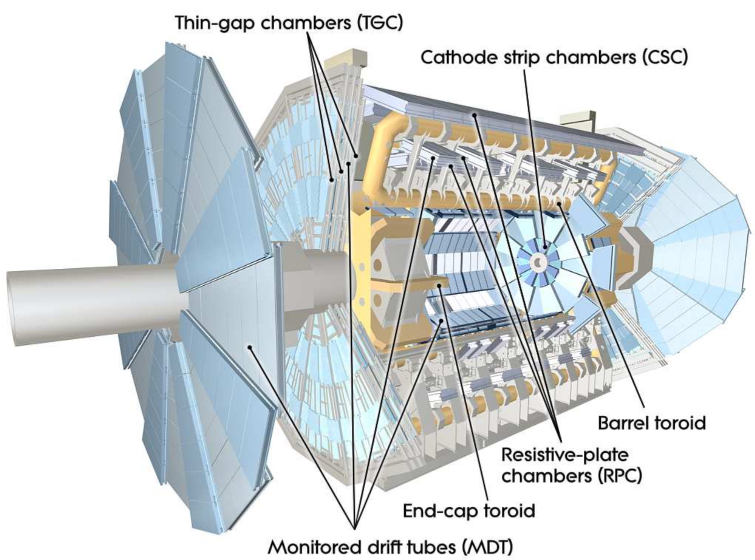

FIGURE 2.9: A cutaway view of the ATLAS muon system.[9]

2.2.6 The trigger and DAQ system

The design luminosity bunch crossing rate for the LHC is 40 MHz. Present storage and data handling capabilities require this rate to be reduced to around 200 Hz. This is achieved in ATLAS with a 3 stage trigger. The first is hardware based and combines reduced granularity signals from a number of the detector components. It looks for such things as the presence of high p_T jets, electrons, photons, taus, muons and large E_T^{miss}, which are all signs of interesting physics events. The trigger decision must be made within 2.5μs during which time the data is stored in "pipe line" memory close to the detector. Good events and their "regions of interest" are then passed to the level two trigger which analyses these regions exploiting the full granularity of the detector. Finally the level three trigger performs a full reconstruction of the event and from this decides which events are to be committed to memory for later physics analysis. Figure 2.10 depicts the basic logical flow of this process.

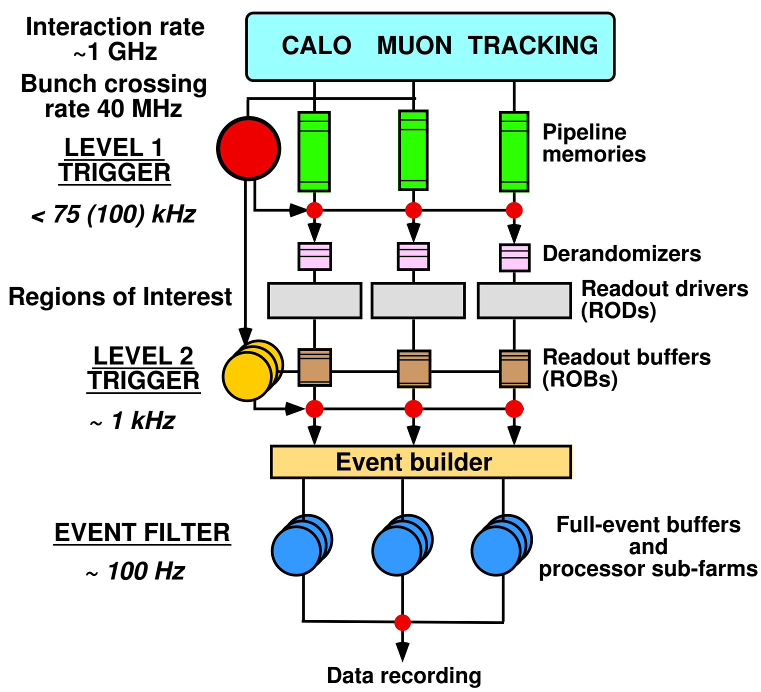

FIGURE 2.10: The logical flow of the ATLAS trigger system. [10]

Chapter 3

Phenomenology of mSUGRA Scenarios and the Coannihilation Region

In Chapter 1 the theoretical basis for mSUGRA and in particular the coannihilation region were presented. In this chapter the general phenomenology of mSUGRA events and the experimental methods for discriminating such events from the SM background will be described. Also a focussed discussion of the phenomenology of coannihilation region mSUGRA will be given, and the particular details of the kinematics of the so-called "golden decay" chain presented. It is the reconstruction of two of the taus arising from this decay chain which is the basis of this thesis.

Here we should make a note of the distinction between a general "inclusive" analysis of mSUGRA, and an "exclusive" one. Near the beginning of the LHC running the focus for mSUGRA analysis will be on establishing whether or not it actually exists. The strategy for this will be to search for excesses of certain quantities over the entire event sample which are consistent with mSUGRA expectations. These quantities are described in the next section and, if weak scale supersymmetry exists, excesses above SM expectations should be visible at the LHC with only a few fb^{-1} of data. This will constitute "discovery" of supersymmetry. Such an analysis is "inclusive".

On the other hand in order to understand the details of the correct mSUGRA model, for example the sparticle masses and decay widths, more focussed analyses of particular decay chains will be necessary. These are the so-called "exclusive" analyses. Because the scope of the event sample is necessarily narrowed with such analyses, they require much higher statistics than inclusive ones. As such they will be the focus of analyses at the LHC after mSUGRA discovery, and only once $\sim 10'$s of fb^{-1} of data have been collected. The golden decay chain analysis of this study is an exclusive one, and the details will be give in Section 3.2.1.

3.1 General phenomenology of mSUGRA events

3.1.1 Production processes and decay cascades

Being a hadron collider means, given that mSUGRA is the correct model for describing beyond-the-standard-model physics, that the SUSY production particles at the LHC will be coloured, *i.e.* the LHC will be a "squark and gluino factory". Figure 3.1 shows the main production processes for these sparticles in the proton-proton collisions at the LHC.

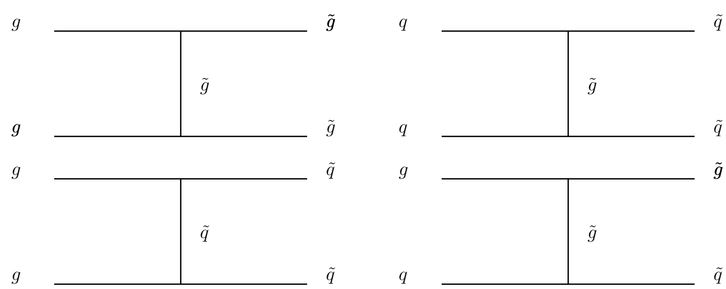

FIGURE 3.1: The main SUSY production processes at the LHC.

At the LHC energy scale these coloured particles are in general relatively heavy compared to the other sparticles which leads to their cascade decay to the LSP via the various other squarks, gauginos and the sleptons. The requirement of the conservation of R-parity means that sparticles must be created in pairs in LHC collisions. It also means that the decay of a sparticle must result in a state with an odd number of sparticles (where in practice this is usually one). The decay of these sparticles is analogous to the decay of their SM counterparts: Gluinos can decay via the analogous process to gluon splitting (for the case $m_{\tilde{g}} > m_{\tilde{q}}$), to a squark-quark pair, or squarks may decay via the analogous process to gluon emission to a gluino and a quark (for the case $m_{\tilde{q}} > m_{\tilde{g}}$). For this latter case, if the gluino is lighter than all of the squarks, it will go to a 3-body decay via an off-shell squark to a two quark + gaugino final state. Any resulting squarks can then decay via the analogous charged or neutral current processes to quarks and gauginos. Finally any resulting gauginos (except the LSP) will decay in analogous processes to the SM gauge bosons resulting in SM leptons, SM gauge bosons or a Higgs particle, plus the

LSP. The kinematic constraints of the particular point in the mSUGRA parameter space will determine the allowed cascades which the SUSY production particles will take.

Combining all of this, a typical mSUGRA production and decay process is illustrated in Figure 3.2. The generally large mass difference between the squarks/gluino and the electroweak gauginos means that squark/gluino decay will result in a number of very energetic quarks which will be observed in the detector as a number of characteristic very hard jets. Then, if the decay goes via leptons there is the possibility of a number of hard leptons [1]. Finally the conservation of R-parity means that the two final LSPs will be stable thus will traverse the detector. In order for the LSP to be a candidate for dark matter it is required to be neutral and weakly interacting. Since the LSP will also be massive the result is a so-called Weakly Interacting Massive Particle (WIMP). In the case of the mSUGRA model this will be a neutralino. These two massive neutralinos will thus escape the detector undetected resulting in the final characteristic SUSY signal of an imbalance in the sum of the transverse momentum measured in the detector.

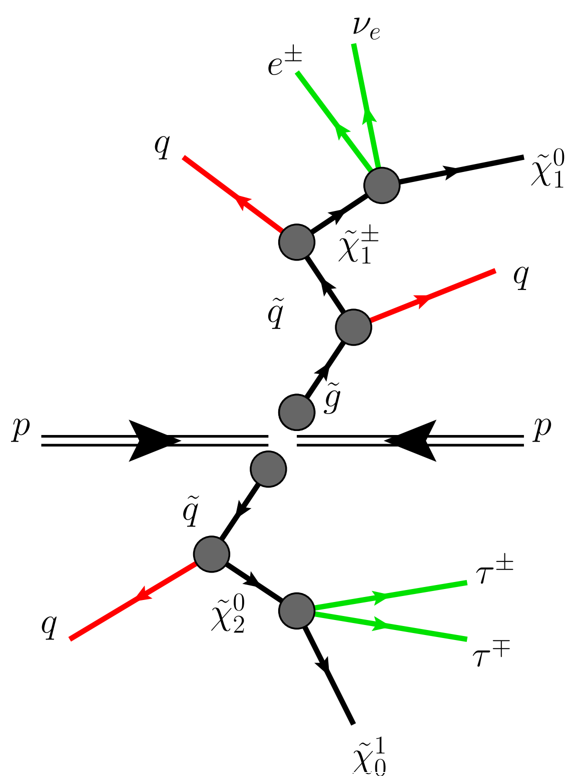

FIGURE 3.2: A typical topology for an mSUGRA event.

[1]In the case of the coannihilation region, one of the leptons can be very soft, but this is a rather unique signature.

3.1.2 Parameter definitions for SUSY analysis

Below are listed some of the parameters used to distinguish SUSY events. As mentioned above, it is the excesses in a number of these quantities which will constitute SUSY discovery. For this exclusive study cuts on these quantities will be used to isolate a pure sample of coannihilation region events. These cuts will be described in Chapter 7.

1. **Hard jets**

   A typical SUSY selection will require some number of hard jets in the event. The justification of this was described above. For this analysis the requirement will be for two hard jets, as will be described in Section 6.2.

2. **Missing transverse energy**

   Missing transverse energy, E_T^{miss}, is the imbalance in the vectorial sum of the measured E_T. This arises from particles such as neutralinos and neutrinos escaping the detector. For the case of mSUGRA events, large E_T^{miss} will arise from the escape of the two LSPs.

3. **Effective mass**

   For this analysis, the effective mass, M_{eff}, is defined as

   $$M_{eff} = P_T^{jet1} + P_T^{jet2} + E_T^{miss} \tag{3.1}$$

   which is a measure of the total activity in the detector. For mSUGRA this quantity is highly correlated with the SUSY mass scale.

4. **Distance between missing transverse energy and jets**

   For the copious QCD di-jet background in LHC collisions, E_T^{miss} will typically be in the direction of the jets, since E_T^{miss} from these events will largely arise from either neutrinos arising from weak processes within the jet, or from jet energy mis-measurement. For SUSY events there is no such correlation between the direction of the jets and the escaping LSP. Thus a cut on the minimum distance between jets and E_T^{miss}, $\Delta\phi_{jet\,i,MET}$, is effective at reducing QCD background.

5. **Transverse mass**

   The transverse mass, M_T, is defined as

   $$M_T^2 = m_\tau^2 + m_\chi^2 + 2(E_T^\tau E_T^{miss} - \mathbf{p}_T^\tau \cdot \mathbf{p}_T^{miss}) \tag{3.2}$$

   where

   $$E_T^\tau = \sqrt{(\mathbf{p}_T^\tau)^2 + m_\tau^2},\ E_T^{miss} = \sqrt{(\mathbf{p}_T^{miss})^2 + m_\chi^2}, \tag{3.3}$$

m_τ, and $\mathbf{p}_T^\tau$ are the mass and transverse momentum of the hardest reconstructed tau in the detector, and $\mathbf{p}_T^{miss}$ is the missing transverse momentum vector. m_χ is the mass of the escaping particle which is the source of the E_T^{miss}, and is usually assumed to be zero. The distribution of M_T for $W \to \tau, \nu$ decays exhibits a Jacobian peak at the W mass, thus a cut on this quantity is effective at reducing this background.

3.2 Phenomenology of coannihilation region golden decay events

Once a pure SUSY sample is isolated using cuts on the above parameters one can perform a more focussed exclusive analysis. Below we define the exclusive analysis which is the subject of this study.

3.2.1 The golden decay chain and the analysis of this study

The escape of the two LSPs from the detector means that the direct measurement of sparticle masses via the formation of invariant mass quantities is impossible. Instead SUSY exclusive analyses focus on the measurement of invariant mass *endpoints*. [11] [12] [13] In particular the cascade decay $\tilde{q} \to q\tilde{\chi}_2^0 \to ql\tilde{l} \to qll\tilde{\chi}_1^0$ is kinematically constrained, and the relationships between the endpoints of the invariant mass distributions of the visible products can be solved to give the masses of the sparticles in the cascade.

For this thesis we consider the following decay chain

$$\tilde{q} \to q\tilde{\chi}_2^0 \to q\tau\tilde{\tau}_1 \to q\tau\tau\tilde{\chi}_1^0 \tag{3.4}$$

This is the so-called "golden decay". Though the analysis of this particular chain is complicated by the further loss of energy from the tau neutrino, it is important since it contains the information of the mass of the $\tilde{\tau}_1$. Also, in some parts of the coannihilation region, the branching of $\tilde{\chi}_2^0$ via taus can be as high as 90% meaning that this may be the only viable option for obtaining information about the $\tilde{\chi}_2^0$.

In order to calculate the sparticle masses, the endpoints of $M_{\tau_1,\tau_2}, M_{\tau_1,q}, M_{\tau_2,q}$ and $M_{\tau_1,\tau_2,q}$ can be measured. These endpoints can be shown to have the following relationships [14]

$$
\begin{aligned}
M^{max}_{\tau_1,\tau_2} &= \sqrt{(M^2_{\tilde{\chi}^0_2} - M^2_{\tilde{\tau}})(M^2_{\tilde{\tau}} - M^2_{\tilde{\chi}^0_1})/M^2_{\tilde{\tau}}} \\
M^{max}_{\tau_1,q} &= \sqrt{(M^2_{\tilde{q}} - M^2_{\tilde{\chi}^0_2})(M^2_{\tilde{\chi}^2_0} - M^2_{\tilde{\tau}})/M^2_{\tilde{\chi}^2_0}} \\
M^{max}_{\tau_2,q} &= \sqrt{(M^2_{\tilde{q}} - M^2_{\tilde{\chi}^0_2})(M^2_{\tilde{\tau}} - M^2_{\tilde{\chi}^1_0})/(2M^2_{\tilde{\tau}} - M^2_{\tilde{\chi}^1_0})} \\
M^{max}_{\tau_1,\tau_2,q} &= \sqrt{(M^2_{\tilde{q}} - M^2_{\tilde{\chi}^0_2})(M^2_{\tilde{\chi}^2_0} - M^2_{\tilde{\chi}^1_0})/M^2_{\tilde{\chi}^2_0}}
\end{aligned}
\tag{3.5}
$$

As will be shown in the next section the most challenging measurement in the coannihilation region is that of the second tau of the decay chain. It will be shown that this tau is extremely soft.

The focus of *this* study is exclusively on the reconstruction of this very soft tau, with the goal being the efficient reconstruction of the $M_{\tau,\tau}$ distribution. This will allow for an accurate-as-possible determination of the $M_{\tau,\tau}$ endpoint which can then be used, along with analyses of the tau-jet endpoints, to determine the masses of the decay chain sparticles via the relations 3.5.

3.2.2 Golden decay kinematics

Before embarking in to the details of the method used for the soft tau reconstruction, we first give the details of the kinematics of the golden decay. The distributions for this section are made from the generator level information of the Monte Carlo samples which will be outlined in the next chapter. We note here that the fraction of the coannihilation region event sample containing the two-tau $\tilde{\chi}^0_2 \to \tau\tilde{\tau}_1 \to \tau\tau\tilde{\chi}^0_1$ chain is 7%.

Figure 3.3 shows the $p_{T,vis}$, η_{vis} and ϕ_{vis} distributions of the two taus coming from the above decay chain, where henceforth vis denotes the visible component of the taus. Also, from here the first tau of the decay chain is referred to as the "signal hard tau", while the second tau is referred to as the "signal soft tau". Indeed, we can see that the "hard" tau is relatively very hard due to the large mass difference between the $\tilde{\chi}^0_2$ and the $\tilde{\tau}$ of the decay chain, while the "soft" tau is relatively very soft due to the near degeneracy of the $\tilde{\tau}$ and the $\tilde{\chi}^0_1$. The means of their $p_{T,vis}$ are 79GeV and 9.3GeV respectively. We note that the softness of this signal soft tau makes its identification in the ATLAS detector difficult, and thus the reconstruction of the final $M_{\tau,\tau}$ distribution particularly challenging.

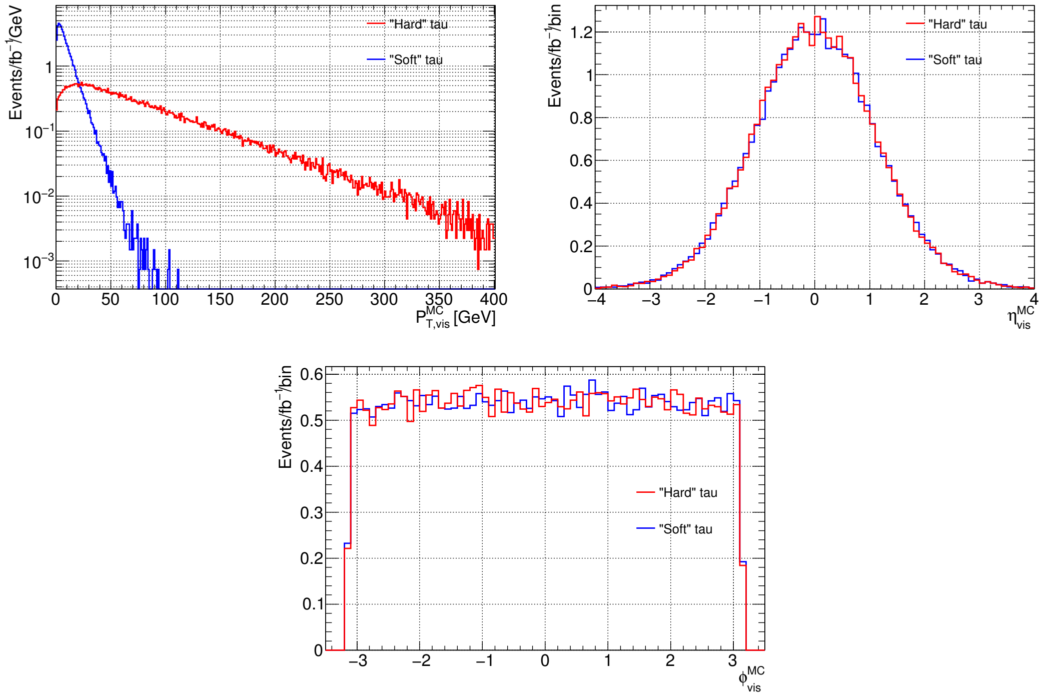

FIGURE 3.3: The truth level distributions of $p^{MC}_{T,vis}$ (top left), η^{MC}_{vis} (top right) and ϕ^{MC}_{vis} (bottom) for the coannihilation region signal hard and soft taus.

Figure 3.4 shows the distribution of the distance between the two taus, where again only the visible information is taken into account. We can see that there is a tendency for the soft tau to be rather close to the hard tau. This is due to their mutual boost which is provided by their parent $\tilde{\chi}^0_2$. In Section 5.1 we will use this containment to help to reduce the background to our final reconstruction.

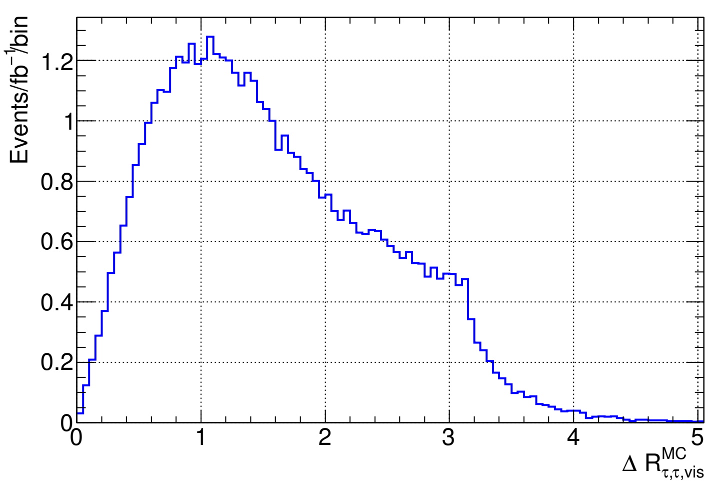

FIGURE 3.4: The truth level distribution of the distance between the coannihilation region signal hard and soft taus. Only the visible components are considered.

Finally Figure 3.5 shows the truth level $M_{\tau,\tau}$ distributions. The blue line show the distribution taking all of the tau energies in to account. We see that there is a nice sharp edge to the distribution, which is similar to those which can arise in the electron and muon channels. The red line shows the distribution taking only the visible tau energy into account. We see that the loss of the neutrino energies smears the distribution backwards, resulting in a very gradual tail towards the endpoint. As we will discuss in Section 7.4 the gradual nature of this endpoint makes the correct determination of it all the more challenging.

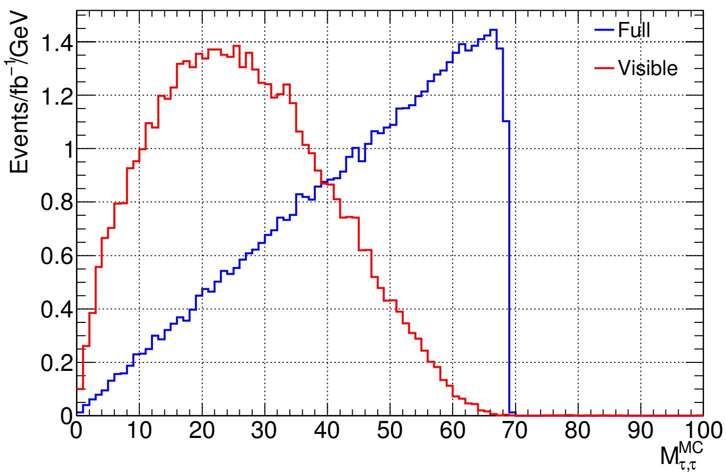

FIGURE 3.5: The truth level $M_{\tau,\tau}$ distribution of the coannihilation region signal hard and soft taus. The blue line shows the distribution using the full tau energies, while the red line shows the distribution using only the visible components of the energies.

Chapter 4

Monte Carlo Simulation and the ATLAS Reconstruction Algorithms

We begin this Chapter with a brief summary of the Monte Carlo simulation programs and samples used for this analysis. We then move quickly on to a description of the physics object reconstruction algorithms used in ATLAS. As emphasised in the previous chapter the most important reconstruction particle for this analysis is the tau lepton. Thus while the descriptions of most of the reconstruction algorithms will be brief, considerable space will be devoted to the description of the ATLAS tau reconstruction algorithm and its performance. The details of this algorithm will set the context for the next chapter which is devoted to the description of the novel soft tau tagging algorithm which has been developed.

4.1 Monte Carlo Simulation

Monte Carlo simulations of LHC physics processes and the subsequent traversal of particles through the ATLAS detector allow for studies of the detector before actual data taking begins. Such things as the optimisation of trigger menus, the optimisation of particle reconstruction algorithms and studies of the discovery potential of the detector can be performed, to a certain extent, before the LHC comes online.

At ATLAS the Monte Carlo simulations and their analyses are performed within the Athena framework [15]. The simulation consists of several steps which are briefly outlined below:

Event Generation

At this step the actual physics processes of the proton-proton collisions of the LHC are simulated. For this study the simulation is done at $E_{CM} = 10$TeV since it was expected that the collision energy would be at this level for some time due to problems with the LHC magnets. A number of Monte Carlo generators are used in Athena providing event simulation of a wide variety of processes. Collision simulation is based on the parton model of the proton where the partons share the proton momentum according to given PDFs. For this study we use Athena version 14.2.20.1 for event generation.

The signal SUSY events for this thesis were generated with a combination of programs. Isajet was used to calculate the weak scale phenomenology of mSUGRA which result from given mSUGRA parameters. These are then used as input to Jimmy and Herwig which together generate the entire underlying event including parton showering and hadronisation.

$t\bar{t}$ events are generated using the MC@NLO package which calculates the matrix elements to next to leading order. These are used as input to Jimmy+Herwig which generate the underlying event.

For W and Z boson processes the Alpgen package was used which creates the parton level interaction. This is then used as input to Jimmy + Herwig which again create the entire underlying event.

Finally QCD processes were simulated using Pythia which is capable of describing the entire hard QCD event.

The Tauola package is used within Athena to describe the decay of tau leptons.

The samples used for this thesis are outlined in Table 4.1. In order to gain enough statistics for this analysis, some private $t\bar{t}$ and $Z \to \nu, \nu$ samples were created with an event filter of $E_T^{miss} > 140$GeV, $P_T^{jet1} > 110$GeV and $P_T^{jet2} > 60$GeV. These filters were sufficiently below the analysis cuts such that the various distributions of non-filter samples matched the filtered samples' distributions well after the analysis cuts were made. Besides the event filter the events were created in exactly the same way as the official ATLAS samples. Further justification of the SM background samples used will be given in Section 6.4.

It should also be noted that, samples which were found to be negligible when cuts were applied to AOD samples were not downloaded/generated at ESD level. These include, for example $Z \to \nu, \nu$ with 0, 1 or 2 partons and $W \to \tau, \nu$ with 0 or 1 parton [1].

[1] These become negligible due to the requirement of 2 jets and a tau for this analysis.

Process	Generator	σ [pb]	Corresponding Lum [fb^{-1}]
SUSY Signal	Herwig	2.58	62.8
$t\bar{t}$, not fully hadronic	MC@NLO	374	21.8
$W \rightarrow \tau, \nu$ + jets	Alpgen	948	1.1
$Z \rightarrow \tau, \tau$ + jets	Alpgen	308	3
$Z \rightarrow \nu, \nu$ + jets	Alpgen	165	7
QCD J4	Pythia	152000	0.0033
QCD J5	Pythia	5129	0.078
QCD J6	Pythia	112	2.90
QCD J7	Pythia	1.08	370
QCD J8	Pythia	0.0011	349k

TABLE 4.1: The Monte Carlo samples used for this analysis.

Detector Simulation and Digitisation

The traversal of the final state particles from the event generation stage through the detector is simulated using the GEANT4 package. A very detailed geometry of the entire detector is used in the simulation, along with empirical magnetic field maps and the results of various subdetector beam tests. The energy deposits of this detector simulation are then converted into digital signals via a digitisation simulation. The output of this is the Raw Data Object (RDO). This is the point at which the simulation data and real data will converge. For this study we use Athena version 14.2.10.1 for the detector simulation and Athena version 14.2.25.8 for the digitisation.

Reconstruction

At this point the RDO needs to be converted in to a form that is meaningful to the end user. This is the job of the reconstruction software. The digital signals of the RDO are reconstructed in to physics objects which can be used for physics analysis. The output of this stage is the Event Summary Data (ESD) or the Analysis Object Data (AOD). The latter is a rarefied and smaller version of the former, and should be the form that most end users analyse. For this study the more detailed ESD was required, since detailed cell-level information of the calorimeter was used. More detailed information of the various reconstruction algorithms is given in the following chapters. For this study we use Athena version 14.2.25.8 for the reconstruction.

4.2 Physics Object Reconstruction

4.2.1 Tracks

As the copious charged particles produced in a collision pass through the inner detector they produce hits in its various components as outlined in Section 2.2.3. These basic data form the basis for track reconstruction which in turn forms the basis for a number of the other reconstruction algorithms, most notably for this analysis the tau reconstruction algorithm. The default track finding algorithm uses the pixel and first SCT layers' hits to identify track candidates which originate from near the interaction point. After a first fitting stage in which fake tracks are rejected the candidate track is propagated through the remaining layers of the inner detectors to find other associated hits. If the track candidate is within the range of the TRT ($|\eta| < 2$) the fit using only the silicon layers is compared to the fit using the both silicon layers and the TRT, and the better of the two is used for the final track reconstruction. All tracks reconstructed as originating from the interaction point are then used in interpolating the primary vertex.

The reconstruction of tau vertices/impact parameters is of particular interest to this study since such information is used to help to identify taus. Also of interest to this study is not only the intrinsic tracking efficiency of pions, but also the charge identification efficiency. These details will be discussed further in Chapters 5 and 6.

4.2.2 Clusters

Clusters are the energy conglomerations which arise when particles enter the electromagnetic and hadronic calorimeters. As with reconstructed tracks, clusters form an important basis for many of the other reconstruction algorithms.

There are two main types of clustering algorithms used in ATLAS. The first type is the so-called "sliding window" algorithm, [16][17] while the second is the so-called "topological clustering" algorithm.[16][18]

While the sliding window algorithm is used by the default electron/photon reconstruction, the newer-to-ATLAS topological clustering algorithm has many exciting possibilities for physics objects with more than one final state particle. Topological clusters are used for the standard ATLAS tau reconstruction algorithms, for the jet reconstruction algorithm used for this analysis and for for the E_T^{miss} calculation. They will also be used for soft tau identification in the soft tau tagging algorithm which will be described in Chapter 5. Thus for this cluster reconstruction review the main focus will be on the topological clustering algorithm.

Sliding Window Clustering

The basic idea of the sliding window clustering algorithm is to create clusters by collecting cells within a given sized cone, and forming a cluster if they collectively pass a certain threshold. This is done in practice by "sliding" a cone of a certain size over the entire calorimeter. If the sum of the energy in the cells passes a certain threshold then the cluster is added to a container. If two clusters are found to overlap within a certain distance then the smaller of the two is discarded.

In ATLAS there are two sliding window algorithms. The first creates EM clusters where only cells from the EM calorimeter are used as input. The second creates hadronic clusters where cells from all of the calorimeters are used. Various particle/jet reconstruction algorithms can use the different sliding window clusters as input, *e.g.* the default electron/photon reconstruction algorithm uses the EM clusters as input.

Topological Clustering

The philosophy employed for the topological clustering algorithm is very different from that of the sliding window algorithm. Its aim is to define the borders of "blobs" of energy in the calorimeter by successively adding neighbouring cells of a given pre-cluster to the pre-cluster if the neighbour has energy over a certain threshold. Three thresholds are defined for the algorithm. In the following E denotes the energy of a cell and σ denotes its noise level.

- **Seed Threshold** Pre-clusters are seeded by cells which have $|E|/\sigma$ above the "seed threshold" (4 for the standard algorithm).
- **Neighbour Threshold** Cells in the pre-cluster which have $|E|/\sigma$ above the "neighbour threshold" are asked for their neighbour cells (2 for the standard algorithm).
- **Cell Threshold** Only cells with $|E|/\sigma$ above the "cell threshold" are added to the pre-cluster (0 for the standard algorithm).

Cells with negative values but for which the absolute value is greater than the thresholds are included in order to avoid a bias from noise.

It can be the case that clusters arising from 2 different particles get merged in to one pre-cluster by this algorithm. Thus a cluster splitting algorithm is employed to split pre-clusters around their maxima. By default maxima are defined as cells with:

- E>500MeV

- Neighbour cells that all have energy less than it
- At least 4 neighbours

A similar procedure is followed to the original topological clustering procedure but now the above defined maxima are used as seeds. Cells at the border of split clusters are shared by each bordering cluster with a weight which is dependant on the distance from each cluster and the energy of each cluster. Only cells that are members of the original topocluster are used.

The power of the topological clustering method is its ability to, for example, separate two clusters which arise from two different particles in the calorimeter when these particles are close together. This is a particular advantage for calorimeters as fine grained as the ATLAS calorimeters. Furthermore noise can be suppressed with judicious choices in the various threshold parameters of the algorithm.[19]

Calibration of clusters

Once calorimeter clusters have been identified the difficult next step is to calibrate them. Calibration though depends on what kind of physics object caused the cluster. The various particle and jet reconstruction algorithms which make use of the clusters have their own calibration schemes and so each do their own calibrations.

The interesting point about the topological clustering though is that, in a region of the calorimeter through which many particles have traversed, individual clusters for each particle can be isolated. Thus for physics objects with more than one final state particle (jets, taus) it is possible to a certain extent to analyse its individual components. Individual components can be identified as EM or hadronic, calibrated accordingly, then have their 4-vectors summed to give the final product. Although this calibration procedure (so-called "Local Hadronic Calibration") is not yet used as the default procedure for any of the particle reconstruction algorithms, its use is being investigated for jet algorithms with topological clusters as inputs and also for E_T^{miss} reconstruction. It is also used by the soft tau tagging algorithm of Chapter 5 as a tool for identifying EM clusters in a tau jet. The calibration proceeds as follows: [19][20]

1. Classify the cluster as EM or hadronic by analysing the shape of the cluster - the various so-called "cluster moments" (see Section 5.1.2.3 for more details)
2. If the cluster is hadronic apply a position and energy dependant e/π weight. If the cluster is EM apply a position and energy dependant detector response correction.
3. Make corrections for upstream and lateral energy losses

The correction factors are derived from single electron and pion MC simulations.

4.2.3 Jets

Being a hadron collider means that the LHC will produce copious QCD jets. Also, as described in Chapter 3, a large jet multiplicity is a characteristic of SUSY events which means that accurate reconstruction of them is important. Furthermore the precise reconstruction of E_T^{miss} is of vital importance to SUSY event discrimination, and accurate jet reconstruction is one of the most critical components of E_T^{miss} reconstruction.

There are a number of jet algorithms employed by the collaboration and each can be supplied with different parameterisations, different inputs and different split/merge mechanisms [21]. For reconstruction of jets in this thesis only the so-called "seeded cone algorithm" was used with a cone size of 0.4 and topological clusters as input (Athena container name:`Cone4H1TopoJets`, henceforth *TopoJets*). This algorithm takes high E_T topological clusters as seeds and adds the 4 momentum of the clusters in a cone of 0.4 around its η, ϕ direction. It then calculates a new η, ϕ direction from this 4 momentum sum and iterates this procedure until the difference between the initial and final directions falls below a certain threshold *i.e.* a stable jet is found. After all of the seeds have been used it may be the case that some jets overlap. If this is the case then the following split/merge procedure is followed: If the two overlapping jets share more than 50% of the E_T of the lower E_T jet, then the 2 jets are merged. If it is less than 50% then each overlapping cell is associated to the jet to which it is the closest in direction. Only jets with $p_T > 7.5$GeV are finally stored.

For this algorithm the so called "H1" global calibration scheme is employed which is the default for ATLAS jet calibration. The basic idea of this method is that energy depositions from EM particles should have a relatively high density compared to those from hadrons. Thus each cell in a jet is weighted by a factor which is a function of its energy density, and to correct for position dependence, its position. These functions have been determined by minimising the resolution of jets in Monte Carlo simulations with respect to the Monte Carlo truth particles. Residual non-linearities in p_T and η are further corrected with an additional calibration function of these variables.

4.2.4 Electrons

Although, along with muons, electrons are of secondary importance to this analysis, they still must be reconstructed efficiently since a lepton veto will be applied[21].

Standard electron reconstruction is seeded by EM sliding window clusters. Various corrections for position dependant responses and upstream losses are applied. A match to a reconstructed track with $E/p < 10$ is attempted and if one is found that has not been flagged as a conversion track then the cluster track pair are electron candidates. Stringent rejection of up to 10^5 against jets faking electrons is required by many analyses and so various cut regimes are in place to achieve rejection up to this level. They comprise cuts on various parameters derived from both the inner detector and the calorimeters. Typical efficiencies for electrons with $E_T > 17GeV$ with “medium” cuts are 77% for a rejection factor of about 2000.

4.2.5 Muons

Muons are one of the easier SM particles to identify in the ATLAS detector due to the fact that they are the only SM charged particle which will reach past the calorimeters with any great efficiency. Many interesting physics events contain high p_T isolated muons which originate from the interaction point while non-interesting events do not so much. The ability to select such muonic events purely thus makes them a good flag for some interesting events. On the other hand, for this analysis they will be used to veto SUSY-like background events which contain muons.

The standard muon reconstruction algorithm in ATLAS begins by reconstructing track segments within each of the three stations of the muon system. These are then linked together to form muon tracks. These are then extrapolated through to the interaction point, taking in to account both energy losses and multiple scattering in the calorimeter. A matching track from the inner detector track reconstruction is then found and a combined fit is performed. The quality of this entire fit determines whether the pair is kept as a “good” muon candidate. Standard background to “good” muons are both actual muons which come from π and K decays (which do not originate from the interaction point), and also low energy photons and neutrons coming from cavern background. Cavern background depends strongly on beam luminosity. Typical efficiencies for “good” muons in a J/ψ sample are at the level of 76% with a fake rate of ≈ 1 per 1000 events when a $p_T >$ 10GeV cut is made. Most of the inefficiency arises from areas in η with bad coverage from the muon system.

4.2.6 Missing Transverse Energy

As mentioned previously a precise E_T^{miss} measurement is of vital important for not only SUSY searches but for most new physics searches. True E_T^{miss} is the imbalance in the vectorial sum of E_T which arises from particles such as neutralinos and neutrinos escaping the detector. E_T^{miss} is measured by the default algorithm by summing the E_T of H1-calibrated calorimeter topoclusters and reconstructed muons. Muon energy deposited in the calorimeter is then corrected for. Furthermore calibration of cells associated to high p_T physics objects (electrons, taus etc.) are refined using the calibration schemes of the respective reconstruction algorithms. Finally energy loss arising in the cryostat between the EM and hadronic calorimeters is corrected for.

Fake E_T^{miss} can arise in the detector from a number of sources which all degrade the E_T^{miss} resolution. These include:

- High energy particles escaping down the very forward regions of the detector.
- Poor reconstruction of particles passing through other bad-coverage areas of the detector (e.g. crack region).
- Poor resolution of deposited energy in regions with large amounts of dead material before the calorimeter.
- Dead regions of the detector.
- Inefficiencies in muon detection and fake muons.
- Noise arising from intrinsic calorimeter noise.
- Noise arising from pile-up conditions.

The ATLAS detector is designed to avoid as much as possible energy loss in the forward regions as described in Chapter 2. Nevertheless some very forward particles will be able to escape down the beam pipe and such losses are unavoidable.

As much as possible corrections for energy losses in poorly instrumented areas of the detector and regions with large amounts of dead material are corrected using factors derived from Monte Carlo simulation.

Instrumental noise is difficult to study with Monte Carlo simulation but it is expected that refined analyses taking in to account such effects will be developed as the understanding of the detector is improved with run-time.

Most fake E_T^{miss} arising from muons comes from missed real muons rather than from fake muons. These muons are missed, as mentioned above, predominantly in the regions of bad coverage by the muon system. These contribute significantly to non-gaussian tails in the E_T^{miss} resolution. Work is underway to recover such lost muons with algorithms using inner detector tracks and calorimeter deposits as seeds.

Intrinsic calorimeter noise from the ≈200k calorimeter channels alone contributes a constant factor of around 13GeV to the E_T^{miss} resolution. Compared to a simple E/σ cut on calorimeter cells, using cells from the standard topocluster algorithm suppresses both intrinsic calorimeter noise and soft pile-up noise significantly.

4.2.7 Standard Tau Reconstruction with `tauRec`

The final and most pertinent reconstruction for this analysis is for tau leptons. Taus play an important role in many analyses at the LHC. For the case that the mass of the Higgs is only slightly above the present exclusion region the decay to taus becomes important. Also, for many regions of the mSUGRA phase space including the co-annihilation region, the τ Yukawa coupling becomes large and $\tilde{\tau}_1$ becomes lighter than its first and second generation counterparts meaning that $\tilde{\chi}_2^0$ decaying to $\tilde{\tau}$ becomes predominant.[11]

4.2.7.1 Tau Decay Topology

As outlined in Section 1.1.4 tau decays can be generally divided in to two types; hadronic modes and leptonic modes. The leptonic mode visible products (electron 17.8% and muon 17.4%) are too difficult to distinguish from primary leptons of the event and so tau reconstruction at ATLAS focusses on the hadronic modes only. These can be further divided in to single prong (1 $\pi^{\pm}$, 70% of hadronic) and three prong (3 $\pi^{\pm}$, 21% of hadronic) modes, each of which can also have some number of π^0s associated to it (refer to Table 1.2). There are a small number of modes containing 5 $\pi^{\pm}$ but it is believed that attempting to identify these would lead to an unacceptable level of QCD background. Also a small fraction of analogous $K^{\pm}$ modes exist but these will be identified along with their $\pi^{\pm}$ counterpart decay modes and so not special attention to them is necessary.

There are a number of challenges when it comes to tau reconstruction. The first and most obvious is the fact that taus have a tau neutrino as a final state particle meaning that a substantial fraction of the tau energy is lost from the detector. Tau reconstruction then focuses only on the visible information of the tau.

A second challenge for hadronic tau reconstruction, especially at a hadron collider, is the rejection of copious QCD jets. Compared to a QCD jet a tau-jet is rather well collimated since the opening angle of its decay products will be limited to m_τ/E_τ. In the inner detector the tau system will appear as an isolated low track multiplicity collimated system with none of the tracks having any characteristics of an electron (e.g. high threshold TRT hits) or a muon (little energy deposition in the calorimeters). There should be 1 or 3 "good " tracks [2] , the invariant mass of the tracks should be less than the tau mass and the absolute value of the sum of their charges should be equal to unity. Furthermore the tau has a finite decay length which can result in a significance in the size of the impact parameter which can be used to identify them as a tau. In the calorimeter the energy should be well collimated and isolated with possibly a large EM component for the case of decays to π^0s. On average about 55% of the energy of taus is carried by π^0 decay products.

4.2.7.2 The `tauRec` algorithm reconstruction

There are two distinct approaches to tau reconstruction used in ATLAS and each approach is seeded by one of the two different manifestations in the detector of the tau decay described above.[22][23]

- The calorimeter seeded approach is seeded by the *TopoJets*.
- The track seeded algorithm is seeded by a small number of "good" tracks.

The two approaches have their own individual merits but their combined performance is better than either one individually. We will outline the two algorithms below and how they have recently been combined in to a single algorithm(`tauRec`)[3] in order to optimise overall tau reconstruction performance. Further ahead in Section 4.3 I will discuss their combined performance in the mSUGRA co-annihilation point of this analysis.

The track seeded approach begins with "good" tracks as defined in the second column of Table 4.2. The main thrust of these cuts is to make sure that fake tracks as well as secondary tracks arising from hadronic interaction in the inner detector are rejected. Tracks of somewhat less stringent quality are then associated to the seed track if they are within a cone of $\Delta R < 0.2$. The quality cuts for these tracks are defined in the third column of Table 4.2. A lower p_T cut for these tracks is offset by a requirement of a B layer hit in the tracker. Also the B-layer hit and the cut on the ratio of high to low threshold hits in the TRT aims to reduce contamination from conversion electrons coming from π^0 decay photons. In the case that the candidate has a total of two tracks, a third track is searched for by dropping the χ^2 and $N^{HT}_{TRT}/N^{LT}_{TRT}$ requirements. This track is only added to the seed if it makes $|\sum Q| = 1$.

[2] "Good" track will be defined below but it suffices to say for now that it means a track that comes from very close to the interaction point, and not from photon conversion.

[3] Historically the calorimeter seeded algorithm was known as `tauRec` while the track seeded algorithm was known as `tau1p3p`. Since Athena version 14 these two algorithms have been combined in to a single tau reconstruction algorithm named `tauRec`.

Track criteria	Seed track	Associated track	Loose track
p_T [GeV]	6	1	1
$\lvert\eta\rvert <$	2.5	2.5	2.5
Impact parameter d_0[mm] $<$	1	1	1.5
Silicon Hits $N_{si} \geq$	8	8	6
TRT hits $N_{TRT} \geq$ (when $\lvert\eta\rvert < 1.9$)	10	no cut	no cut
Normalised $\chi^2 <$	1.7	1.7	3.5
Pixel Hits $N_{pixel} \geq$	no cut	1	1
B-layer hits $N_{blay} \geq$	no cut	1	no cut
High/Low threshold hit ratio $N^{HT}_{TRT}/N^{LT}_{TRT} <$	no cut	0.2	no cut

TABLE 4.2: Track quality criteria for the track seeded algorithm (Seed track and Associated track) and for the calorimeter seeded algorithm (Loose track) of `tauRec`.

The calorimeter seeded approach begins with H1 calibrated *TopoJets*. Only *TopoJets* with $E_T > 10$GeV and $|\eta| < 2.5$ are used. Tracks which pass certain quality cuts are associated to the seed if they are within a cone of radius $\Delta R < 0.3$ of the *TopoJet*. These track quality cuts are shown in the fourth column of Table 4.2.

Now for the case that a track seeded tau is matched to within $\Delta R < 0.2$ of a calorimeter seeded tau, only one candidate is built. Thus candidates can be calorimeter seeded, track seeded or they can have both seeds. For the case that they have both seeds (most candidates have both seeds) the best parts of the original two algorithms have been used to optimise the reconstruction. The following will describe the methods used for energy and direction calculations, and the method for tau discrimination, for each of the three cases.

Energy calculation

Firstly if the candidate has a calorimeter seed its energy is calculated entirely from calorimeter information. This is the approach of the original calorimeter based algorithm and in general has superior performance compared to the track based method. The H1 calibration scheme used for QCD jets (Section 4.2.3) is initially used to correct the *TopoJet* to the hadronic scale. This calibration scheme though has been optimised for QCD jets which have a significantly different EM component from taus, thus an extra correction for the tau energy level has been derived as a function of E_T, η and the number of tracks associated to the tau candidate, by comparing Monte Carlo information with the reconstructed taus.

For the case that the candidate is only track seeded a so-called energy flow approach is used. This was originally contrived as a means of improving the energy resolution of low p_T taus by using the track information as well as the calorimeter information. First the different components of the tau energy in the calorimeters are separated as follows:

- The pure EM energy, E_T^{emcl}, which is seeded by an isolated EM cluster
- The charged EM and hadronic energies, E_T^{chrgEM} and $E_T^{chrgHAD}$ seeded by the impact point of the track(s) is each layer of the calorimeter
- The neutral EM energy, E_T^{neut}, seeded by the vertex direction of the tau seed track. Only cells not used for the collection of the above two contributions are used.

Note that only cells within $\Delta R < 0.2$ of the leading track are used in the following: The general idea is to first remove the contribution of the $\pi^{\pm}$ from the calorimeter and then add up the rest of the energy assuming that it comes from π^0s. In practice this is done by removing the energy in a cone of $\Delta R < 0.0375$ around the track(s) in the EM calorimeter (E_T^{chrgEM}), and in a cone of $\Delta R < 0.2$ in the hadronic calorimeter, and then replacing this with the p_T of the track(s). The cone used for the EM calorimeter is small in order to avoid removing π^0 energy as much as possible. This of course is not a consideration for the energy in the hadronic calorimeter. Following this step isolated EM clusters are searched for (E_T^{emcl}). These are required to have little hadronic leakage and must be outside the $\Delta R < 0.0375$ cone described above. These correspond to π^0 which are well separated from their charged counterparts in the calorimeter. It is not always the case that $\pi^{\pm}$ and π^0 are well separated in the calorimeter though, so any cells that have not been used in the previous two steps, and which are in a cone of $\Delta R < 0.2$ of the position of the *track at the vertex*, are added up at the EM scale in order to account for non-isolated π^0 contributions. Also some factors accounting for π^0 energy leakage in to the $\pi^{\pm}$ cone, and for $\pi^{\pm}$ energy leaking outside of the cone are corrected for with factors $\sum \mathrm{res}E_T^{chrgEM}$ and $\sum \mathrm{res}E_T^{neutEM}$. These are calculated by comparing p_T^{track} with E_T^{chrgEM} to check for leakage of hadronic energy outside the small collection cone, and also comparing p_T^{track} with E_T^{neutEM} to check for whether neutral energy is large enough to assume that a substantial amount has leaked in to the collection cone.[24]

Thus the energy is summed as:

$$E_T^{eflow} = E_T^{emcl} + E_T^{neut} + \sum p_T^{track} + \sum \mathrm{res}E_T^{chrgEM} + \sum \mathrm{res}E_T^{neutEM} \tag{4.1}$$

Direction calculation and charge/number-of-tracks reconstruction

For the direction calculation the track seeded approach is given precedence. For candidates with a track-seed the direction of the tau candidates is calculated from the direction of the track at its vertex for single track candidates, and the p_T-weighted barycentre for the case of multi-track candidates. For candidates with only a calorimeter seed, the direction is calculated as the E_T-weighted barycentre of the calorimeter cells of the *TopoJet*s. The charge of the candidate is calculated as the simple sum of its associated tracks, where again the tracks from the track seed are given precedence.

4.2.7.3 The `tauRec` algorithm discrimination

Identification of taus in `tauRec` is performed by calculating a number of variables. These variables are designed to exploit the tau characteristics and they focus on such factors as the narrowness of the tau-jet, the isolation of the tau track system and the finite path length of the tau before decay. The variables are listed below:

DISCRIMINATION VARIABLES FOR CALORIMETER SEEDED CANDIDATES

- **The electromagnetic radius** R_{em}:

  The electromagnetic radius R_{em} is defined as

  $$R_{\mathrm{em}} = \frac{\sum_{i=1}^{n} E_{T,\,i}\sqrt{(\eta_i - \eta_{\mathrm{axis}})^2 + (\phi_i - \phi_{\mathrm{axis}})^2}}{\sum_{i=1}^{n} E_{T,\,i}}, \tag{4.2}$$

  where i runs over all cells associated to the tau within a cone of $\Delta R < 0.4$ of the tau axis. It can be thought of as an energy weighted width of the tau in the EM calorimeter.

- **The Hadronic radius** R_{had}:

  The hadronic radius R_{had} is defined as

  $$R_{\mathrm{had}} = \frac{\sum_{i=1}^{n} E_{T,\,i}\sqrt{(\eta_i - \eta_{\mathrm{axis}})^2 + (\phi_i - \phi_{\mathrm{axis}})^2}}{\sum_{i=1}^{n} E_{T,\,i}}, \tag{4.3}$$

  where i runs over all cells associated to the tau within a cone of $\Delta R < 0.4$ of the tau axis. It can be thought of as an energy weighted width of the tau in the hadronic calorimeter.

- E_T **over** p_T **of the leading track:** E_T/p_T^{trk1} :

  The ratio of the E_T of the tau to the p_T of the leading track. The leading track of a tau decay carries a relatively large fraction of the tau energy.

- **Number of hits in the η strip layer**:

  The number of hits in the finely segmented first layer of the EM calorimeter with E>200MeV and within $\Delta R < 0.4$ of the tau axis are counted. Only tau decays with π^0 are expected to deposit significantly in this layer and even these should have a small number of hits compared to a QCD jet.

- **Lifetime signed pseudo impact parameter significance**:

  The transverse impact parameter is defined as the distance of closest approach of the leading track to the beam axis, in the plane perpendicular to the beam axis. This distance is divided by the impact parameter resolution which is calculated from all primary tracks. This gives a significance of the parameter. Also, if the vector defined as being perpendicular from the beam axis, and pointing in the direction of the point of closest approach of the track, "faces away" from the track direction, then the sign of this quantity is made negative, otherwise positive. A tau's leading track is expected to "face" the same way as the direction in which the pre-decay tau moved (and thus the lifetime signed pseudo impact parameter should be positive for a tau).

- **Isolation fraction in the calorimeter, I**:

  The isolation fraction is defined as

  $$I = \frac{\sum_i E_{T,i}^{0.1<\Delta R<0.2}}{\sum_j E_{T,j}^{\Delta R<0.4}}, \tag{4.4}$$

  where the i and j run over all EM calorimeter cells in a cone around the tau axis with $0.1 < \Delta R < 0.2$ and $\Delta R < 0.4$, respectively, and $E_{T,\,i}$ and $E_{T,\,j}$ denote the cell E_T. Taus are expected to have a small isolation fraction.

- **Transverse energy width in the η strip layer, $\Delta\eta$**:

  The transverse energy width $\Delta\eta$ is defined as

  $$\Delta\eta = \sqrt{\frac{\sum_{i=1}^{n} E_{Ti}^{\text{strip}} \left(\eta_i - \eta_{\text{axis}}\right)^2}{\sum_{i=1}^{n} E_{Ti}^{\text{strip}}}}. \tag{4.5}$$

  where the sum runs over all strip cells in a cone with $\Delta R < 0.4$ around the tau axis and E_{Ti}^{strip} is the corresponding strip transverse energy. This is another quantity measuring energy narrowness, but using only the finely-segmented-in-η strip layer of the EM calorimeter, and only in the η direction.

- **Transverse flight path significance, L_{xy}/σ_{Lxy}**:

For candidates with more than one track associated to them, the tracks' vertex is reconstructed. The transverse flight path significance is defined as the transverse distance of this vertex from the primary vertex L_{xy}, divided by its uncertainty σ_{Lxy}.

- **Centrality fraction in the calorimeter,** C_{frac}:

  The centrality fraction is defined as

$$C_{frac} = \frac{\sum_i E_{T,\,i}}{\sum_j E_{T,\,j}}, \tag{4.6}$$

  where the i and j run over all EM calorimeter cells in a cone around the tau axis with $\Delta R < 0.1$ and $\Delta R < 0.4$, respectively, and $E_{T,\,i}$ and $E_{T,\,j}$ denote the cell E_T. This is another isolation parameter.

Figures showing examples of the distributions of these variables for the process $W \to \tau, \nu$, and for background J2 samples can be found in Appendix A.

DISCRIMINATION VARIABLES FOR TRACK SEEDED CANDIDATES

- **Ratio of the hadronic energy to the sum of the tracks' transverse momenta,** $E_T^{chrgHAD} / \sum p_T^{trk}$:

  Ratio of the energy in the hadronic calorimeter (EM scale) in $\Delta R < 0.2$ of the tau direction to the sum of the tracks' p_T

- **The electromagnetic radius,** $EMradius$:

  Similar to R_{em} for the calorimeter seed except calculated with respect to the track derived direction

$$EMradius = \frac{\sum_{i=1}^{n} \Delta R_i E_{T,\,i}}{\sum_{i=1}^{n} E_{T,\,i}}, \tag{4.7}$$

  where i runs over all cells associated to the tau within a cone of $\Delta R < 0.4$ of the track derived tau axis.

- **Isolation fraction in the isolation region,** $EtIsolFrac$:

  The isolation fraction in the isolation region is defined as

$$EtIsolFrac = \frac{\sum_i E_{T,\,i}}{\sum_j E_{T,\,j}}, \tag{4.8}$$

  where the i and j run over all EM calorimeter cells in a cone around the tau axis with $0.2 < \Delta R < 0.4$ and $\Delta R < 0.4$, respectively, and $E_{T,\,i}$ and $E_{T,\,j}$ denote the cell E_T. This is similar to C_{frac}, but the inverse quantity, with slightly different cone size.

- **The invariant visible mass** , $M_{invariant}$:

  $M_{invariant}$ is defined as the invariant mass calculated with the tracks, and the 4-momentum of E_T^{emcl} (which should correspond to π^0).

- **Fraction of transverse energy in the isolation region,** $IsolationFraction$

  $IsolationFraction$ is defined as

$$IsolatinFraction = \frac{\sum_i E_{T,i}}{\sum_j E_{T,j}}, \tag{4.9}$$

  where the i and j run over all both EM and hadronic calorimeter cells in a cone around the tau axis with $0.1 < \Delta R < 0.2$ and $\Delta R < 0.2$, respectively, and $E_{T,i}$ and $E_{T,j}$ denote the cell E_T. This quantity is similar to the calorimeter seed quantity I, except that cells from both EM and hadronic calorimeter are used and the cone sizes differ.

- **Number of tracks,** N_{trk}^{core}:

  The number of tracks associated to the tau within a cone of $\Delta R < 0.2$ of the tau.

- **Associated tracks in isolation region,** N_{trk}^{isol}:

  The number of tracks associated to the tau within the region $0.2 < \Delta R < 0.4$ of the tau.

- **Number of calorimeter strips,** $N_{\eta-strip}^{hits}$:

  The same quantity as "Number of hits in the η strip layer" defined for the calorimeter seed above, except calculated with respect to the track derived direction.

- **Width of the energy in strips,** $(\Delta\eta)^2$:

  Similar to the "transverse energy width in η strip layer" defined for the calorimeter seeded tau above, except that the width is now defined as the variance in the η coordinate, weighted by the transverse energy in a given strip.

$$(\Delta\eta)^2 = \frac{\sum_{i=1}^{n} E_{Ti}^{\text{strip}} \left(\eta_i - \eta_{\text{axis}}\right)^2}{\sum_{i=1}^{n} E_{Ti}^{\text{strip}}} - \frac{\left(\sum_{i=1}^{n} E_{Ti}^{\text{strip}} \left(\eta_i - \eta_{\text{axis}}\right)\right)^2}{\left(\sum_{i=1}^{n} E_{Ti}^{\text{strip}}\right)^2} \tag{4.10}$$

  where the sum runs over all strip cells in a cone with $\Delta R < 0.4$ around the tau axis and E_{Ti}^{strip} is the corresponding strip transverse energy.

- **The invariant mass of the tracks,** M_{trk}:

  M_{trk} is defined as the invariant mass of the tracks associated to the tau (for candidates with more than one track).

- **Transverse flight path significance,** L_{xy}/σ_{Lxy}:

  Exactly the same as for the calorimeter seed, except that tracks come from the track seeded algorithm.

- **Width of tracks,** $TrackWidth$:

  $TrackWidth$ is defined as the variance in the η coordinate over the tracks, weighted by the p_T of the tracks (for candidates with more than one track)

$$TrackWidth = \frac{\sum_{i=1}^{n} p_{Ti}^{\mathrm{trk}} \left(\eta_i - \eta_{\mathrm{axis}}\right)^2}{\sum_{i=1}^{n} p_{Ti}^{\mathrm{trk}}} - \frac{\left(\sum_{i=1}^{n} p_{Ti}^{\mathrm{trk}} \left(\eta_i - \eta_{\mathrm{axis}}\right)\right)^2}{\left(\sum_{i=1}^{n} p_{Ti}^{\mathrm{trk}}\right)^2} \tag{4.11}$$

  where the sum runs over all tracks associated to the tau.

Figures comparing these variables for the ATLAS Tau Working Group benchmark process $W \to \tau, \nu$, and for background QCD jets, can be found in Appendix A.

There are a number of ways to use these variables for discrimination. A so-called "safe" cut based method will be used during early running stages of the experiment but as understanding of the detector is improved a better performing multi-variate method will be used. Probability density functions (PDFs) for tau signal and QCD background have been created by the ATLAS Tau Working Group with high statistics from $Z \to \tau, \tau$ Monte Carlo simulations, and from QCD simulations respectively. These PDFs were binned in $p_{T,vis}$ in order to take account of the change in their shape in the different energy regions. Then when a tau candidate is reconstructed by `tauRec`, these PDFs are used to create a likelihood variable for the candidate as described below.

In tauRec the following variable is constructed for each tau candidate:

$$d = \sum_{k=1}^{k=nVars} \log \frac{p_k^S(x_k)}{p_k^B(x_k)} \tag{4.12}$$

where the sum is over the discrimination variables described above, x_k is the value of the variable k for the candidate, and $p_k^S(x_k)$ and $p_k^B(x_k)$ are the probability density at the value x_k for the signal PDF and for the background PDF respectively. It is easy to see that, when the probability density returned from the signal PDF is higher than that from the background PDF for some variable, the contribution to the summation will be positive. Otherwise it will be negative. Thus the variable d gets pushed in the positive direction when the value for a variable is more tau-like, and in the negative direction when the value for a variable is background-like.

Because this likelihood method has been trained for rejecting QCD jets, on its own, it does not perform well for electron rejection. For this purpose there has been a separate electron veto developed. The electron veto is a similar likelihood algorithm which is applied only when the tau candidate is a single track candidate. The algorithm performs better than a simple electron-tau overlap removal procedure, yielding an electron efficiency of 5% for a tau efficiency of 95% for taus arising from $Z \to \tau\tau$ decay. For muon rejection a simple requirement of $E > 5$GeV in the calorimeter around the leading track is required.

4.3 `tauRec` performance in the mSUGRA coannihilation region

The following section outlines studies undertaken on the performance of the `tauRec` algorithm in the mSUGRA coannihilation region. It will begin with giving the quality of the kinematic reconstruction of the taus, and finish with the algorithm's rejection power. We will see that while `tauRec` performs well for reconstructing and identifying taus with $P_{T,vis} > 20$GeV, its performance in the low energy region is poor. As was outlined in Chapter 3, for this analysis, reconstruction and identification of low energy taus is vital. A number of lessons were learnt from the performance of `tauRec` in the low energy region which formed the basis for the development of a soft tau tagging algorithm. This algorithm is the subject of the next chapter.

In the following `tauRec` reconstruction of true taus in the coannihilation region, and fake taus in QCD di-jet samples are compared. The following matching conditions are used.

- True taus are considered as reconstructed by `tauRec` if the truth level visible component is matched to a `tauRec` object within $\Delta R < 0.2$.
- Fake taus are considered as reconstructed by `tauRec` if the truth level jets are matched to `tauRec` objects within $\Delta R < 0.4$

Furthermore, comparison is made between soft object reconstruction and hard object reconstruction. For this purpose a soft object is defined as an object with $p_{T,vis} <$ 20GeV, while a hard object is defined as an object with $p_{T,vis} > 20$GeV.

4.3.1 Prong multiplicity and charge reconstruction

Correct reconstruction of the charge of tau candidates is important for this analysis. Subtracting same sign pairs of tau candidates from opposite sign pairs of tau candidates helps to reduce the background from the $M_{\tau,\tau}$ distribution, as will described in Chapter 6.

Figure 4.1 shows the distribution of the number of tracks associated to `tauRec` objects for true taus and fake taus, separately for soft objects ($p_T < 20$GeV), and hard objects ($p_T > 20$GeV). The ratio of 3-prong candidates to 1-prong candidates for true taus is expected to be 30%. The reconstructed ratio is $15.0 \pm 0.2\%$ for soft candidates matched to true taus, and $31.9 \pm 0.2\%$ for hard candidates matched to true taus. Thus we can see that while the track multiplicity ratio is reconstructed quite well for harder taus, it is about half of what it should be for soft taus, due to inefficiencies in reconstructing the soft tracks of 3 prong taus. The QCD spectrum is smooth with peaks at 1 for soft jets and at 3 for hard jets.

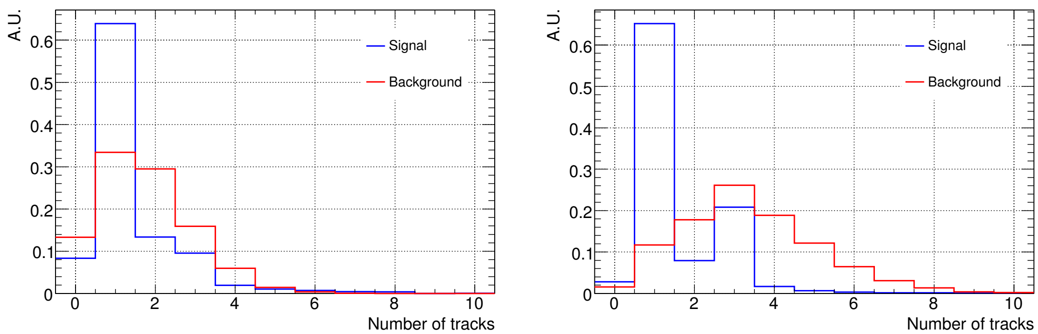

FIGURE 4.1: The track multiplicity of `tauRec` objects. The left hand plot shows the multiplicity of objects with reconstructed $p_T < 20$GeV, while the right hand plot shows the multiplicity for objects with $p_T > 20$GeV. The multiplicities for fake taus (from a J2 QCD sample) and real taus (from a coannihilation sample) are shown superimposed.

As mentioned above, `tauRec` reconstructs the charge of the tau candidate simply as the sum of the charges of the associated tracks. Table 4.3 shows the migration of 1 and 3 prong true taus in to other track multiplicity categories. Results for soft taus and hard taus are shown separately. For hard taus, 1 prong taus are reconstructed with 1 track 83.6% of the time, while 3 prong taus are reconstructed with 3 tracks 71.4% of the time. For soft taus, 1 prong taus are reconstructed with 1 track 74.7% of the time, while 3 prong taus are reconstructed with 3 tracks 41.0% of the time. Again we see the inefficiency of track reconstruction for soft taus significantly reducing the number of correctly reconstructed 3-prong candidates.

Complimentary to Table 4.3 is Table 4.4 which shows the charge misidentification for true taus which have been reconstructed with 1 or 3 tracks. We focus only on taus reconstructed with 1 or 3 tracks since this is a standard identification cut for taus for reducing background and charge misidentification. Results for soft taus and hard taus are shown separately. We can see that for hard taus, the rate of charge misidentification is

	Reconstructed as 1-track	Reconstructed as 2-track	Reconstructed as 3-track	Reconstructed as 3-track>
TAUS WITH $p_{T,vis}^{MC} < 20$GeV				
one-prong	74.7%	8.6%	2.9%	3.8%
three-prong	13.2%	36.1%	41.0%	9.0%
TAUS WITH $p_{T,vis}^{MC} > 20$GeV				
one-prong	83.6%	6.8%	3.8%	2.1%
three-prong	10.8%	11.4%	71.4%	6.3%

TABLE 4.3: Migration of true one and three prong taus from a coannihilation region sample into other prong categories with `tauRec`. Statistics are shown for taus with $p_{T,vis}^{MC} < 20$GeV and $p_{T,vis}^{MC} > 20$GeV separately.

	Reconstructed as 1-track	Reconstructed as 3-track
TAUS WITH $p_{T,vis}^{MC} < 20$GeV		
Correct Q	95.7%	85.5%
Incorrect Q	4.3%	14.5%
TAUS WITH $p_{T,vis}^{MC} > 20$GeV		
Correct Q	96.5%	92.9%
Incorrect Q	3.5%	7.1%

TABLE 4.4: Charge misidentification for `tauRec` objects reconstructed with 1 or 3 tracks and matched to true taus from a coannihilation region sample. Statistics are shown for taus with $p_{T,vis}^{MC} < 20$GeV and $p_{T,vis}^{MC} > 20$GeV separately.

3.5% for taus reconstructed with 1 track and 7.1% for taus reconstructed with 3 tracks. For soft taus this increases to 4.3% for taus reconstructed with 1 track, and 14.5% for taus reconstructed with 3 tracks. Charge misidentification arises from a combination of effects. Single prong tau charge misidentification may arises from π^0 decay gamma ray conversion electrons being associated to the tau, or from track contamination from the underlying event. On the other hand 3 prong tau charge misidentification may arise from inefficient reconstruction of softer tracks combined with conversion electrons being associated to the tau and also from event contamination. Inherent charge misidentification of individual tracks also plays a role.

From Figure 4.1 it is obvious that requiring that hard `tauRec` objects have exactly one or three associated tracks will significantly reduce the QCD background. Requiring an odd number of tracks is also necessary for obtaining a meaningful charge for the tau. The requirement of 1 or 3 tracks will be used as one of the identification cuts for the coannihilation region signal hard tau further ahead. For softer taus we can see that allowing only 1 prong candidates to pass can reduce the QCD background significantly. Allowing 3 prong candidates is likely to introduce much more background from jets.

4.3.2 Energy reconstruction

Figure 4.2 shows plots of the p_T resolution for the two different algorithms of `tauRec`, with the resolutions of true soft taus and true hard taus superimposed. Since the energy reconstruction of the calorimeter seeded algorithm takes precedence over that of the track seeded algorithm, the track seeded resolution is for candidates which *only* have a track seed.

We can see that the calorimeter seeded algorithm resolution peak is shifted by a few percent to the positive for both hard and soft taus. This is due to the quite large energy collection area (0.4 cone) used. For the busy environment of a SUSY event this tends to be contaminated with other energy. Further evidence of this is the high end tail which is present. On the other hand we see that the track seeded algorithm, which is more selective about the energy it uses, has a well placed peak for hard taus but a slightly positive shifted peak for soft taus. The positive shifted peak for soft taus is likely to arise from energy double counting in its energy flow method. High end tails still exist for the track seed method. For the calorimeter seeds, a gaussian fit of the peaks yields σs of 18% and 7% for soft and hard taus respectively, while for the track seeds these are 15% and 8%.

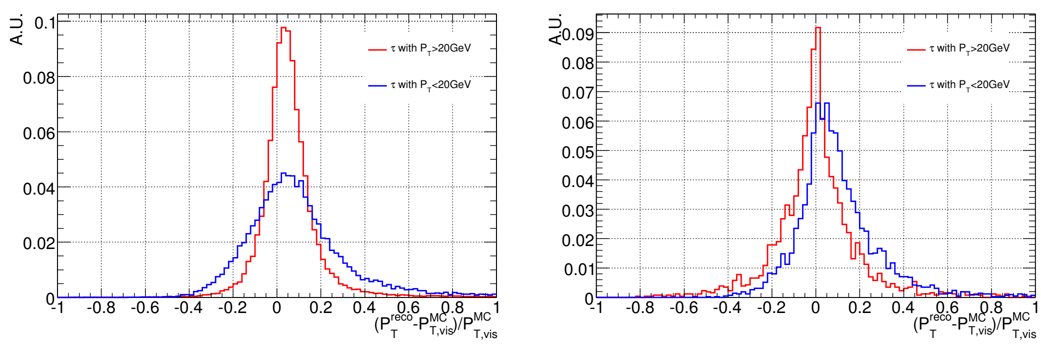

FIGURE 4.2: The p_T resolutions for the true taus reconstructed by the `tauRec` algorithm in a SUSY coannihilation region sample. The left hand plot shows the resolution for the calorimeter seeded algorithm while the right hand plot shows the resolution for the track seeded algorithm. The red lines are taus with $p_{T,vis} < 20$GeV while the blue lines are taus with $p_{T,vis} > 20$GeV.

Figure 4.3 shows the p_T linearity of the `tauRec` reconstruction as functions of $p_{T,vis}^{MC}$, η_{vis}^{MC} and ϕ_{vis}^{MC} for all true taus (no separation of hard and soft taus). The linearity is shown separately for the calorimeter seeded algorithm and the track seeded algorithm. We can see, as shown also by the resolution plot of Figure 4.2, that the calorimeter seeded algorithm suffers from a positive shift in the reconstructed p_T. It becomes worse at lower p_T when contamination from the rest of the event may become relatively more significant. The track seeded algorithm also significantly overestimates p_T in the lower

p_T region, most probably from problems with double counting and contamination, while at higher p_T it underestimates the energy, likely due to π^0 energy being subtracted along with $\pi^{\pm}$ energy in the $\pi^{\pm}$ energy subtraction step. The linearity as a function of η_{vis}^{MC} shows distortions in the crack regions of the calorimeter, while in ϕ_{vis}^{MC} it is fairly uniform.

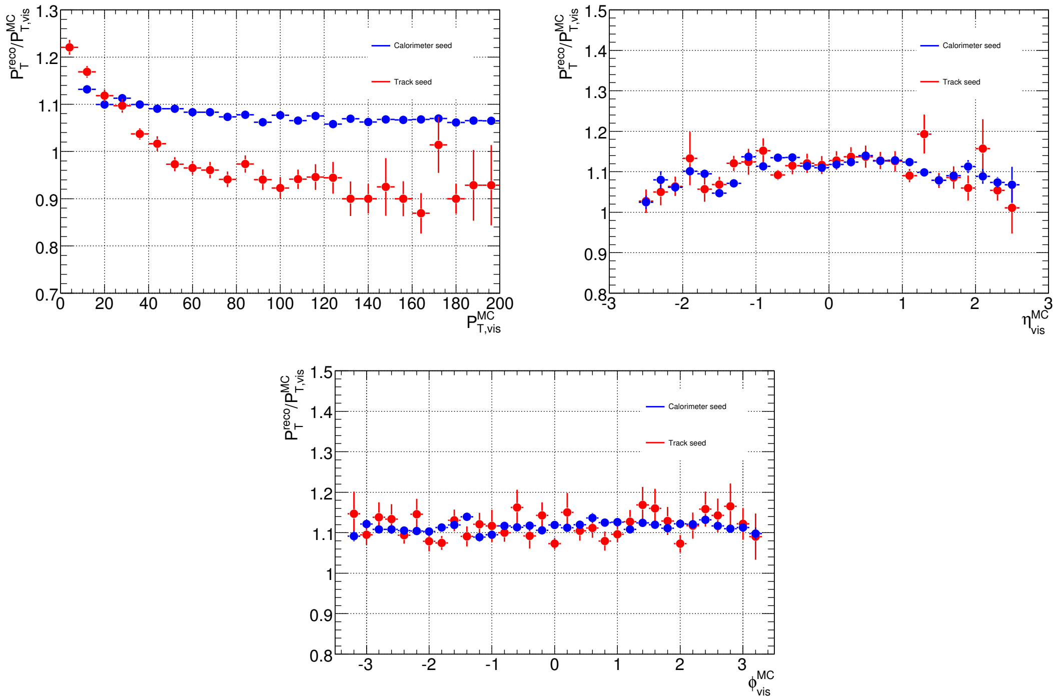

FIGURE 4.3: $p_T^{reco}/p_{T,vis}^{MC}$ as a function of $p_{T,vis}^{MC}$ (top-left), η_{vis}^{MC} (top-right) and ϕ_{vis}^{MC}, (bottom) for true taus reconstructed by `tauRec` in a SUSY coannihilation region sample. The blue line shows the linearity for the calorimeter seeded algorithm, while the red line shows the linearity for the track seeded algorithm.

4.3.3 Direction reconstruction

Figure 4.4 shows the η and ϕ resolutions of both the calorimeter and track seeded algorithms. Since the direction reconstruction of the track seed algorithm takes precedence over that for the calorimeter seed, the calorimeter seeded resolution is for candidates which *only* have a calorimeter seed. Resolutions for soft and hard taus are shown superimposed. We can see that, overall, the direction reconstruction of the track seeded algorithm is better than that of the calorimeter seed, as expected. Furthermore the direction reconstruction of harder taus is better for the track seeded algorithm, likely due to a smaller chance of interaction in the tracking material for more energetic tracks. The direction reconstruction of the calorimeter seeded algorithm is also better for hard taus due to the narrower deposition area of hard taus in the calorimeter. This narrower area arises from narrower showers from more boosted taus and from opposite sign particles diverging less in the detector magnetic field. The effect of opposite sign particle divergence is particularly apparent in the calorimeter seeded ϕ resolution for soft taus, where we can see that the 3-prong taus' track divergence significantly degrades ϕ reconstruction performance.

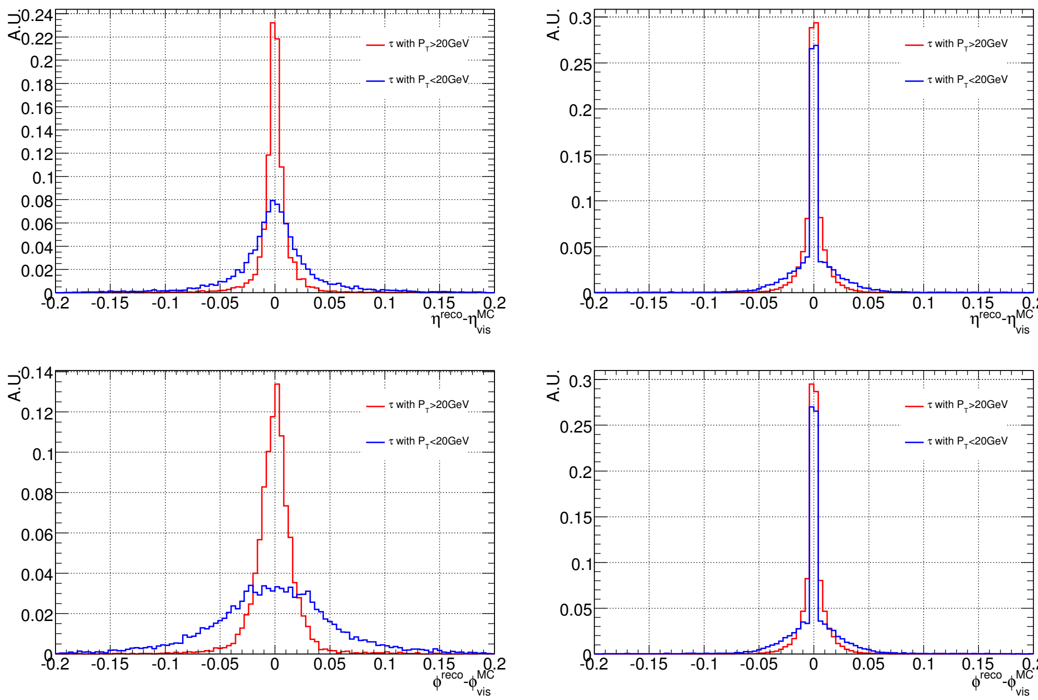

FIGURE 4.4: The direction resolutions of the `tauRec` algorithm, for true taus in a SUSY coannihilation region sample. The plots on the left show resolutions for the calorimeter seeded algorithm while those on the right show resolutions for the track seeded algorithm. The plots on the top show the direction resolution in η while those on the bottom show the resolution in ϕ. Resolutions for taus with $p_{T,vis}^{MC} > 20$GeV (red) and with $p_{T,vis}^{MC} < 20$GeV (blue) are shown superimposed.

4.3.4 Discrimination performance

After the reconstruction step it is then necessary to apply identification cuts to the `tauRec` objects in order to reject background. This is done with a cut on the likelihood variable discussed above. Figure 4.5 compares this likelihood curve for true taus from a coannihilation sample, and for jets from a J2 sample. It shows the curves for hard objects and soft objects superimposed. It is obvious that discrimination is much easier for harder objects than softer objects. As taus become softer their signals become more and more similar to those of soft jets.

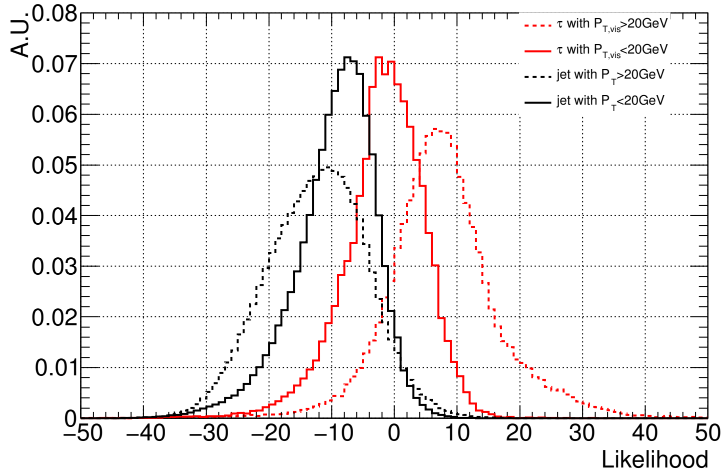

FIGURE 4.5: Comparison of the `tauRec` likelihood for true taus and QCD jets. Plots for soft objects ($p_T < 20$GeV) and hard objects ($p_T > 20$GeV) are shown superimposed.

In addition to a cut on the likelihood, we also apply some other cuts for "identification" in order to reduce background further. These are the electron and muon vetoes, the requirement that the object has exactly one or three associated tracks, and the requirement that $|Q| = 1$ for the object. Furthermore, we only consider objects in the region $|\eta < 2.5|$ which is the kinematic region within which `tauRec` attempts reconstruction. We thus we define tau efficiency in the coannihilation region

$$\epsilon^{signal} = \frac{\text{number matched } \texttt{tauRec} \text{ with 1,3 tracks, } \mu, e \text{ veto, } |Q| == 1, \text{LLH} > \text{LLH}^{cut}}{\text{number of MC taus within } |\eta| < 2.5} \tag{4.13}$$

Similarly the fake rate is defined as

$$\epsilon^{jet} = \frac{\text{number matched } \texttt{tauRec} \text{ with 1,3 tracks, } \mu, e \text{ veto, } |Q| == 1, \text{LLH} > \text{LLH}^{cut}}{\text{number of MC jets within } |\eta| < 2.5} \tag{4.14}$$

The denominator used for ϵ^{jet} is simply the number of MC jets in the kinematic region (with no requirement on number of associated tracks). Figure 4.6 shows the performance of the likelihood variable as curves in the $\epsilon^{jet}, \epsilon^{signal}$ plane. As the likelihood variable cut is loosened the signal efficiency increases but at the same time so does the jet efficiency. Curves are shown for different regions of the p_T spectrum and for one and three prong candidates separately.

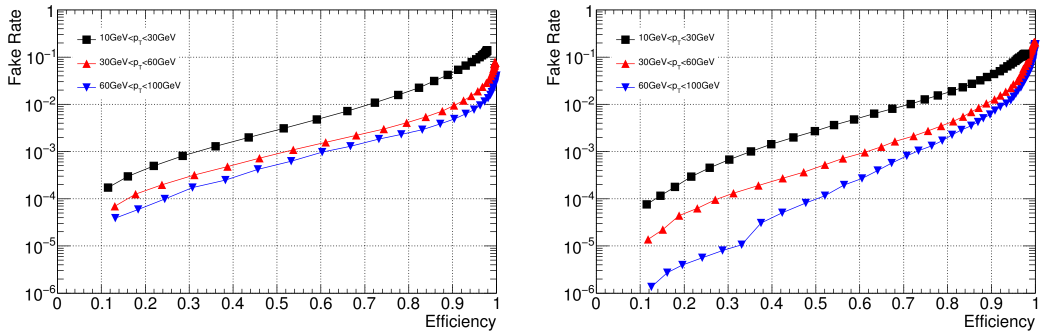

FIGURE 4.6: Fake rate vs. efficiency for `tauRec`. The left hand plot shows the performance for single prong taus while the right hand plots shows the performance for three prong taus. Definitions of fake rate and efficiency are given in the text.

In `tauRec` there are pre-defined cuts in the likelihood variable named "loose" "medium" and "tight" They are designed to roughly correspond to signal efficiencies of 70%, 50% and 30% respectively. Figure 4.7 show the dependency of ϵ^{signal} on $p_{T,vis}^{MC}$, η_{vis}^{MC} and ϕ_{vis}^{MC} for the medium cut. Curves for one and three prong candidates are shown separately. Note that the efficiency plots as functions of η_{vis}^{MC} and ϕ_{vis}^{MC} have an extra requirement on them that $p_{T,vis}^{MC} > 20$GeV. Also shown for reference are curves for the "reconstruction" efficiency. This is simply the efficiency that `tauRec` *reconstructs* the object (before the identification cuts of Equation 4.13).

We can see clearly that that the "reconstruction" efficiency is very low for the low $p_{T,vis}$ region for both one and three prong cases. This is a result of the $E_T > 10$GeV requirement for the calorimeter seeded algorithm, and the $p_T > 6$GeV requirement for the track seeded algorithm. Also, the likelihood cut is rather harsh on the "identification" efficiency all the way up to $p_{T,vis}^{MC}$ 40GeV. This is in order to contain the large QCD statistics in the lower p_T regions.

We now summarise the implications of the performance of `tauRec` in the low energy region for the reconstruction of soft taus.

- In order to reduce jet background it is best to focus only on reconstructing single prong taus.
- Energy reconstruction of low energy taus is very difficult, and it tends to be overestimated
- Using the tracks of the taus results in a better direction reconstruction.
- It is necessary to reduce the seed threshold in order to efficiently reconstruct very soft taus.

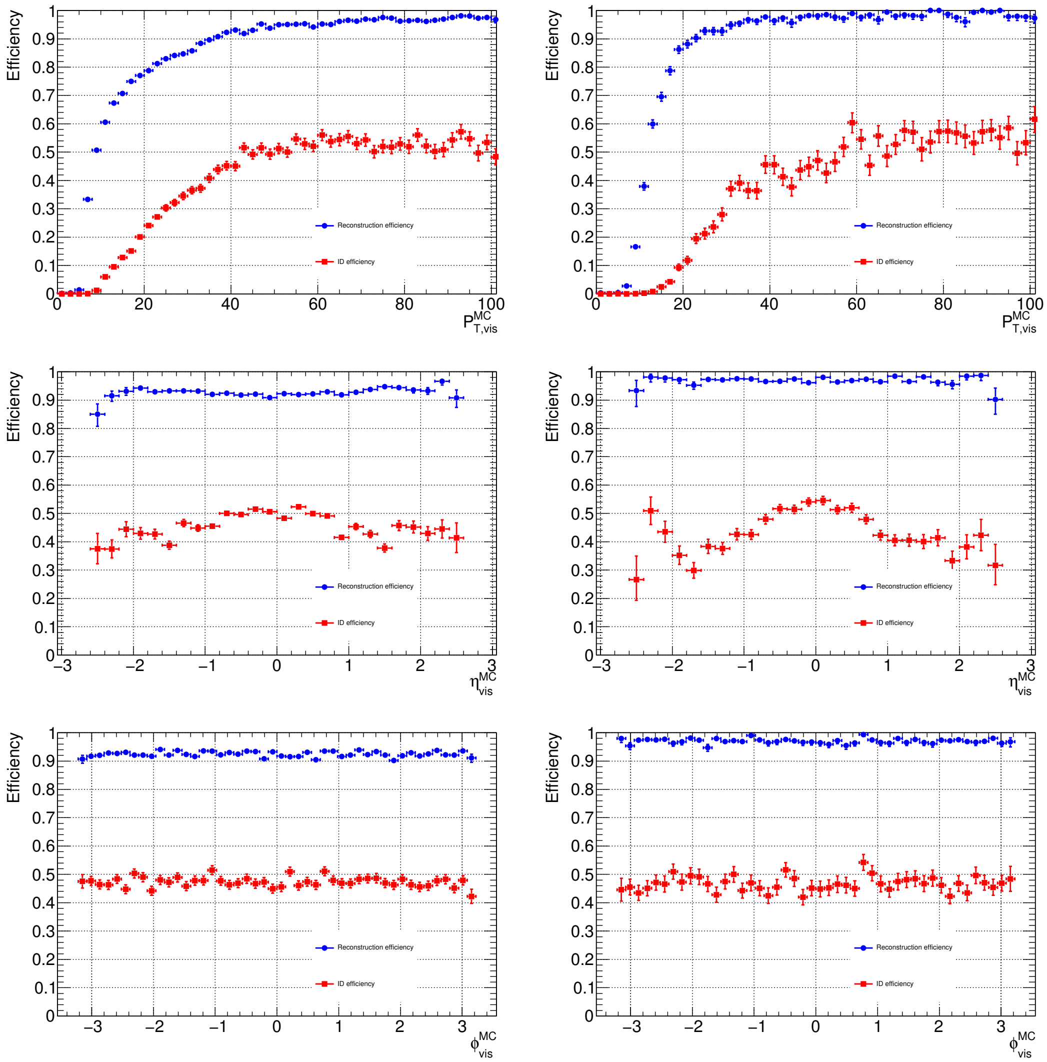

FIGURE 4.7:
Reconstruction and identification efficiencies for the `tauRec` algorithm as functions of $p_{T,vis}^{MC}$ (top), η_{vis}^{MC} (middle), and ϕ_{vis}^{MC} (bottom). The left hand plots show the efficiencies for single prong taus while the right hand plots show the efficiencies for three prong taus. The curves for reconstruction efficiency and identification efficiency are superimposed. The cut used for identification is the "medium" likelihood cut. Note that the plots of efficiency as functions of η_{vis}^{MC} and ϕ_{vis}^{MC} have a requirement that $p_{T,vis}^{MC} > 20\text{GeV}$.

Chapter 5

Soft Tau Reconstruction

In chapter 3 the importance of efficiently reconstructing taus with $p_{T,vis} < 10\text{GeV}$ for the reconstruction of the $M_{\tau,\tau}$ edge was shown. In the previous chapter, the performance of `tauRec` in the low p_T region was shown to be poor, and thus its capability for reconstructing the $M_{\tau,\tau}$ edge can be inferred to be also poor. This chapter describes the development of an entirely new method for tagging the coannihilation region golden decay soft tau in the ATLAS detector. It should be emphasised that there are techniques employed in this method which are analysis specific, so that rather than being a general soft tau reconstruction algorithm, it is an algorithm for tagging a soft tau when it is in the vicinity of some other easier-to-reconstruct object. This was deemed a necessary requirement in light of the fact that there is such an overwhelming background arising from low p_T QCD jets.

The section begins with studies of reconstruction of the signal soft tau $\pi^{\pm}$ tracks and π^0 clusters. The development of a likelihood method for discrimination is then described followed by studies of its performance compared to `tauRec`.

5.1 The soft tau tagging and reconstruction algorithm

A number of methods were used in order to contain the large jet background to the low p_T tau search. They can be summarised as follows:

- Confine the search to single prong taus
- Contain the search to events with well reconstructed hard `tauRec` and also confine the search to the geometrical vicinity of this object.
- Use a likelihood method to discriminate the soft tau

As was described in Section 4.3.1 the background to the $M_{\tau,\tau}$ spectrum can be significantly reduced in the low p_T region if we focus only on tagging the single prong modes of the soft tau *i.e.* if we search for *isolated* tracks. Although this requirement effectively cuts out 21% of the hadronic mode tau signal, it is deemed judicious in order to reduce the overwhelming QCD background in the low p_T region.

As was described in Section 3.2.2 (refer Figure 3.4) the signal soft tau is often fairly close to the signal hard tau due to the underlying boost provided by their mutual parent $\tilde{\chi}_2^0$. Thus we can reduce the background by confining the search for the signal soft tau to the vicinity of a well reconstructed `tauRec` object. Furthermore a final discrimination against jets can be made with a likelihood method along the lines of the `tauRec` likelihood method, but optimised for the low p_T region. Thus the algorithm can be succinctly summarised as **"a search for a low p_T, isolated, tau-like track in the vicinity of a hard `tauRec` object".** Figure 5.1 illustrates this approach.

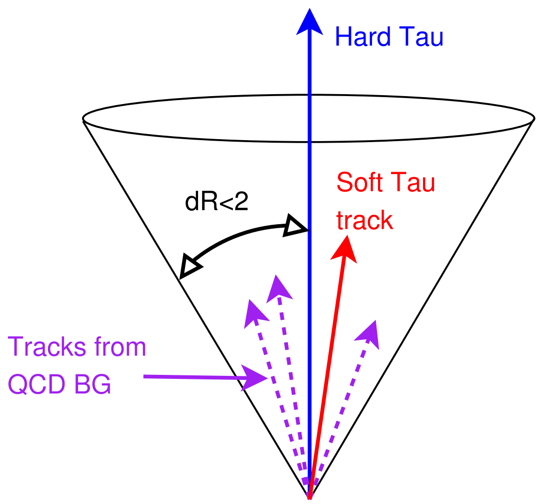

FIGURE 5.1: The single prong soft tau $\pi^{\pm}$ track is searched for within a cone of $\Delta R < 2$ around the candidate hard tau.

In concrete terms the algorithm proceeds as follows:

- Select signal hard tau candidates with $p_{T,vis} > 15$GeV using `tauRec` (cuts for this selection will be outlined in Section 6.1).
- Select soft tau candidates by collecting tracks within a cone of $\Delta R < 2$ of the hard tau candidate and apply to these certain quality and isolation requirements.
- Search for π^0 candidate clusters around the soft tau candidate track.
- Use the π^0 candidate clusters and other information to create a likelihood variable for determining the tau-likeness of the soft tau candidates. Dispose of the candidates which are not sufficiently tau-like.

- Of the soft tau candidates which remain select the most tau-like of the candidates.

This approach differs from the traditional approaches of reconstructing the $M_{\tau,\tau}$ end-point which tend to focus on selecting events with two well reconstructed taus.[21] [11] [25] [26] Instead the focus here is on "searching out" the softer tau around the hard tau. The problem with the requirement of two well reconstructed taus is that the signal soft taus are so soft and thus so difficult to identify that traditional tau reconstruction algorithms will often miss them, either through stringent cuts on seed energy, or through stringent cuts on identification cuts. Here, rather, the approach is to select hard taus in SUSY like events, and then select tracks around it which are "sufficiently" tau-like. If there is more than one soft tau candidate then the most tau-like one is chosen.

The following two subsections describe studies of the reconstruction and identification of the signal soft tau single prong mode $\pi^{\pm}$ tracks and π^0 clusters.

5.1.1 The soft tau $\pi^{\pm}$ reconstruction and selection

The quality of the information coming from the tracking measurements in the inner detector is of superior quality relative to that coming from the calorimeters for isolated charged objects in the low p_T region. Thus the decision was made to use tracks around the reconstructed hard taus as seeds for the soft tau tagging algorithm. This motivation is similar to that for the development of the track seeded algorithm in `tauRec`, which is designed for tau reconstruction in the lower p_T region, albeit with a limit of $p_{T,vis} \gtrsim$ 10GeV .

We saw in the study of `tauRec` that reconstruction of the tau energy is rather difficult and so for this study only the single prong *track* energy is used for the final $M_{\tau,\tau}$ distribution. π^0 information is used only for tau discrimination. This point is further discussed in Section 7.5.2. We also saw that reconstructing the tau direction from track information results in a better quality direction reconstruction. Using the seed track for the soft tau direction reconstruction will guarantee a good direction reconstruction.

5.1.1.1 Truth level study

Figure 5.2 shows the truth level distributions of the $\pi^{\pm}$ for the three single prong modes of the signal soft tau. p_T, η and ϕ are shown, with distribution for the 0-π^0, 1-π^0 and 2-π^0 modes superimposed. We can see that, as expected, the lower π^0 multiplicity modes' $\pi^{\pm}$ have higher p_T than the higher multiplicity modes since they get a larger share of the tau energy. The mean values of the p_T for the 0,1 and 2-π^0 mode $\pi^{\pm}$ tracks are 9.2 GeV, 4.6 GeV and 3.9 GeV respectively.

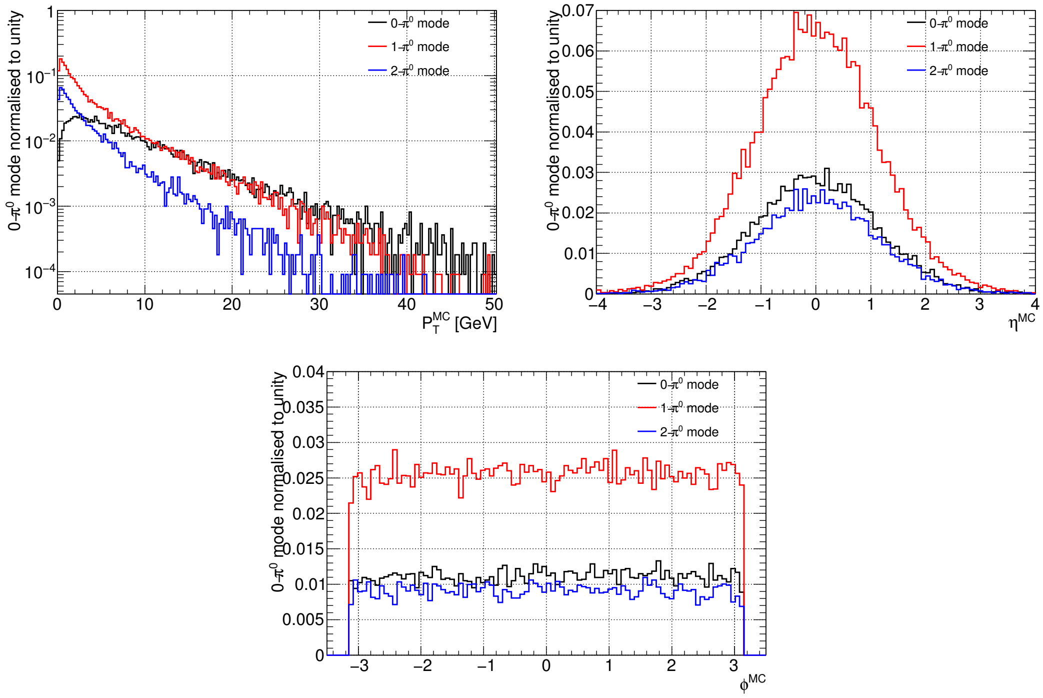

FIGURE 5.2: The truth level kinematic distributions for the $\pi^\pm$ of the hadronic single prong signal soft tau of the coannihilation region. The top left plots show p_T, the top right η, and the bottom ϕ. Separate plots for the 3 single prong modes are shown superimposed. The $0-\pi^0$ distributions are normalized to unity.

5.1.1.2 Reconstruction

Figure 5.3 shows the distance between the truth level $\pi^\pm$ and the closest reconstructed track, where all single prong modes have been combined. $p_T > 2$GeV and $|\eta| < 2.5$ (the extent of the inner tracker) cuts are imposed at the truth level. Unless otherwise specified, from here, all plots involving the $\pi^\pm$ tracks will have these cuts imposed. In light of the $\Delta R_{MC,reco}$ distribution we set the track matching condition to $\Delta R_{MC,reco} < 0.01$ and use this condition for the definition of "$\pi^\pm$ is reconstructed". With this definition the misidentification of the reconstructed $\pi^\pm$ tracks is only 0.04%.

Figure 5.4 shows the p_T, η, and ϕ resolutions for the reconstructed track of the matched $\pi^\pm$s. The gaussian fit of the p_T resolution yields a width of $\sigma = 1.69\%$.

Figure 5.5 shows the reconstruction efficiency of the signal soft tau single prong $\pi^\pm$ tracks, as a function of p_T and η, where the $\Delta R_{MC,reco} < 0.01$ condition is used. The efficiencies for the 3 single prong modes are combined in these plots. The $p_T > 2$GeV cut is not imposed on the efficiency vs. p_T plot, so as to illustrate the efficiency dependence in the low p_T region. We can see that the reconstruction efficiency levels off to around 90% for $p_T \gtrsim 2$GeV and falls dramatically for $p_T \lesssim 700$MeV which is around the expected

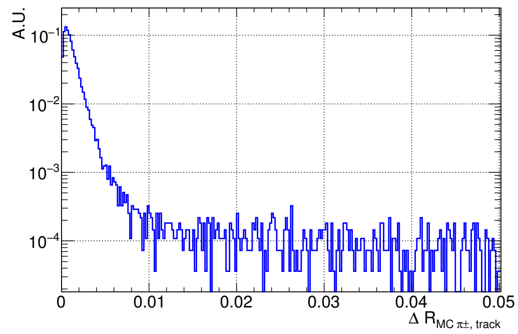

FIGURE 5.3: The distance between the truth level $\pi^{\pm}$ from the hadronic single prong signal soft tau, and the closest reconstructed track. A $p_T > 2$GeV and $|\eta| < 2.5$ cut is imposed at the truth level. From now we use $\Delta R_{MC\,\pi^{\pm},track} < 0.01$ as the matching condition for the signal $\pi^{\pm}$.

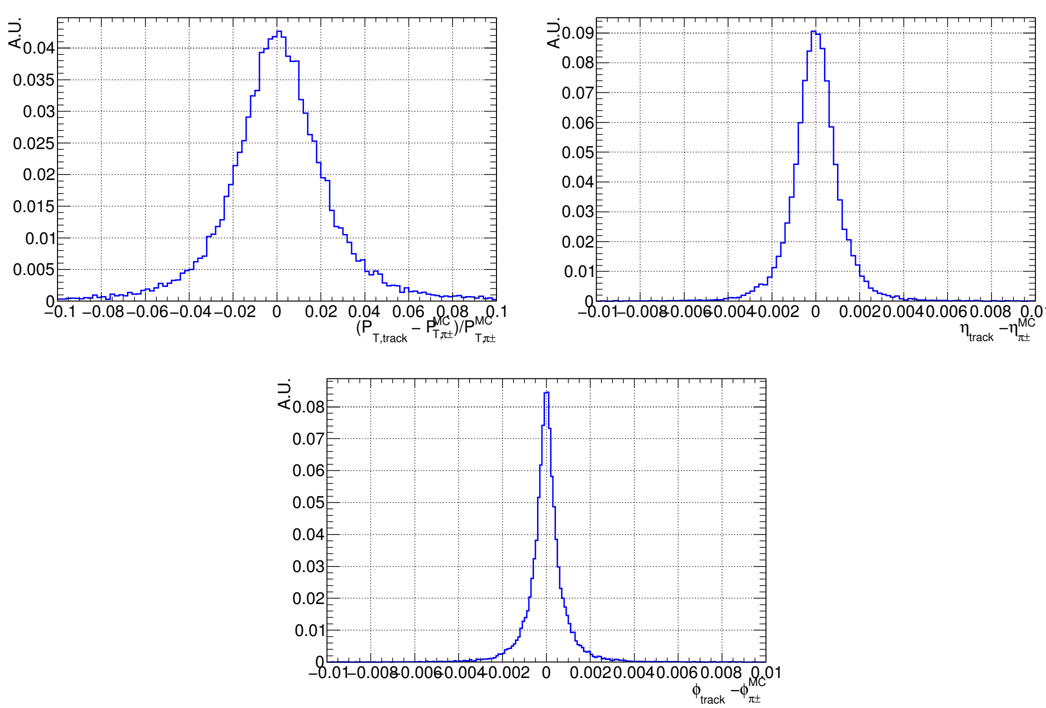

FIGURE 5.4: p_T, η, and ϕ resolutions for the $\pi^{\pm}$ from the hadronic single prong modes of the signal soft tau of the coannihilation region.

lower limit for the performance of the tracking detectors [21]. Inefficiencies of tracking of $\pi^{\pm}$ at low p_T arise because of the large material effects in this region. We can also see that the efficiency falls of with increasing $|\eta|$ which is again a result of increased probability for interactions as the amount of material traversed by the $\pi^{\pm}$ increases. A small dip at $\eta \approx 0$ can be seen where there is an increase in the traversed material in the SCT and TRT detectors.

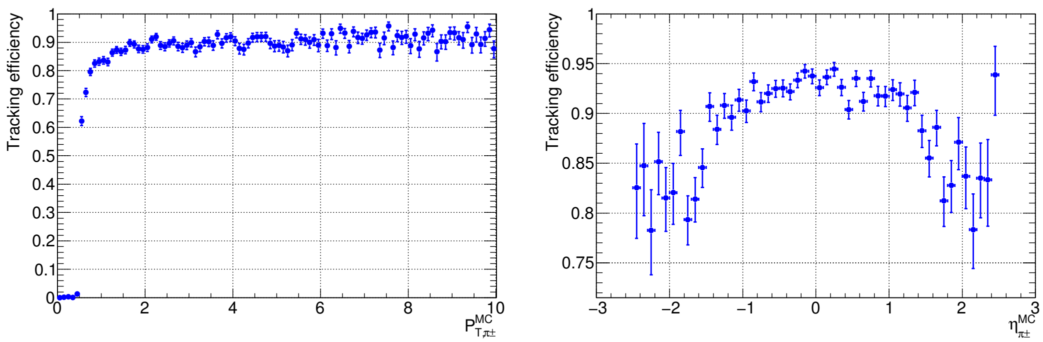

FIGURE 5.5: Track reconstruction efficiencies of the hadronic single prong signal soft tau $\pi^{\pm}$ as functions of p_T and η. The $p_T > 2$GeV cut is not imposed on the truth level for the efficiency vs. p_T plot.

5.1.1.3 Selection

Now in order to seed the soft tau tagging algorithm the quality cuts of the tracks needed to be decided. The quantities used for the track seeded algorithm of `tauRec` were checked and ultimately it was decided that the same quality requirements would be used for this algorithm. The only exception was the reduction of the p_T cut from 6 GeV to 2 GeV. As discussed in Section 4.3.4, it is necessary to reduce the seed threshold in order to increase the soft tau reconstruction efficiency. The 2 GeV cut is a preliminary cut for choosing the soft tau candidates and studies for optimising it for the $M_{\tau,\tau}$ analysis will be outlined in Section 6.3. Figure 5.6 shows the distributions of the track quality quantities for the single prong signal soft tau $\pi^{\pm}$ tracks, and for the background to these tracks which are the other reconstructed tracks in the region $\Delta R < 2$ of the reconstructed hard tau. These comprise both real tracks (mainly from jets) and fake tracks. The $p_T > 2$GeV cut, and a standard χ^2/d.o.f < 1.7 cut is applied to both signal and background tracks for these plots. The track quality cuts for the soft tau tagging algorithm seed are shown in the second column of Table 5.1.

Since it was decided that only single prong modes would be considered fairly stringent isolation requirements can be made on the algorithm seed track. Seed tracks are considered as isolated if no tracks of a given quality are reconstructed within $\Delta R < 0.2$ of

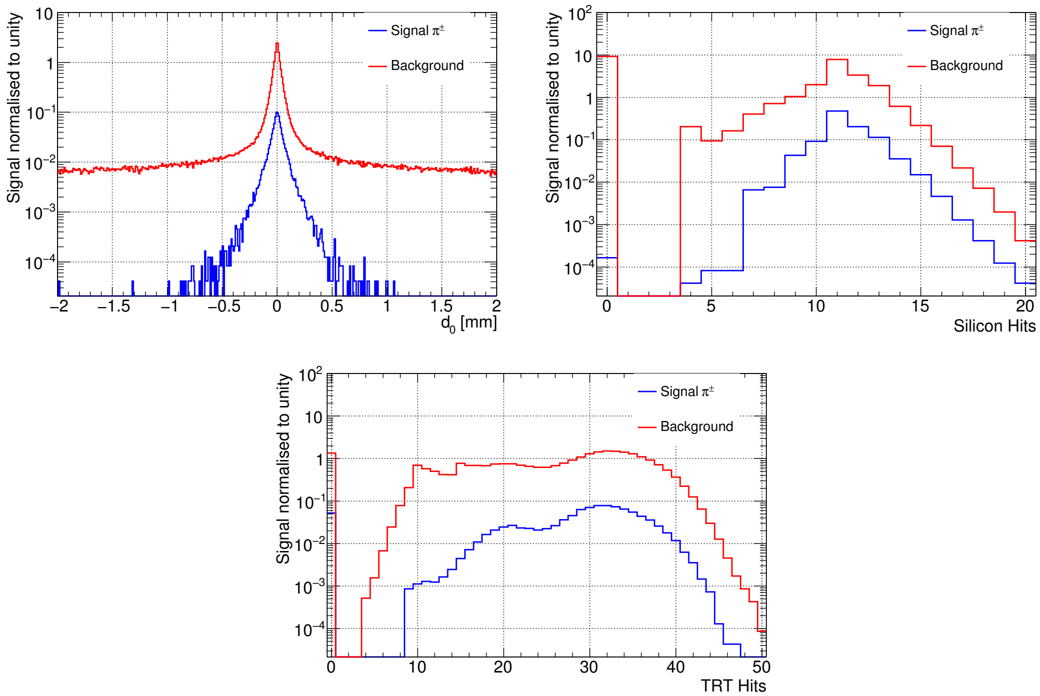

FIGURE 5.6: The track quality quantities for the signal $\pi^{\pm}$, and the background tracks within the search area around the signal hard tau. The signal distributions are normalised to unity. The soft tau search algorithm seed track cuts are $|d_0| < 1$mm, number of silicon hits ≥ 8, and TRT hits ≥ 10 (when $|\eta_{track}| < 1.9$).

Track criteria	Seed track	Isolation track
p_T [GeV]	2	1
$\|\eta\| <$	2.5	2.5
Impact parameter d_0[mm] $<$	1	1
Silicon Hits $N_{si} \geq$	8	8
TRT hits $N_{TRT} \geq$ (when $\|\eta\| < 1.9$)	10	no cut
χ^2/d.o.f $<$	1.7	1.7
Pixel Hits $N_{pixel} \geq$	no cut	1
B-layer hits $N_{blay} \geq$	no cut	1
High/Low threshold hit ratio $N_{TRT}^{HT}/N_{TRT}^{LT} <$	no cut	0.2

TABLE 5.1: Track quality criteria for the soft tau tagging algorithm seed track and isolation track.

it. The quality requirements for the “isolation tracks” are shown in the third column of Table 5.1. The same requirements as those for the “associated tracks” of the `tauRec` track seeded algorithm were used. These have been optimised to be stringent enough to exclude tracks arising from conversion electrons coming from $\pi^0 \to \gamma, \gamma$ decay, and so are ideal for checking the isolation of the $\pi^\pm$ coming from taus with π^0 decay products.

The left hand plot of Figure 5.7 shows the distribution for the distance from the seed track to the closest “isolation track”. The distribution for the signal $\pi^\pm$ tracks and for the background to these tracks are shown superimposed, where again the background are the seed tracks in the region $\Delta R < 2$ of the reconstructed hard tau which do not come from the signal soft tau. We can see that a track isolation cut of $\Delta R < 0.2$ removes a lot of the background which mainly comes from jet activity. The right hand plot of Figure 5.7 shows the p_T distributions of the signal and background. For this plot the track cut has been reduced to $p_T > 1$GeV in order to illustrate the rise in the background below the 2GeV cut. As mentioned before, a tentative cut of $p_T > 2$GeV was made on the seed track but this will be optimised in the full background analysis of Section 6.3.

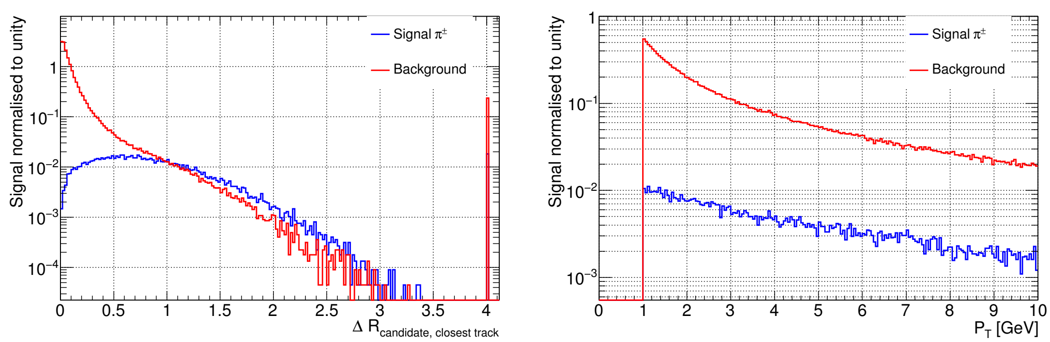

FIGURE 5.7: The left hand plot shows the distance between the seed quality track, and the closest “isolation quality” track, for both signal and background seed tracks. The right hand plot compares the p_T of the signal and background seed quality tracks.

5.1.1.4 Performance

Table 5.2 shows the cut flow for the 3 single prong modes when the seed track quality cuts are made. It also shows how the mean number of background tracks within the soft tau search area changes with the cuts. We can see that around quarter of the signal is lost by confining the search area to $\Delta R < 2$ around the signal hard tau. We can also see that the $p_T > 2$GeV cut biases the remaining soft tau signal towards the lower π^0 multiplicity modes, since the higher π^0 multiplicity modes have softer $\pi^\pm$ tracks. After all of the seed track requirements an average of 1.3 tracks besides the signal $\pi^\pm$ track

	0-π^0 mode [/fb^{-1}]	1-π^0 mode [/fb^{-1}]	2-π^0 mode [/fb^{-1}]	mean no. BG in search area
No cut	8.2	18.9	6.7	
$\|\eta\| < 2.5$	7.9	18.3	6.5	
Reconstructed	7.1	14.1	5.0	
Within $\Delta R < 2$ of hard tau	5.1	10.4	3.7	30.1
$\|d_0\| <$ 1mm	5.1	10.3	3.7	16.5
Si hits≥ 8	5.0	10.3	3.6	15.1
TRT hits≥ 10	4.6	9.4	3.3	13.5
$\chi^2 < 1.7$	4.4	8.9	3.1	12.0
$p_T >$ 2GeV	4.1	6.3	2.1	7.9
Isolated	3.8	5.9	2.0	1.3

TABLE 5.2: Cut flow for coannihilation single prong signal soft tau $\pi^{\pm}$ with the soft tau search algorithm seed track selection cuts. Cut flows for each of the 3 considered decay modes are shown separately. The fifth column shows the mean number of background tracks which remain in the soft tau search area as the cuts are made on the seed tracks.

remain in the search area around the signal hard tau. Thus, on average, the likelihood method will need to select the signal soft tau $\pi^{\pm}$ track from out of 2.3 tracks.

5.1.2 The soft tau π^0 reconstruction and selection

The fact the signal soft taus are not very boosted means that any π^0 coming from their decay can be relatively separated from the $\pi^{\pm}$ in the calorimeter. It is possible to exploit this fact to help to discriminate these taus from background. The following section outlines the algorithm developed for selecting any π^0 clusters coming from the soft tau decay.

5.1.2.1 Truth level study

Figure 5.8 shows the truth level energy distributions of the π^0 coming from the 1-π^0 and 2-π^0 modes for the signal soft tau. We can can see that, as expected, the 2-π^0 mode π^0 are less energetic than the 1-π^0 mode π^0 due to the tau energy being shared amongst more decay products. The mean energy of the π^0 from the 1-π^0 mode decay is 7.33GeV while the mean energies of the π^0s coming from the 2-π^0 mode decay are 6.94GeV and 3.01GeV. Particularly for the 2-π^0 mode, the reconstruction of such low energy clusters in the calorimeter is extremely challenging due to material in front of the calorimeter.

Figure 5.9 shows the truth level correlation of the distance between the $\pi^{\pm}$ and the π^0(s) at the interaction point, $\Delta R_{\pi\pm,\pi 0}$, and the p_T of the $\pi^{\pm}$, $p_{T,\pi^{\pm}}$, for both 1 and 2-π^0 modes. If the tau is less boosted then the p_T of the $\pi^{\pm}$ will be lower. As can be

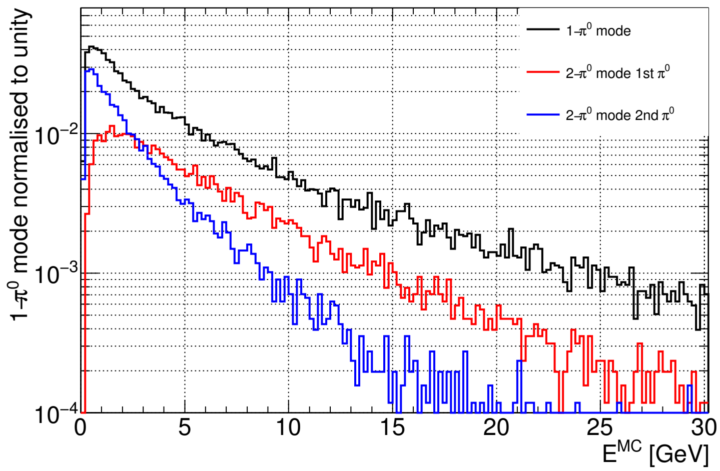

FIGURE 5.8: Truth level energy distributions for the π^0 coming from the 1-π^0 and 2-π^0 signal soft tau single prong mode decays.

seen, as the p_T of the $\pi^\pm$ becomes smaller, the distance between the $\pi^\pm$ and the π^0 grows larger due to this smaller boost. Thus we can see that we can size the search area for π^0 clusters around the vertex direction of the $\pi^\pm$ track according to $p_{T,\pi\pm}$. The $p_{T,\pi\pm}$ dependant search area that is used for the π^0 selection algorithm is shown superimposed on the figure. It is a cone of 0.4 for 2GeV $< p_{T,\pi\pm} <$ 5GeV, 0.2 for 5GeV $< p_{T,\pi\pm} <$ 10GeV, and 0.1 for 20GeV $> p_{T,\pi\pm}$. This is an improvement on the `tauRec` track seeded algorithm method of searching for π^0 clusters which employs only a fixed cone size ($\Delta R < 0.2$).

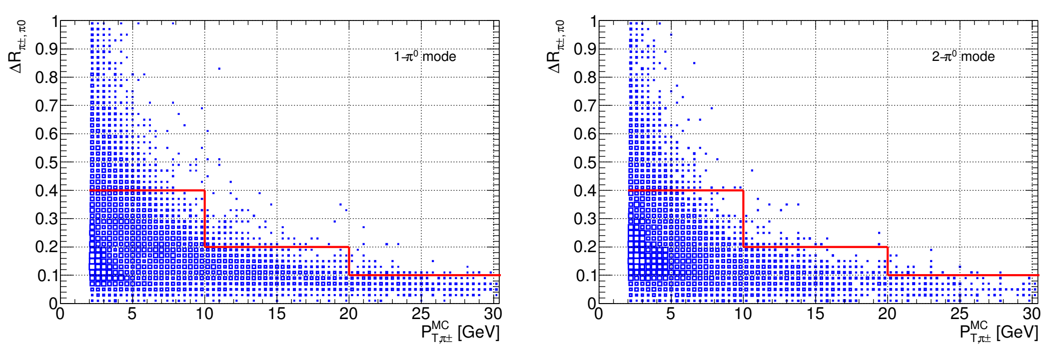

FIGURE 5.9: The truth level correlation between $\Delta R_{\pi\pm,\pi0}$ and $p_{T,\pi\pm}$ for the signal soft tau 1 and 2-π^0 modes. The correlation for the 1-π^0 is shown on the left, while the correlation for the 2-π^0 mode is shown on the right. For the 2-π^0 mode the histograms for each π^0 are added together.

5.1.2.2 Excluding the $\pi^{\pm}$ cluster

The basic procedure for the π^0 cluster search algorithm is as follows.

- The seed track is propagated to the middle layer of the calorimeter and the primary cluster of the track is searched for. This cluster is excluded from the search for the π^0 clusters.
- Clusters are then searched for in a search cone around the vertex direction of the seed track. The size of this search cone is $p_{T,\pi^{\pm}}$ dependant as described above.
- Only clusters which pass certain EM-like criteria are accepted as π^0 candidate clusters.

For the purpose of excluding the $\pi^{\pm}$ cluster from the search, and for attempting to resolve up to two π^0 clusters (from the single prong 2-π^0 mode), the topological clustering algorithm of Section 4.2.2 was used. This clustering algorithm performs better than a fixed cone algorithm for resolving clusters which are close together in the calorimeter.

In order to exclude the $\pi^{\pm}$ cluster from the π^0 search we find the closest cluster to the $\pi^{\pm}$ position in the middle layer of the calorimeter. The matched cluster is required to have $E > 1$GeV when it is calibrated to the hadronic scale [1] . Figure 5.10 shows the distribution of the distance between the track position in the middle calorimeter and the matched cluster, $\Delta R_{track,cluster}$, for the signal $\pi^{\pm}$. For this section of the study, only the 0-π^0 mode is used to avoid contamination from any π^0. Also, only soft taus which are $\Delta R > 0.8$ from the signal hard tau are used to avoid contamination from the signal hard tau. It is obvious that at such low energy the match between the $\pi^{\pm}$ track and cluster is not always good ($\Delta R_{track,cluster}$ can be rather large). This is because of significant multiple scattering before the calorimeter.

At low energy the shower arising from the $\pi^{\pm}$ is also wider and may result in a number of secondary clusters in the calorimeter. We can observe this affect by looking at $E_{T,cluster}/p_{T,track}$ for the matched cluster. This is shown in the left hand plot of Figure 5.11. Note that these clusters are corrected for energy loss before the calorimeter. Obviously not all of the $\pi^{\pm}$ energy is contained in this cluster. The right hand plot of the same figure shows E_T/p_T again, but now with the sum of the E_T of all of the clusters in a cone of 0.2 around the $\pi^{\pm}$. We can see that the energy is mostly fully recovered. Figure 5.12 shows the number of clusters which are collected in this cone. We can see that for most of these low energy $\pi^{\pm}$ the energy in the calorimeter is dispersed amongst greater than one clusters.

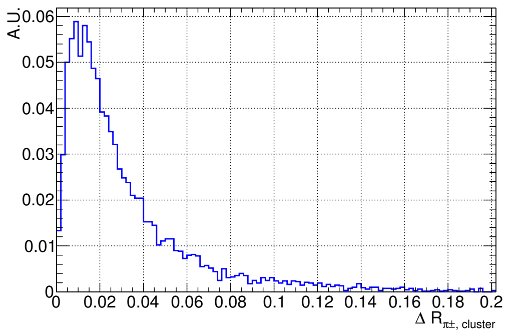

FIGURE 5.10: The distance between the signal $\pi^{\pm}$ in the middle layer of the calorimeter, and the closest cluster. For this plot only the $\pi^{\pm}$ from the 0-π^0 mode is shown in order to avoid contamination from π^0.

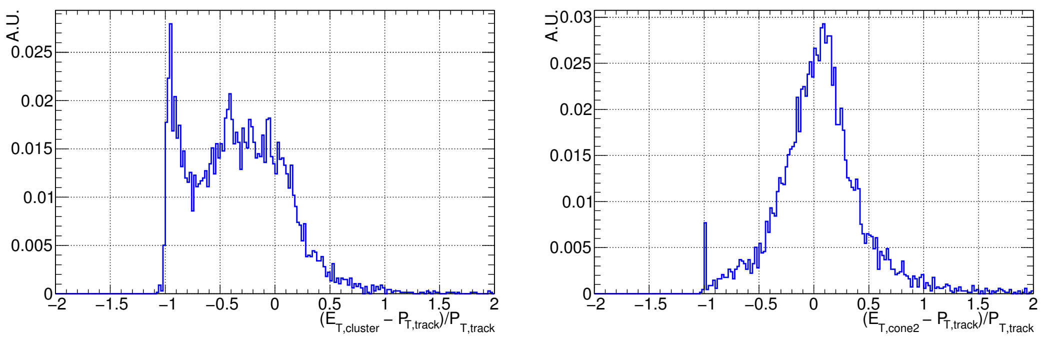

FIGURE 5.11: The left hand plot shows $E_{T,cluster}/p_{T,track}$ where the track is the signal $\pi^{\pm}$ track, and the cluster is the closest matched cluster in the calorimeter. The right hand plot shows E_T/p_T again, but this time with the E_T of all of the clusters within 0.2 of the $\pi^{\pm}$ track summed.

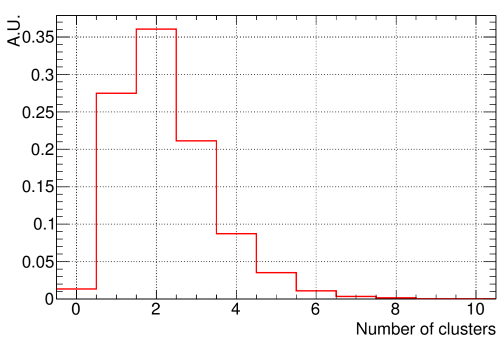

FIGURE 5.12: The number of clusters collected in a cone of 0.2 around the signal $\pi^{\pm}$ impact in the calorimeter. For this plot only the 0-π^0 mode is shown in order to avoid contamination from any π^0.

Now the best that we can do to remove the primary $\pi^{\pm}$ cluster from π^0 candidacy is to remove it only if is close to the impact of the $\pi^{\pm}$ in the calorimeter. Otherwise there is a risk of removing π^0 clusters as well. Thus we only remove the $\pi^{\pm}$ matched cluster if it is within $\Delta R < 0.04$ of the $\pi^{\pm}$ track at the middle layer of the calorimeter. For the case that the match is not good, π^0 clusters will be discriminated using only cuts on energy and shower shape, as will be described below. Note that this π^0 discrimination will potentially be against a number of low energy secondary $\pi^{\pm}$ clusters, and thus will be quite challenging.

5.1.2.3 Selecting π^0 clusters with `EMFracClusterClassificationTool`

The next step is to select EM-like π^0 candidates from the remaining clusters. This "EM-likeness" is determined with a package within Athena named `EMFracClusterClassificationTool`. The algorithm in this package is the default algorithm used for classifying topological clusters in Athena as EM or hadronic. Its algorithm works by classifying a cluster as EM or hadronic by comparing it with the phase space population predicted by single $\pi^{\pm}$ and single π^0 Monte Carlo simulations in Athena.[19] A 4-dimensional phase space in $|\eta|, E_{cluster}, \log_{10}\lambda_{centre}$ and $\log_{10}\langle\rho\rangle$ is used, where λ_{center} is the distance of the shower centre from the front face of the calorimeter along the shower axis, and $\langle\rho\rangle$ is the first moment in energy density

$$\langle\rho\rangle = \frac{1}{E_{norm}} \times \sum_{i|E_i>0} E_i\,\rho_i\,,\ E_{norm} = \sum_{i|E_i>0} E_i \tag{5.1}$$

For the above formula, E_i and ρ_i are the energy and energy density of the ith cell respectively. The sum is over the cells in the cluster. This phase space is populated with equal numbers of $\pi^{\pm}$ and π^0, with an energy range of 200MeV - 2TeV. Assuming a probability ratio of $\pi^{\pm}$ to π^0 production of 2:1, a weight is then calculated for each bin i in the phase space

$$EMfraction = \frac{n_i^{\pi^0}}{n_i^{\pi 0} + 2n_i^{\pi\pm}} \tag{5.2}$$

where $n_i^{\pi^0}$ is the fraction of π^0 in the bin and $n_i^{\pi^{\pm}}$ is the fraction of $\pi^{\pm}$. By default if a candidate cluster falls in to a bin which has $EMfraction > 0.5$, then the cluster is classified as EM, though this setting can be altered if desired.

[1]Calibration for clusters matched to seed tracks for this algorithm is done using Local Hadronic Calibration, as described in Section 4.2.2.

Figure 5.13 shows the probability that a cluster comes from a π^0 as a function of $\langle\rho\rangle$ of the cluster, and λ_{center} of the cluster, when the above mentioned Monte Carlo procedure is followed. η and $E_{cluster}$ are fixed for these plots. The hot areas of the plots are the bins which are highly populated with π^0, while the cold areas are the bins which are highly populated with $\pi^{\pm}$. Green areas are those regions of the phase space where there is a lot of overlap between $\pi^{\pm}$ and π^0. The left hand plot is for 1GeV< $E_{cluster}$ <2GeV clusters, while the right hand plot is for 8GeV< $E_{cluster}$ <16GeV clusters. We can see that π^0 clusters tend to populate areas of lower λ_{center}, and higher $\langle\rho\rangle$ as we would expect for EM clusters. We can also see that there are a lot more areas of green for the low energy plot. This means that the phase spaces of $\pi^{\pm}$ and π^0 overlap. This is because the showers of $\pi^{\pm}$ and π^0 look more and more similar as their energies becomes smaller. This makes it more difficult to distinguish the two at low energy.

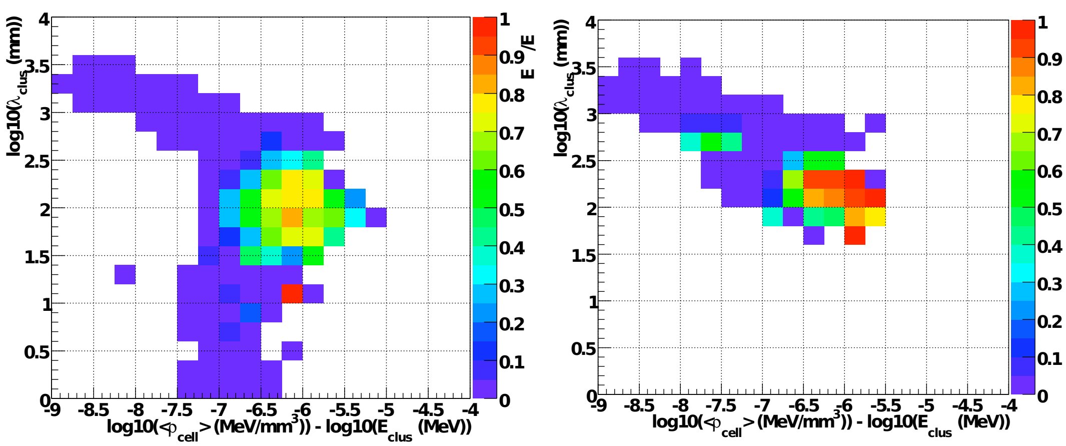

FIGURE 5.13: Probability that a cluster comes from a π^0 as a function of $\langle\rho\rangle$ of the cluster and λ_{center} of the cluster. Both plots are for the region $0.2 < |\eta| < 0.4$, but the left hand plot is for clusters with 1GeV< $E_{cluster}$ <2GeV, while the right hand plot is for clusters with 8GeV< $E_{cluster}$ <16GeV. [19]

While the classification efficiency with the default boundary of EMfraction=0.5 for π^0 clusters with $E > 50$GeV is rather good at 80 - 85%, this efficiency falls off to 50% at 5GeV and 23% at 1GeV. This is due to the substantial overlap in the phase space of $\pi^{\pm}$ and π^0 at low energy, *i.e.* low energy $\pi^{\pm}$ clusters look very similar to low energy π^0 clusters.

In order to optimise the classification efficiency of our signal π^0 clusters, and thus to optimise the decay mode classification efficiency of our signal tau, this $EMfraction$ setting was changed.

The EMfraction setting was optimised using the following procedure. Monte Carlo π^0s from the 1-π^0 mode signal tau were matched to topoclusters. Only events with

$E_{\pi 0} > 1\text{GeV}$ and where the π^0 were within the π^0 search cone around the $\pi^{\pm}$ were considered. The cluster was considered matched if it was not the same as the $\pi^{\pm}$ cluster (*i.e.* the π^0 did not overlap with the $\pi^{\pm}$ in the calorimeter), and the distance between the truth level π^0 and the cluster was less than 0.1. These π^0 were considered as "findable". Then the $EMfraction$ setting was varied to try to find the setting at which this π^0 cluster was the only EM-like cluster within the π^0 search cone.

Figure 5.14 shows the efficiency of EM-like classification as the $EMfraction$ setting is varied, both for the π^0 cluster, and for reference, the $\pi^{\pm}$ cluster, of the 1-π^0 mode. We see that as the $EMfraction$ setting is increased the efficiencies drop off, as expected.

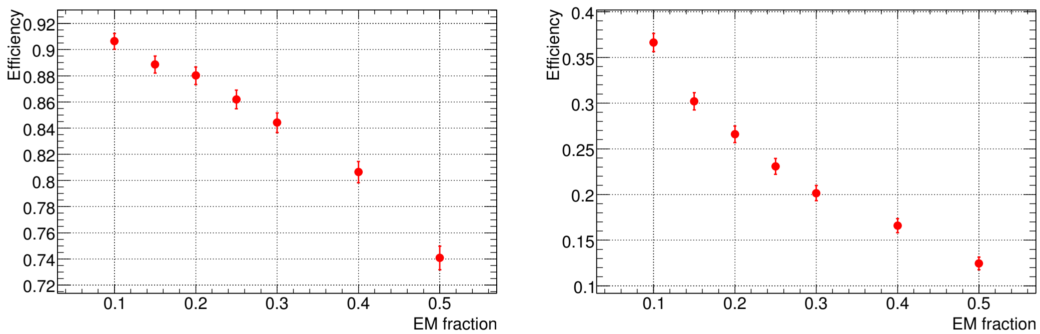

FIGURE 5.14: The change in the EM-like classification efficiency of the signal 1-π^0 mode π^0 cluster (left), and $\pi^{\pm}$ cluster (right), as $EMfraction$ is varied.

The left hand plot of Figure 5.15 shows, for the 1-π^0 mode, the number of clusters in the π^0 search cone which are classified as EM-like, after the primary $\pi^{\pm}$ cluster was removed, as discussed above. The plots from varying the $EMfraction$ setting from 0.1 - 0.5 are shown superimposed. Mostly only the π^0 cluster is classified as EM-like, thus the peak at 1. We can see though that, as the $EMfraction$ setting is decreased, the number of clusters classified as EM-like increases. This is because many of the secondary $\pi^{\pm}$ clusters are also classified as EM-like. Events with greater than one EM-like cluster can also arise from the two π^0 gamma rays actually forming two separate clusters.

Finally the right hand plot of Figure 5.15 shows the fraction of the selected events for which the π^0 cluster is the only EM-like cluster found, as $EMfraction$ is varied. The maximum is for a setting of 0.2. That is to say that, with the above π^0 search algorithm, the maximum number of 1-π^0 events will be correctly classified when $EMfraction$ is set to 0.2. We thus use this setting for selecting π^0 clusters from around the $\pi^{\pm}$ track.

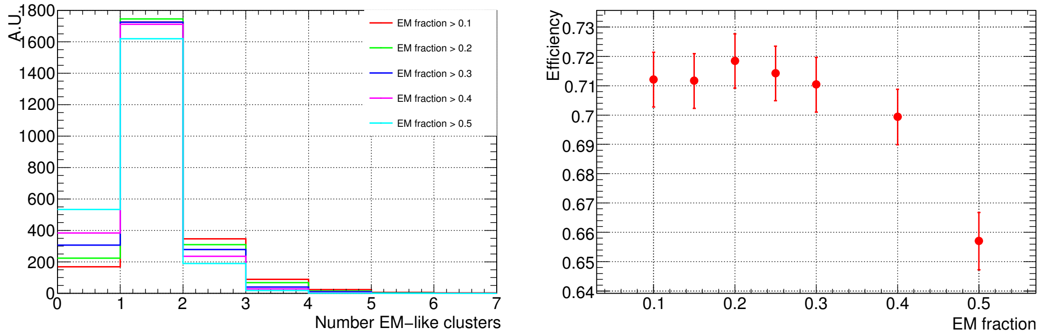

FIGURE 5.15: The left hand plot shows the number of clusters around the signal $\pi^{\pm}$ which are classified as EM-like, as $EMfraction$ is varied. The right hand plot show the fraction of events for which the signal π^0 cluster is the only cluster which is classified as EM-like, as $EMfraction$ is varied. Only the 1-π^0 mode is used, and the primary $\pi^{\pm}$ cluster is removed as described in the text.

This algorithm (`tauRec`)	0 EM clusters	1 EM clusters	2 EM clusters	> 2 EM clusters
0-π^0 mode	54%(74%)	30%(19%)	10%(2%)	7%(0)
1-π^0 mode	32%(33%)	36%(15%)	19%(3%)	13%(1%)
2-π^0 mode	19%(14%)	33%(10%)	25%(2%)	23%(1%)
J2 jets	41%(13%)	30%(3%)	18%(0)	11%(0)

TABLE 5.3: Single prong tau decay mode classification efficiency of the soft tau search algorithm. For comparison the classification efficiency of `tauRec` is shown in brackets. For a fairer comparison, only taus with 5GeV $< p_{T,vis} <$ 10GeV are considered here. `tauRec` classifications do not add up to 100% because only the track seed algorithm has a π^0 search algorithm. For reference the classification for QCD jets in a J2 sample is also shown.

5.1.2.4 Performance

Table 5.3 show the classification performance of this algorithm for the single prong mode signal taus which have been reconstructed. For comparison the classification performance for `tauRec` is also shown, for those signal tau which `tauRec` has reconstructed. The p_T range for the taus is limited to 5GeV $< p_{T,vis} <$ 10GeV. It should be noted that the classifications of `tauRec` do not add up to 100% because only the track seeded objects have a π^0 search algorithm. It is obvious that the classification performance of this algorithm is better than that for `tauRec`, but mainly due to the fact that most of the 1 and 2-π^0 signal tau which are reconstructed by `tauRec` are done so by the calorimeter seeded algorithm. This is because the low p_T tracks of these modes do not pass the track seed p_T threshold, while the clusters (which include the π^0 energy) do pass the calorimeter seed threshold.

There are a number of sources of classification inefficiency for the soft tau search algorithm. One of the main sources for decay modes with π^0s is from the $E_{cluster} > 1$GeV requirement for the π^0 search algorithm. Also, as mentioned above, the misclassification of secondary $\pi^\pm$ clusters as EM-like, and π^0 clusters as non-EM-like is significant in the low energy region. There are also some classification inefficiencies from losses of π^0 clusters outside the π^0 search cone.

Finally Figure 5.16 shows plots of the quality of the π^0 reconstruction for this algorithm. Energy resolution plots are shown in the top row. The bottom row shows the quality of the reconstruction of the $\pi^\pm, \pi^0$ system invariant mass. Only signal from 1-π^0 and 2-π^0 modes which have been correctly classified are shown. We can see that

The gaussian fit of the energy resolution of the 1-π^0 mode π^0 yields $\sigma = 9.5\%$. It is 14.2% for the first π^0 of the 2-π^0 mode. The reconstruction for the second π^0 of the 2-π^0 mode is poor and so the resolution has not been fit. Recall that this π^0 has a mean energy of only 3GeV. It is also in the vicinity of another, more energetic π^0, and also a $\pi^\pm$, making reconstruction very difficult. Nevertheless it seems that a cluster which corresponds to the second π^0 has been found, since the resolution plot is centered around zero.

The invariant mass of the 1-π^0 tau is reconstructed quite well, as can be seen from the comparison with the truth level distribution. The 2-π^0 reconstruction is not as good, due to the difficulty of reconstructing the 2nd π^0. Both of these distributions, among others, will be used in the discrimination of the signal soft taus from the background. This is the subject of the next section.

5.2 The soft tau likelihood method

Now that the information about soft tau candidate $\pi^\pm$ tracks, and soft tau candidate π^0 clusters is obtained, it is now necessary to further discriminate these isolated track+cluster systems from QCD jets. For this purpose a likelihood method was developed. The inspiration for the method was taken from the `tauRec` likelihood method, but with some modifications which are specific to the low energy region, and some modifications which are specific to this analysis. The likelihood method will be described below with an emphasis on its differences from the `tauRec` method. Then the performance of the method will be shown, with a comparison against `tauRec`.

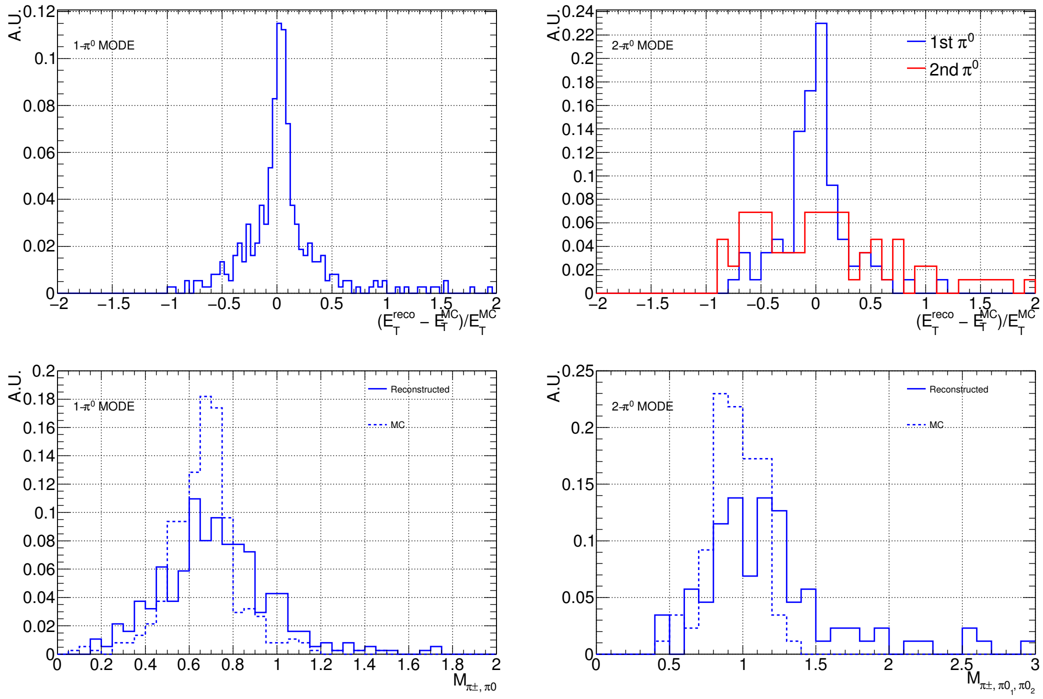

FIGURE 5.16: Plots showing the quality of the π^0 reconstruction in the soft tau search algorithm. The top row shows the energy resolution of the π^0s while the bottom row shows the invariant mass of the $\pi^{\pm}, \pi^0$ system. In the left column are the plots for the 1-π^0 mode, while the in the right column are the plots for the 2-π^0 mode. The invariant mass distributions are compared with the truth level distributions. Only correctly classified signal is shown.

5.2.1 Description

The majority of the discrimination variables employed by `tauRec` focus on discriminating taus by the relative narrowness of their overall structure. For very soft taus the discrimination power of these "narrowness" variables becomes worse. The advantage we have with soft taus though is that, while the opening angle of the decay products becomes larger and hence the tau jet becomes wider, at the same time the decay products become more distinguishable in the calorimeters. Thus rather than looking at the overall narrowness of the tau jet, it was decided to attempt to look at the narrowness of only the $\pi^{\pm}$ energy depositions, and to consider the π^0 components completely separately. This approach means that, effectively, we are only measuring the narrowness of a single $\pi^{\pm}$ in the calorimeter. We thus take advantage of the quite different topology of soft taus in the calorimeters.

Thus the basic thrust of the likelihood method is to

- Identify the EM-like depositions in the calorimeter that are likely to come from π^0 (as outlined in Section 5.1.2)

- Remove these depositions from the calorimeter and then calculate the "narrowness" likelihood variables.
- Use both $\pi^\pm$ and π^0 components to form other likelihood variables (such as invariant masses).

Below are listed separately the variables which are calculated with the EM-like clusters removed, and the variables which are calculated *using* the EM-like cluster information, along with variables which only use track information. Some of the variables are very similar to those used in `tauRec` (with some differences, for example, in the calorimeter cells which contribute), but are listed along with the other variables for completeness (refer to Appendix B for PDFs of these variables).

DISCRIMINATION VARIABLES USING CALORIMETER AND TRACK INFORMATION, EXCLUDING EM-LIKE CLUSTERS

- **The electromagnetic radius,** R_{em}:

  The electromagnetic radius R_{em} is defined as

$$R_{\mathrm{em}} = \frac{\sum_{i=1}^{n} E_{T,i}\sqrt{(\eta_i - \eta_{\mathrm{axis}})^2 + (\phi_i - \phi_{\mathrm{axis}})^2}}{\sum_{i=1}^{n} E_{T,i}}, \tag{5.3}$$

  where i runs over non-EM-like cells within a cone of $\Delta R < 0.4$ of the $\pi^\pm$ position [2] . This is similar to the variable used in `tauRec`.

- **Transverse energy width in the** η **strip layer,** $\Delta\eta$:

  The transverse energy width $\Delta\eta$ is defined as

$$\Delta\eta = \sqrt{\frac{\sum_{i=1}^{n} E_{Ti}^{\mathrm{strip}} (\eta_i - \eta_{\mathrm{axis}})^2}{\sum_{i=1}^{n} E_{Ti}^{\mathrm{strip}}}}. \tag{5.4}$$

  where the sum runs over all non-EM-like strip cells in a cone with $\Delta R < 0.4$ of the $\pi^\pm$ position and E_{Ti}^{strip} is the corresponding strip transverse energy. This is similar to the variable used in `tauRec`

- **Isolation fraction in the calorimeter,** I:

  The isolation fraction is defined as

$$I = \frac{\sum_i E_{T,i}}{\sum_j E_{T,j}}, \tag{5.5}$$

[2] From here "non-EM-like cells" means cells belonging to topoclusters which have not been classified as EM-like, and "$\pi^\pm$ position" means the position of the $\pi^\pm$ at the relevant layer of the calorimeter.

where the i and j run over all non-EM-like cells belonging to cones around the $\pi^{\pm}$ position with $\Delta R < 0.2$ and $\Delta R < 0.4$, respectively, and $E_{T,i}$ and $E_{T,j}$ denote the cell E_T. This is similar to the `tauRec` isolation variable, except that the numerator is the sum of cell with $\Delta R < 0.2$ instead of $0.1 < \Delta R < 0.2$.

- **Ratio of hadronic and EM energy,** $HADoverEM$:

  The ratio of hadronic to EM energy is defined as

$$HADoverEM = \frac{\sum_{i=1}^{n} E_{T,i}}{\sum_{j=1}^{n} E_{T,j}} \tag{5.6}$$

  where the i and j run over all non-EM-like cells in cones of $\Delta R < 0.4$ of the $\pi^{\pm}$ position, in the hadronic calorimeter, and the EM calorimeter respectively.

- E_T^{EM} **over** p_T **of the seed track,** E_T^{EM}/p_T :

  The ratio of sum of the E_T of non-EM-like cells within $\Delta R < 0.4$ of the $\pi^{\pm}$ position to the p_T of the seed track. Only cells from the EM calorimeter are used. This is similar to the variable used in `tauRec`.

- E_T^{HAD} **over** p_T **of the seed track,** E_T^{HAD}/p_T :

  The ratio of sum of the E_T of non-EM-like cells within $\Delta R < 0.4$ of the $\pi^{\pm}$ position to the p_T of the seed track. Only cells from the hadronic calorimeter are used.

- **Number of hits in the** η **strip layer**:

  The number of hits in the finely segmented first layer of the EM calorimeter with E>100MeV and within $\Delta R < 0.4$ of the $\pi^{\pm}$ position are counted. Only non-EM-like cells are considered. This is the same as for `tauRec`, except that the threshold is reduced to 100MeV (which is still well above the 12 - 15MeV noise level in the strip layer).

DISCRIMINATION VARIABLES USING CALORIMETER AND TRACK INFORMATION, USING EM-LIKE CLUSTERS

Note that these variables are only calculated for the case that exactly one or two EM-like clusters are identified.

- **The invariant visible mass,** $M_{invariant}$:

  $M_{invariant}$ is defined as the invariant mass of the seed track and the EM-like clusters.

- **The distances between the $\pi^\pm$ and the EM-like clusters, $\Delta R_{\pi^\pm,\pi^0_{1,2}}$**:

  $\Delta R_{\pi^\pm,\pi^0_{1,2}}$ is defined as the distance between the $\pi^\pm$ at the interaction point, and the 1 or 2 EM-like clusters.

- **The distance between the two EM-like clusters, $\Delta R_{\pi^0_1,\pi^0_2}$**:

  $\Delta R_{\pi^0_1,\pi^0_2}$ is defined as the distance between the two EM-like clusters.

DISCRIMINATION VARIABLES USING ONLY TRACK INFORMATION

- **The distance to the closest track, $\Delta R_{\pi^\pm,closesttrack}$**:

  $\Delta R_{\pi^\pm,closesttrack}$ is defined as the distance between the seed track and the closest track of "isolation track" quality, as defined in Table 5.1. This is another measure of the isolation of the system, but using information from the inner detector.

- **The number of tracks in the isolation zone, $NTRACK\_02\_04$**:

  $NTRACK\_02\_04$ is defined as the number of tracks of "isolation track" quality, as defined in Table 5.1, in the region $0.2 < \Delta R < 0.4$. Recall that the seed track is *required* to be isolated within $\Delta R < 0.2$.

- **Lifetime signed pseudo impact parameter significance**:

  This parameter is exactly the same as that used for `tauRec`. It is a measure of the significance of the impact parameter. Refer to Section 4.2.7.3 for a complete description.

The likelihood variable using these variables is calculated in the same way as for the `tauRec` algorithm (refer Section 4.2.7.3). PDFs for the signal and background were created from Monte Carlo simulations. Signal PDFs were created using the signal soft tau from the coannihilation region sample. Background PDFs were created with a J2 sample. Separate PDFs have been created for 0, 1 and 2 π^0 modes.

The same likelihood variable as `tauRec` is calculated from these PDFs:

$$d = \sum_{k=1}^{k=nVars} \log \frac{p_k^S(x_k)}{p_k^B(x_k)} \tag{5.7}$$

where the sum is over the discrimination variables, x_k is the value of the variable k for the candidate, and $p_k^S(x_k)$ and $p_k^B(x_k)$ are the probability density at the value x_k for the signal PDF and for the background PDF respectively. No electron veto has been implemented for this method.

The classification by the π^0 cluster finding algorithm determines which PDF set is used (0,1 or 2 π^0). For candidates with greater than 2 EM-like clusters, the discrimination variables using the EM-like cluster information are not calculated, and the 0-π^0 PDF set is used. PDFs were binned by the momentum of the seed track as follows: 2GeV $<$ $p_{track} <$ 5GeV, 5GeV $< p_{track} <$ 10GeV and $p_{track} >$ 10GeV.

Figures showing the final PDFs used for the likelihood method are located in Appendix B. They are divided by decay mode classification (single prong 0-π^0, 1-π^0 and 2-π^0), and then further by seed track momentum range (2GeV $< p_{track} <$ 5GeV, 5GeV $< p_{track} <$ 10GeV and $p_{track} >$ 10GeV). The signal and the background PDFs are shown superimposed in these plots. We can see that the discrimination power of some variables is much better than others. In particular it is obvious that the discrimination power of the track based variables is relatively powerful. This is likely due to the fact that the depositions from low energy object in the calorimeter tends to be dispersed. We can also see that the variables involving the π^0 clusters adds extra discrimination power to the likelihood. This is an improvement on the `tauRec` method which only used one variable involving π^0 candidates ($M_{invariant}$), and then only for the track seeded algorithm.

In addition to the different approach for creating the likelihood variables mentioned above, we have implemented another somewhat analysis specific modification to the likelihood method. The discrimination power of the "narrowness" and "isolation" variables used in this method are contingent on the activity in the vicinity of the soft tau candidate. That is to say that if there are tracks close to the soft tau candidate which come from other objects, or if there are depositions in the calorimeter close to the candidate which come from other objects, the power of the variables is diminished. It was shown in Figure 3.4 that the signal soft tau is often very close to the very energetic signal hard tau. Thus, firstly, tracks which are associated to the reconstructed hard tau candidate are excluded from the calculation of variables which involve track information (*e.g.* the number of tracks in the area $0.2 < \Delta R < 0.4$ around the soft tau candidate). Secondly, when calculating likelihood variables involving calorimeter information, if the soft tau candidate is within $\Delta R < 0.8$ of the hard tau candidate, only calorimeter cells in the half cone *furtherest away* from the hard tau candidate were used. Figure 5.17 shows a schematic illustrating the half cone method. This method was *not* used for the π^0 cluster search. The improvement in discrimination power using this method will be discussed below.

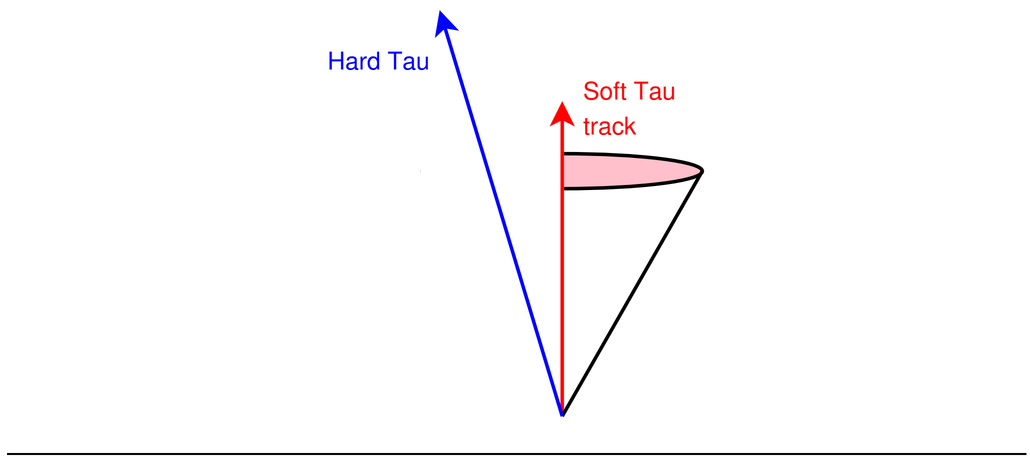

FIGURE 5.17: When the soft tau candidate is within $\Delta R < 0.8$ of the hard tau candidate, only the half cone furtherest from the hard tau candidate is used for calculating a number of the likelihood variables.

5.2.2 Performance

Figure 5.18 shows final discrimination power of the likelihood functions for the signal and the background. Likelihood functions for 0, 1 and 2-π^0 modes are shown and the functions are plotted separately for the momentum ranges in which the likelihood variables are binned. Only the correctly classified signal is shown. We can see that, indeed, the extra variables using the π^0 information do add to the discrimination power of the likelihood method. But as will be described below, this power is diminished when candidates are incorrectly classified.

Figure 5.19 show the improvements in the discrimination power of the likelihood functions when the above-mentioned half-cone method is used. Only soft tau candidates within the cut-off distance of $\Delta R < 0.8$ are shown. We can see that this method provides a small improvement in discrimination power for the signal soft taus which are close to the signal hard tau.

Figure 5.20 compares the performance of this method's likelihood function with that of `tauRec`. As in Section 4.3.4 this is shown as a line in the ϵ^{jet}, ϵ^{signal} plane, where similarly ϵ^{signal} is defined as

$$\epsilon^{signal} = \frac{\text{number matched soft candidates with } LLH > LLH^{cut}}{\text{number of MC taus}} \tag{5.8}$$

and ϵ^{jet} is defined as

$$\epsilon^{jet} = \frac{\text{number matched soft candidates with } LLH > LLH^{cut}}{\text{number of MC jets}} \tag{5.9}$$

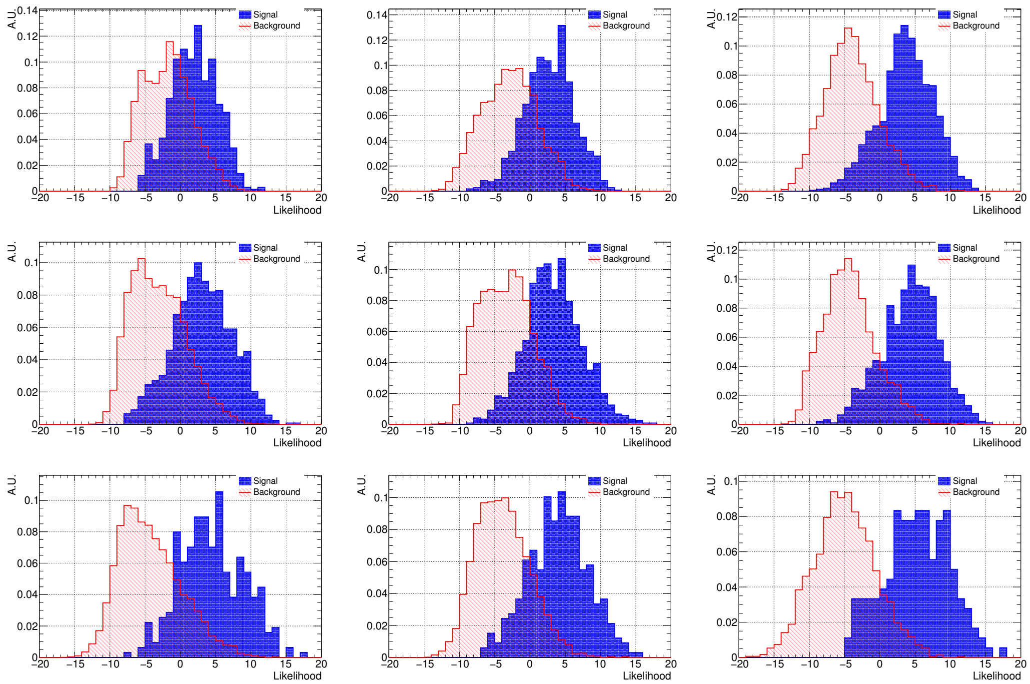

FIGURE 5.18: The likelihood functions of the soft tau likelihood method for the 0-π^0 mode (top), 1-π^0 mode (middle) and 2-π^0 mode (bottom). The functions are shown separately for candidates with seed tracks in the range $2 <$ GeV$p_{track} <$ 5GeV (left), $5 <$ GeV$p_{track} <$ 10GeV (middle) and $10 <$ GeVp_{track} (right). The signal here are the correctly classified coannihilation region soft taus, while the background are jets in a J2 QCD sample.

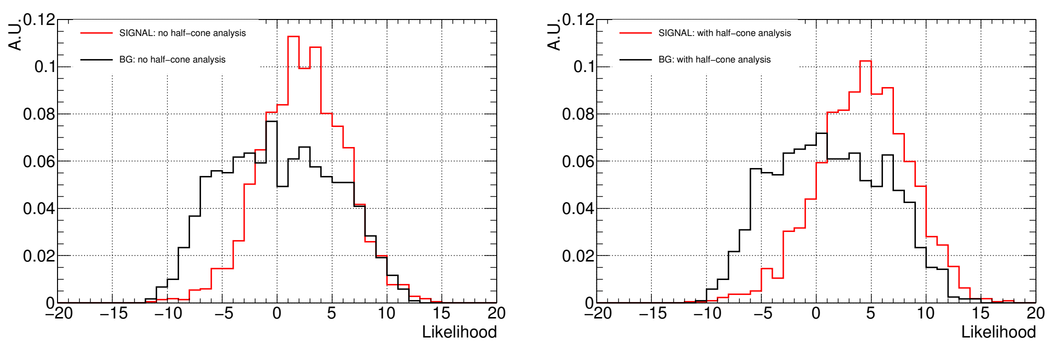

FIGURE 5.19: The improvement in the soft tau likelihood method when the half-cone method is used. The left hand plot shows the likelihood function for taus/jets which are within $\Delta R < 0.8$ of the hard tau candidate, when the half-cone method is *not* used. The right hand plot shows the same but for when the half-cone method *is* used.

where "matched" means for the signal that the soft tau candidate track has been matched to within $\Delta R < 0.01$ of the truth level $\pi^{\pm}$, and for background means that the soft tau candidate has been matched to within $\Delta R < 0.2$ of a truth level jet. For ϵ^{signal} the signal soft tau from the coannihilation region is used while a J2 sample is used for ϵ^{jet}. No hard tau candidate requirement is made for this comparison. Only taus and jets with $|\eta| < 2.5$ are considered and only taus from a particular decay mode are considered at a time. The denominator for ϵ^{jet} is all MC jets in the kinematic region. Figures are shown separately for the 0, 1 and 2-π^0 modes and for different regions of the p_T spectrum. For a fair comparison a seed track cut of $p_{T,track} > 5$GeV is used for the soft tau method, which is 1GeV lower than the track cut used for `tauRec` in order to compensate for the increase in the maximum attainable efficiency that the calorimeter seeded algorithm of `tauRec` provides [3].

We can see that in the region 5GeV $< p_T <$ 10GeV the new soft tau discrimination method performs significantly better than `tauRec` for the 0 and 1-π^0 modes. The 2-π^0 modes performs slightly worse. The better performance of the lower π^0 multiplicity modes can be understood in two ways. Firstly the classification efficiency for the lower multiplicity modes is significantly better, which means that the calculated discrimination variables are being compared to the "correct" PDF set. Thus although the extra π^0 variables do provide extra discrimination power for the higher π^0 multiplicity modes, misidentification of π^0 clusters will result in a degradation in performance.

Secondly the `tauRec` algorithm has an advantage over the soft tau method since it has a calorimeter seeded algorithm. The calorimeter seeded algorithm has a particular advantage for higher π^0 multiplicity modes in the low energy region since, for these modes the $\pi^{\pm}$ track will be particularly soft, and so will often fall below the threshold of a track seeded algorithm. On the other hand the combined energy of the $\pi^{\pm}$ and π^0s is more likely to pass the calorimeter seed threshold. In addition the π^0 decay conversion electrons will contribute significantly to inefficiencies in the $\pi^{\pm}$ passing seed track isolation requirements.

We can also see that in the higher energy region of 10GeV $< p_T <$ 20GeV, the performance of `tauRec` is better for all modes. This can be understood again from the advantage that `tauRec` gains from having a calorimeter seeded algorithm. The contribution to the reconstruction efficiency coming from the calorimeter seeded algorithm becomes very significant when the tau energy is greater than the calorimeter seed threshold.

Nevertheless the overall performance for the soft tau tagging algorithm is better in the region 5GeV $< p_T <$ 10GeV as can be seen in the combined performance plot at the

[3]The cut on the seed track ultimately used for the optimisation of the signal to background ratio for the $M_{\tau,\tau}$ reconstruction is actually lower than this, as will be described in Section 6.3

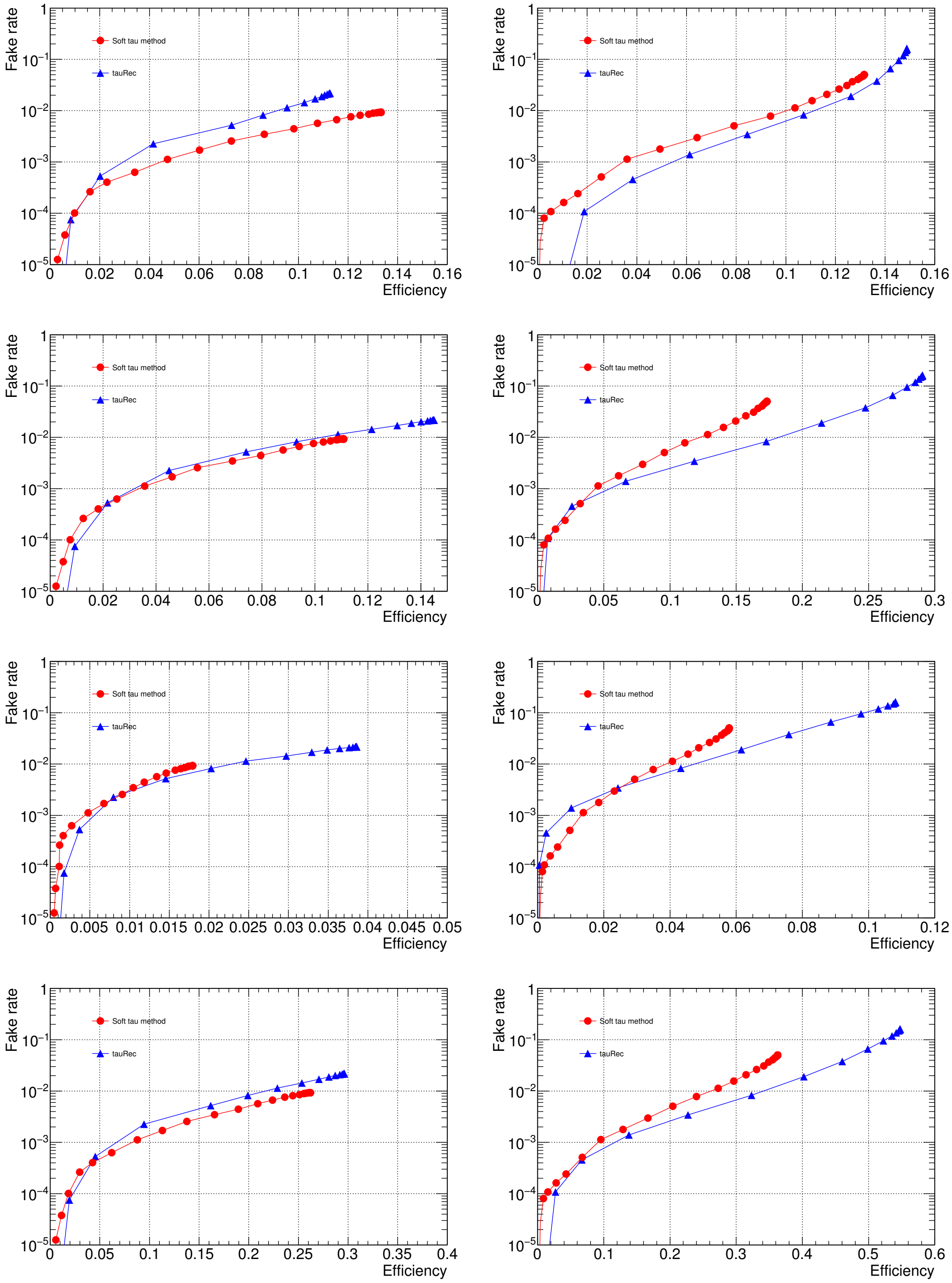

FIGURE 5.20: Fake rate vs. efficiency plots comparing the performance of the soft tau likelihood method with `tauRec`. Comparisons are made for 0-π^0 taus (top), 1-π^0 taus (2nd row), 2-π^0 taus (3rd row) and the combined performance for all single prong modes (bottom). The left hand plots are for the taus/jets with 5GeV $< p_T <$ 10GeV and the right hand plots are for taus/jets with 10GeV $< p_T <$ 20GeV. A seed track cut of $p_{track} >$ 5GeV is used for a fair comparison with `tauRec`.

bottom left of Figure 5.20. Furthermore the soft tau tagging algorithm has also been optimised for even lower energies than this, where the `tauRec` algorithm efficiency is virtually zero due to its high seed thresholds. The majority of the signal soft tau which we are attempting to tag have $p_T < 10\text{GeV}$, so the performance of the algorithm in the region $p_T > 10\text{GeV}$ is of secondary importance. It will be shown in the next section that indeed the better performance of the soft tau tagging algorithm in the lower energy region results in a better reconstruction of the $M_{\tau,\tau}$ endpoint as compared to `tauRec`.

Chapter 6

$M_{\tau,\tau}$ Endpoint Analysis

In Chapter 4 the algorithm to be used for reconstructing the coannihilation region signal hard tau (`tauRec`) was described. In Chapter 5 the development of a new algorithm for reconstructing the coannihilation region signal soft tau was outlined. The following chapter presents the final analysis of the coannihilation region $M_{\tau,\tau}$ distribution endpoint reconstruction.

The chapter will begin with the study of the selection of SUSY events from the copious standard model background which will arise in LHC collisions. This includes the requirement of a signal hard tau candidate using `tauRec`. The optimisation of the selection of the signal soft tau will then be outlined. Finally the analysis of the resulting $M_{\tau,\tau}$ distribution will be given.

Prior to all of this though it is necessary to briefly give some technical details of the definitions of physics objects used. This is the subject of the next section.

6.1 Physics object definitions

Table 6.1 outlines the definitions of all of the ATLAS standard reconstruction objects used for this analysis (excludes the soft tau definition). The recommendations for physics object identification cuts given in reference[21] were used.

As well as the definition of physics objects it is also necessary for a procedure for so-called "overlap removal" to be implemented. "Overlap" arises, for example, when a set of calorimeter clusters is reconstructed (and identified) as different physics objects. This occurs because reconstruction algorithms are executed independently. Overlap removal needs to be implemented in order to avoid double counting of objects. The procedure for removing such overlaps is as follows:

Physics object	**Algorithm**	**Athena container name**	**Identification cuts**
Jets	0.4 radius cone, topological cluster input, H1 calibration	`Cone4H1TopoJets`	$\eta < 2.5$, $p_T > 20$GeV
Electrons	`egamma`	`ElectronCollection`	$\eta < 2.5$, $p_T > 10$GeV, medium" ID cut, `etcone20` isolation
Muons	`STACO`	`StacoMuonCollection`	$\eta < 2.5$, $p_T > 10$GeV isCombinedMuon, $\chi^2/d.o.f. < 100$, `etcone20` isolation
Taus	`tauRec`	`TauRecContainer`	$\eta < 2.5$, $p_T > 15$GeV, "medium" LLH cut, 1,3 tracks, $\|Q\| == 1$, e, μ veto
E_T^{miss}	"Refined Calibrated"	`MET_RefFinal`	N/A

Table 6.1: ATLAS standard reconstruction physics object definitions used for this analysis. Object overlap removal procedure is described in the text.

Reconstructed taus which are selected using the criteria of Table 6.1 already have an effective electron veto applied so that electrons faking taus are reduced. This electron veto has a better performance than a simple overlap removal procedure between electrons and taus as described in Section 4.2.7.3. Thus rather than removing taus which overlap electrons, in this analysis we remove electrons which overlap taus. This is in order to maintain tau efficiency as much as possible. Furthermore we remove jets which overlap taus. The overlap criteria used is $\Delta R < 0.4$ between the reconstructed objects.

The jet reconstruction algorithm can reconstruct an electron as a jet. On the other hand electrons selected with the criteria of Table 6.1 have very few jets faking electrons. Thus a jet overlapping an electron within $\Delta R < 0.2$ is removed.

Electrons and muons can arise from the decay of particles within a jet. These electrons and muons are not of interest in themselves in this analysis, and so electrons that are between $0.2 < \Delta R < 0.4$ of a jet, or muons which are within $\Delta R < 0.4$ of a jet are removed.

6.2 SUSY selection

The overall phenomenology of SUSY events was outlined in Section 3.1. The main characteristics which distinguish SUSY events from SM background are a number of energetic jets arising from the cascade decay of gluinos and squarks, possible leptons, and large E_T^{miss} arising from the escape of two $\tilde{\chi}_1^0$ from the detector. In this section we describe the SUSY selection cuts used to isolate a pure SUSY sample. Note that all of the following plots have a requirement of a tau with $p_T > 15$GeV.

For this analysis the requirement on the number of energetic jets is set to two. Figure 6.1 shows plots of E_T^{miss} vs. $P_T^{jet1} + P_T^{jet2}$ for the signal events from the coannihilation region sample and for the various SM processes. Recall that the definition of effective mass used for this analysis only involves the two hardest jets and E_T^{miss}: $M_{eff} = E_T^{miss} + P_T^{jet1} + P_T^{jet2}$. Thus a cut on effective mass of x can be viewed in the E_T^{miss}, $P_T^{jet1} + P_T^{jet2}$ plane as a line running from $E_T^{miss} = x$ to $P_T^{jet1} + P_T^{jet2} = x$. In order to supplement the rejection of copious soft tau background , rather hard cuts on E_T^{miss}, P_T^{jet1}, P_T^{jet2} and M_{eff} are used for this analysis to reduce SM background as much as possible. The following cuts on P_T^{jet1}, P_T^{jet2} and E_T^{miss}, are used

1. $P_T^{jet1} > 180$GeV
2. $P_T^{jet2} > 90$GeV
3. $E_T^{miss} > 200$GeV
4. $M_{eff} > 700$GeV

These cuts are illustrated in the plots of Figure 6.1 [1]. The background process that will pass these cuts with the greatest efficiency is $t\bar{t}$ which also has energetic jets and large E_T^{miss} which comes from W decay. Of course significant numbers of other SM processes such as QCD di-jet will pass these initial cuts due to their sheer numbers of statistics but the efficiency is rather smaller.

After this first set of cuts the largest background still remaining is QCD di-jet processes which have large jet transverse energy (>J4). In order to reduce these further a requirement of a minimum distance in ϕ between E_T^{miss} and the first and second jets is made.

5. $\Delta\phi_{jet1,MET} > 0.2$
6. $\Delta\phi_{jet2,MET} > 0.2$

Correlation plots between $\Delta\phi_{jet1,MET}$ and $\Delta\phi_{jet2,MET}$ are shown in Figure 6.2 with these cuts superimposed. These cuts effectively reduce the QCD contribution by around

[1] Note that with separate cuts on the P_Ts of the first and second jets, the vertical cut on $P_T^{jet1} + P_T^{jet2}$ is not strictly accurate, but is drawn for illustrative purposes.

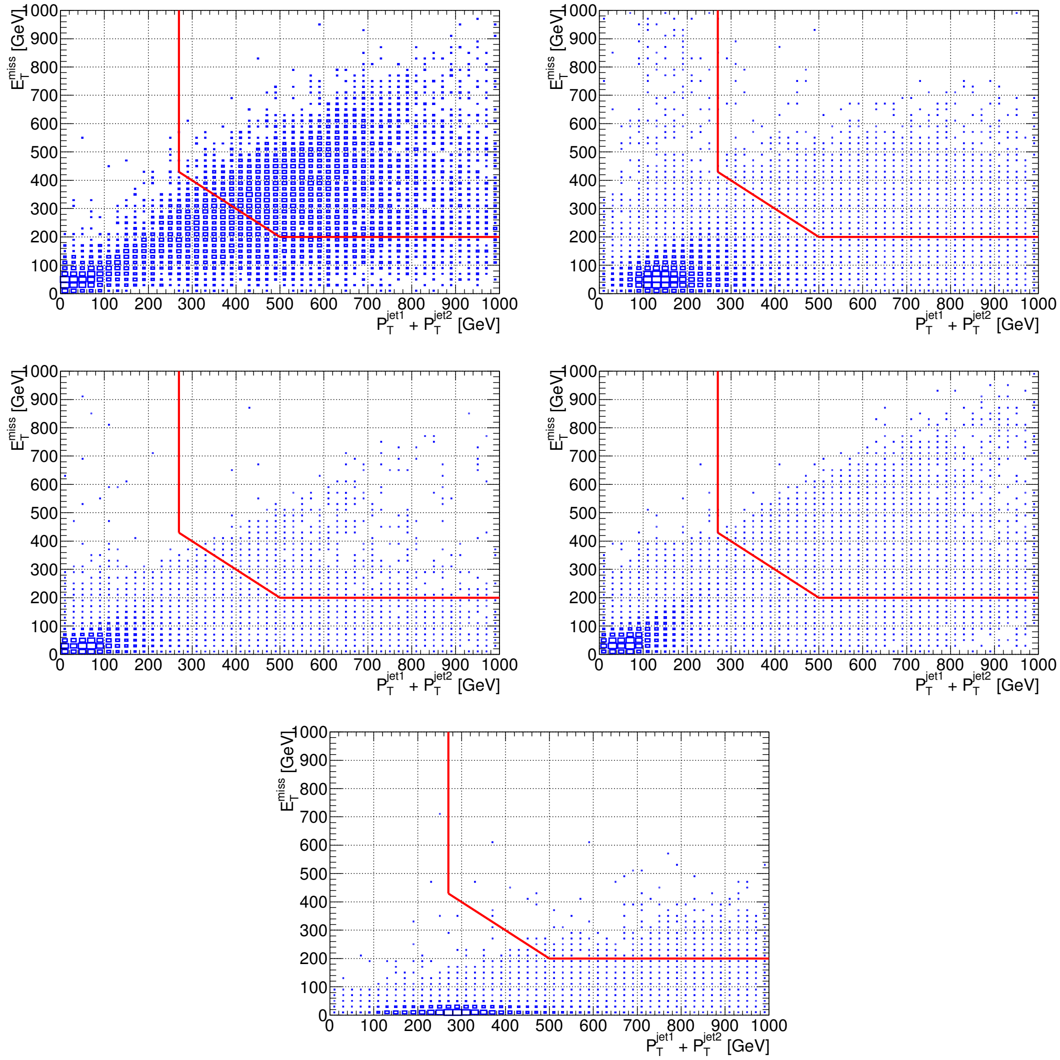

FIGURE 6.1: E_T^{miss} vs $P_T^{jet1} + P_T^{jet2}$ for the coannihilation region signal events (top left), $t\bar{t}$ (top right), $W \rightarrow \tau, \nu$ (middle left), Z (middle right) and QCD (bottom). The cuts imposed on these quantities are superimposed. Normalisation for each plot is arbitrary.

70% while reducing the signal by only 3%. This is because the E_T^{miss} from QCD di-jet processes arises either from neutrinos coming from weak processes within the jet (real E_T^{miss}), or from mismeasurements of jet energy in the calorimeter (fake E_T^{miss}). E_T^{miss} in coannihilation events mostly comes from the two $\tilde{\chi}_1^0$ whose directions are not correlated to the directions of the cascade jets.

In order to reduce the contributions of W and Z boson decay to electrons and muons we also apply a lepton veto to the analysis. The reconstruction efficiency of electrons and muons in the ATLAS detector is relatively very good and so this cut allows us to ignore the contributions from $W \rightarrow e, \nu$, $W \rightarrow \mu, \nu$, $Z \rightarrow e, e$ and $Z \rightarrow \mu, \mu$, since they will be insignificant relative to $W \rightarrow \tau, \nu$ and $Z \rightarrow \tau, \tau$.

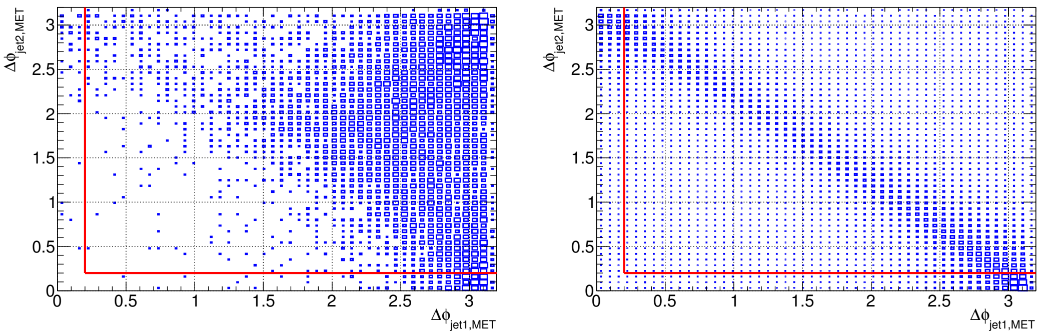

FIGURE 6.2: $\Delta\phi_{jet2,MET}$ vs. $\Delta\phi_{jet1,MET}$ for coannihilation region signal events (left) and for QCD (right). Cuts made on these quantities are shown superimposed.

7. Lepton veto

This cut is also quite effective at reducing further $t\bar{t}$ contributions, since the branching ratio of "not fully hadronic" decay of $t\bar{t}$ is 54%.

Next we make a requirement of a `tauRec` object with $p_T > 15$GeV .

8. $P_{T,\tau} > 15$GeV

While this is effective at reducing the standard model background, its most important role is in reducing the combinatorial background from SUSY events. Recall that only 7% of SUSY events will contain the "golden" decay chain so in order to cleanly reconstruct the $M_{\tau,\tau}$ endpoint it is necessary to reduce this SUSY background as much as possible. The SUSY combinatorial background efficiency for this cut is 5% while the signal efficiency is 40%.

The final cut that we make before the soft tau selection is on M_T. For this analysis the transverse mass is calculated using the hard tau candidate and the E_T^{miss}. Recall that the M_T distribution from $W \rightarrow \tau, \nu$ will exhibit a Jacobian peak at the W mass so that a cut around the W mass is effective at reducing this contribution. In fact, a cut on M_T is also quite effective for reducing contributions from $t\bar{t}$. This is because a semi-leptonically decaying $t\bar{t}$ event will produce an on shell W boson which can go via $W \rightarrow \tau, \nu$. Figure 6.3 shows the M_T distributions for signal, $W \rightarrow \tau, \nu$, and $t\bar{t}$ events, where indeed we can see the peak around the W mass (80GeV) for $W \rightarrow \tau, \nu$ and $t\bar{t}$. This peak is is somewhat smeared compared to, for example, $W \rightarrow e, \nu$, due to the existence of the second neutrino coming from the τ decay, and from jets faking taus. For this analysis we make a cut on M_T of 90GeV

9. $M_T > 90\text{GeV}$

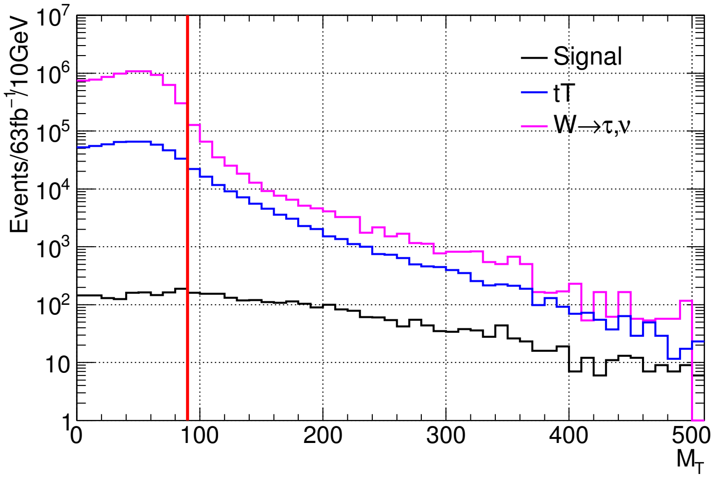

FIGURE 6.3: Comparison of M_T for the coannihilation region signal events, $W \to \tau, \nu$ and $t\bar{t}$.

6.3 Soft tau selection

Now that the selections have been applied to heavily reduce the SM contributions, and to some extent the SUSY BG contribution, the final selection that must be made is for the signal soft tau. The details of this algorithm were outlined in Chapter 5 but here we optimise the cut on the soft tau candidate track, $p_{T,track}$, and also the likelihood of the candidate LLH. Figure 6.4 show a plot in two dimension of $S/\sqrt{N}$ as a function of the cut on $p_{T,track}$ and the LLH, where S is the number of signal events for which the signal hard and soft taus have been correctly selected by their respective algorithms, and N is the total number of events which remain with both a hard and soft tau candidate. This quantity was chosen as the optimising parameter since the uncertainty in the final fit of the $M_{\tau,\tau}$ spectrum will depend on the total statistics remaining N. Only the contributions from background SUSY events are used for this plot, as the SM background contributions are small in comparison. We can see that the optimal cuts on the soft tau candidates are at around $p_{T,track} > 3\text{GeV}$ and $LLH > 3$. Unfortunately it was necessary to enlarge the acceptance of this cut by changing it to $p_{T,track} > 2.5\text{GeV}$ and $LLH > 0$ in order to maintain statistics in the SM samples. This means a drop in $S/\sqrt{N}$ from 6.40 to 6.16

As a preliminary to the presentation of the final cut flow we study the efficiency of the likelihood method for selecting the signal soft tau from out of a number of soft tau

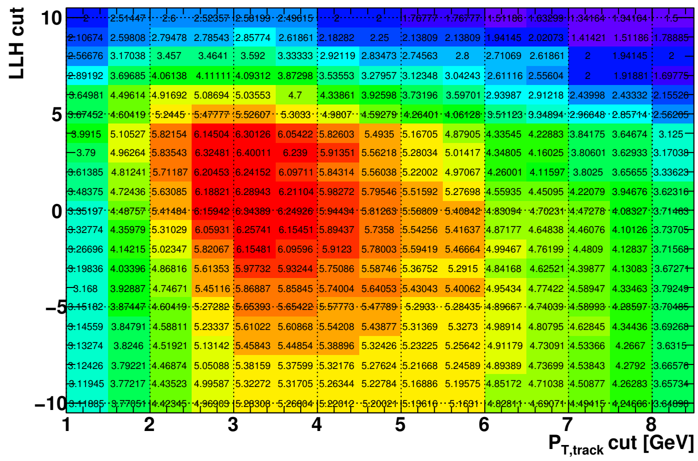

FIGURE 6.4: $S/\sqrt{N}$ as a function of the cut on soft tau candidate $p_{T,track}$, and the likelihood cut, where S is the number of signal events for which the hard and soft taus have been correctly selected, and N is the total number of events which remain with a candidate hard and soft tau.

candidates around the signal hard tau. That is we would like to know how often the likelihood method actually correctly selects the signal soft tau when there is greater than one candidate remaining.

The blue line in Figure 6.5 shows the number of soft tau candidates which remain around the signal hard tau after all of the selection cuts, but before the soft tau likelihood cut. Only events for which the hard tau is correctly reconstructed, and the soft tau is reconstructed within the search cone, are shown. We can see that, before the soft tau likelihood cut 52% of the events are background free (there are no other soft tau candidates except for the signal soft tau). 96 of the events have more than one soft tau candidate in the search cone (there are other tracks besides the signal soft tau track within the search cone). Of these 96 events, 63 of the signal soft tau tracks pass the likelihood cut, then of these 63, 56 are correctly selected as the most tau-like candidate. Thus we can see that the selection efficiency for the soft tau likelihood method, for the case that there is more than one candidate to choose from, is at least 58%. For reference, the number of soft tau candidates which remain around the signal hard tau *after the likelihood cut* is shown as the red line if Figure 6.5. Only events for which the signal soft tau passes the likelihood cut are shown.

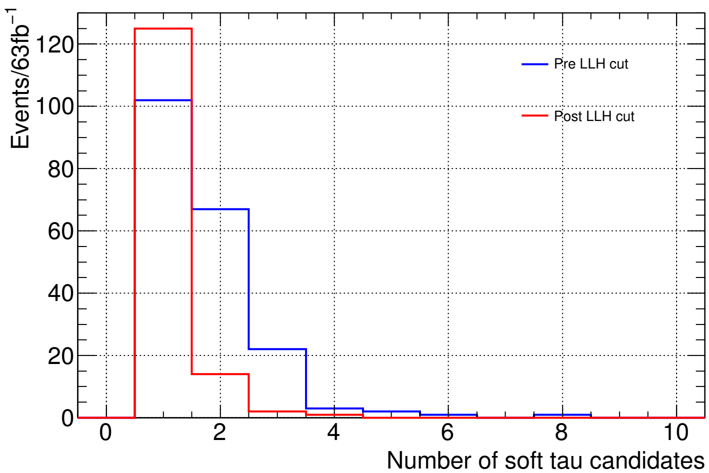

FIGURE 6.5: The number of soft tau candidates which remain in the soft tau search area before (blue) and after (red) the soft tau likelihood cut. Only events for which the signal soft tau survives the selection cuts are shown for each plot.

6.4 Final cut flow

Table 6.2 show the final cut flow, before the OS-SS subtraction. It includes both the SUSY selection and the soft tau selection, for the signal and the various backgrounds. It shows the cut flow normalised to the signal sample integrated luminosity of 63fb^{-1}. The samples used were outlined in Section 4.1. For this study we assume that the trigger rate for the events which pass the SUSY cuts will be close to 100%, since we require such a large E_T^{miss}, and high energy jets.

Note that signal events for which the signal hard tau is not selected as the hardest tau by `tauRec` are migrated to "SUSY BG" at that cut. Similarly for the soft tau selection. 1 of the final 150 signal events actually had the signal soft tau (coming from the $\tilde{\tau}_1$) identified by `tauRec`, and the signal hard tau identified by the soft tau search algorithm. The signal soft tau was a factor 2.8 harder than the signal hard tau for this particular event. 1 event for which the hard and soft taus are correctly reconstructed has the hard tau with a misidentified charge. This event is added to the SUSY background category.

Complimentary to this table is Figure 6.6 which shows the cut flow in graphical form. We can see that the major background which remains is the SUSY combinatorial BG, which is a factor 3 larger than the combined SM background. We can see that the major contributions from SM processes arises from both $t\bar{t}$ and $W \to \tau, \nu$, which both have significant E_T^{miss}.

There are a couple of points to note about the Monte Carlo samples used for this final analysis. Recall that with the lepton veto, the W and Z to μ and e become negligible

Cut	Signal	SUSY BG	$t\bar{t}$	W	Z	QCD
No cut	11.9k	151k	6.78M	59.7M	21.0M	9.91G
$P_T^{jet1} > 180$GeV	8.88k	120k	784k	1.51M	594k	3.50G
$P_T^{jet2} > 90$GeV	7.80k	105k	603k	879k	277k	3.16G
$E_T^{miss} > 200$GeV	6.11k	85.0k	77.1k	81.9k	103k	267k
$M_{eff} > 700$GeV	5.94k	82.8k	59.6k	66.7k	82.3k	263k
$\Delta\phi_{jet1,MET} > 0.2$	5.93k	82.7k	59.2k	66.7k	82.2k	189k
$\Delta\phi_{jet2,MET} > 0.2$	5.75k	80.7k	51.4k	59.5k	76.4k	75.2k
Lepton Veto	3.40k	56.9k	26.0k	47.3k	76.3k	75.2k
$p_{T,\tau} > 15$GeV	1.33k	3.08k	3.92k	10.9k	413	
$M_T > 90$GeV	905	1.86k	494k	465	341	
Soft tau selection	150 ± 12	451 ± 21	75 ± 17	54 ± 54	18.7 ± 8.4	

Table 6.2: The cut flow of the SUSY and soft tau selections, normalized to an integrated luminosity of 63fb^{-1}. Only the significant samples, as described in the text, are used.

compared to their τ decay counterparts, and so ESD samples were not created for these and they are not included in the final analysis. Also, ESD samples were not created for Z and W samples which would become insignificant after the jet cuts (*e.g.* $Z \to \nu, \nu$ with 0 or 1 parton).

Also, only the QCD samples >J4 (leading jet $E_T > 140$GeV) were found to have significant statistics after the cuts on $\Delta\phi_{jet,MET}$, and so only these are included in the table [2]. Even with this restriction it was impossible to create large enough QCD samples such that statistics remain at the final soft tau cuts. Statistics remain for each of the QCD samples only up to the lepton veto. An estimate was made on the combined efficiency of the hard tau p_T cut, the M_T cut, and the soft tau cuts by imposing these cuts, with a range of looser SUSY cuts preceding them. A conservative estimate of the efficiency of these cuts of 10^{-4} was made. It is expected that the contribution to the $M_{\tau,\tau}$ spectrum from QCD should be similar to that of $Z \to \nu, \nu$. We will show that the contribution from $Z \to \nu, \nu$ is negligible compared to that from the SUSY combinatorial background.

Of interest here is whether or not the two tau candidates which are selected by the above procedure are true taus or not. Table 6.3 summarises this information. We can see that for 47% of the SUSY background at least one of the hard or soft candidates is a true tau. For 9% of the SUSY background both candidates are true. 78% of the True/Fake SUSY background arises from correct identification of the signal hard tau with incorrect identification of the signal soft tau. 24% of the True/True background arises from correct identification of the signal hard tau with identification of a separate tau from the signal soft tau in the event.

[2] Statistics for other QCD samples run out at earlier cuts, but they quickly become insignificant compared to those >J4 due to the low energy of their jets

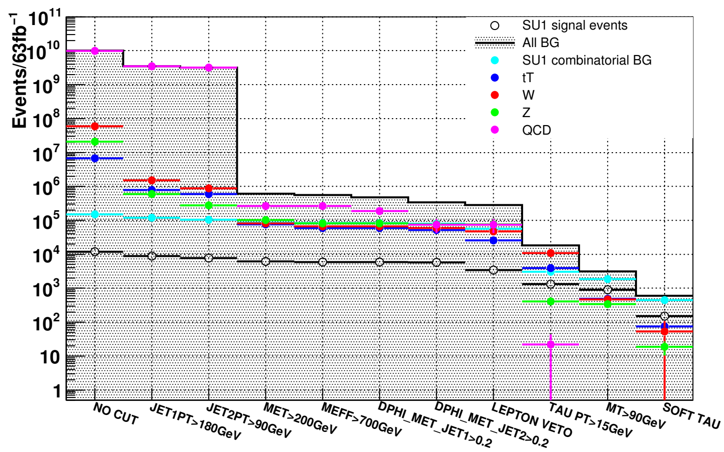

FIGURE 6.6: The cut flow of the SUSY and soft tau selections. Only the significant samples, as described in the text, are used.

Process	True/True	True/Fake	Fake/True	Fake/Fake	Total
SUSY BG	41	124	46	240	451
$t\bar{t}$	1	4	2	19	26
$W \to \tau, \nu$	0	0	0	1	1
$Z \to \nu, \nu$	0	0	0	5	5

TABLE 6.3: The proportions of the backgrounds which come from true taus. The raw Monte Carlo statistics for each sample are listed here.

In the SM background there are relatively few true taus arising from the selection procedure, though the statistics are very limited for the $W \to \tau, \nu$ case. In comparison, the large true tau contribution in the SUSY background is to be expected due to the enhanced SUSY cross section for decay to taus and the large boost usually imparted to these taus, plus the fact that many of the signal hard taus are relegated to background from the misidentification of the signal soft tau.

6.5 $M_{\tau,\tau}$ contribution from the backgrounds

The final step for this analysis is to subtract the $M_{\tau,\tau}$ distribution of the SS tau candidate pairs from that of the OS sign pairs. This will reduce the uncorrelated pair background since uncorrelated SS pairs will arise at the same rate and with the same kinematics as uncorrelated OS pairs. If there are no other correlated pairs present, in principal only the $M_{\tau,\tau}$ spectrum from our signal decay chain should remain.

6.5.1 The SM contributions

Due to the serious lack of statistics in the remaining SM background the shape of the $M_{\tau,\tau}$ contributions from each SM process were obtained by slightly loosening the SUSY selection, and then this shape was normalised by the final statistics of the cut flow.

Contribution from $t\bar{t}$

Figure 6.7 shows the $M_{\tau,\tau}$ shape of the $t\bar{t}$ contribution after the OS-SS procedure. The shape with the complete SUSY selection, and that with the loosened SUSY selection are shown superimposed. For $t\bar{t}$ the SUSY selection was loosened as follows:

- $E_T^{miss} > 200\text{GeV} \rightarrow E_T^{miss} > 100\text{GeV}$
- $M_{eff} > 700\text{GeV} \rightarrow M_{eff} > 600\text{GeV}$

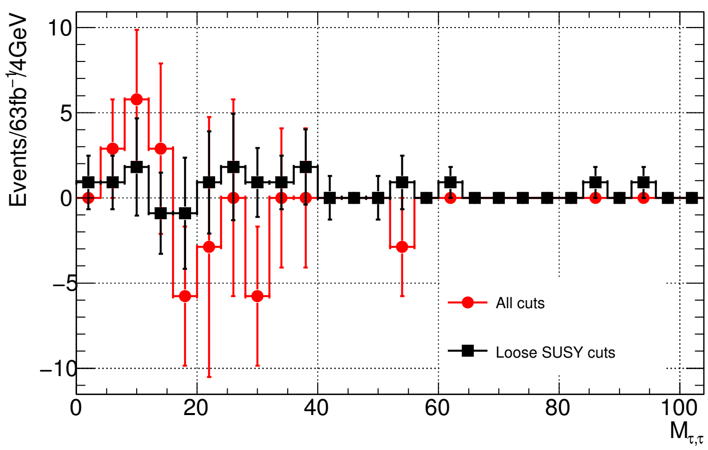

FIGURE 6.7: $t\bar{t}$ contribution to the $M_{\tau,\tau}$ spectrum. The red line shows the shape with all of the selection cuts imposed while the black line shows the shape with the loosened selection.

We can see that the contribution from $t\bar{t}$ after the loosened SUSY selection is not perfectly flat, due to the contribution from correlated leptons, arising from fully leptonic decay $t\bar{t}$ events. Most of the correlated pair are true/fake or fake/true combinations, where one of the pairs is an electron. There is a possibility that this excess is slightly underestimated with these looser cuts on E_T^{miss}, since fully leptonic $t\bar{t}$ decay is expected to be enhanced with hard E_T^{miss} cuts. The effect of any such increase on the final $M_{\tau,\tau}$ spectrum is expected to be negligible though, since the absolute contribution from $t\bar{t}$ is small compared to the SUSY combinatorial background.

Contribution from $W \rightarrow \tau, \nu$

Figure 6.8 shows the $M_{\tau,\tau}$ shape of the $W \rightarrow \tau, \nu$ contribution after the OS-SS procedure. The shape with the complete SUSY selection, and that with the loosened SUSY selection are shown superimposed. For $W \rightarrow \tau, \nu$ the SUSY selection was loosened as follows:

- $E_T^{miss} > 200\text{GeV} \rightarrow E_T^{miss} > 100\text{GeV}$
- $M_{eff} > 700\text{GeV} \rightarrow M_{eff} > 200\text{GeV}$
- $P_T^{jet1} > 180\text{GeV} \rightarrow P_T^{jet1} > 100\text{GeV}$
- $P_T^{jet2} > 90\text{GeV} \rightarrow P_T^{jet2} > 50\text{GeV}$
- $M_T > 90\text{GeV} \rightarrow M_T > 50\text{GeV}$

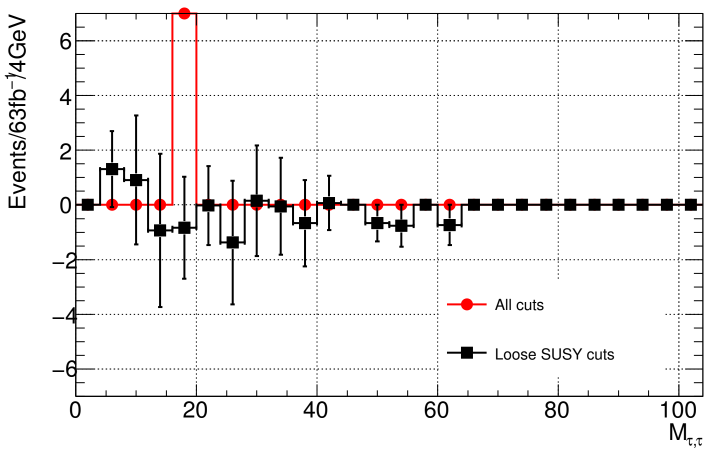

FIGURE 6.8: $W \rightarrow \tau, \nu$ contribution to the $M_{\tau,\tau}$ spectrum. The red line shows the shape with all of the selection cuts imposed while the black line shows the shape with the loosened selection.

The shape of the $W \rightarrow \tau, \nu$ $M_{\tau,\tau}$ contribution is flat as expected, since there should not be any correlated pairs, true tau or fake tau, in such events.

Contribution from $Z \rightarrow \nu, \nu$

It was found that $Z \rightarrow \tau, \tau$ became negligible compared to $Z \rightarrow \nu, \nu$ due to the large cuts on E_T^{miss}, thus only $Z \rightarrow \nu, \nu$ is considered for the $M_{\tau,\tau}$ shape contribution. Figure 6.9 shows the $M_{\tau,\tau}$ shape of the $Z \rightarrow \nu, \nu$ contribution after the OS-SS procedure. The shape with the complete SUSY selection, and that with the loosened SUSY selection are shown superimposed. For $Z \rightarrow \nu, \nu$ the SUSY selection was loosened as follows:

- $E_T^{miss} > 200\text{GeV} \rightarrow E_T^{miss} > 100\text{GeV}$

- $M_{eff} > 700\text{GeV} \rightarrow M_{eff} > 200\text{GeV}$
- $P_T^{jet1} > 180\text{GeV} \rightarrow P_T^{jet1} > 100\text{GeV}$
- $P_T^{jet2} > 90\text{GeV} \rightarrow P_T^{jet2} > 50\text{GeV}$
- $M_T > 90\text{GeV} \rightarrow M_T > 50\text{GeV}$

which is the same as for $W \rightarrow \tau, \nu$.

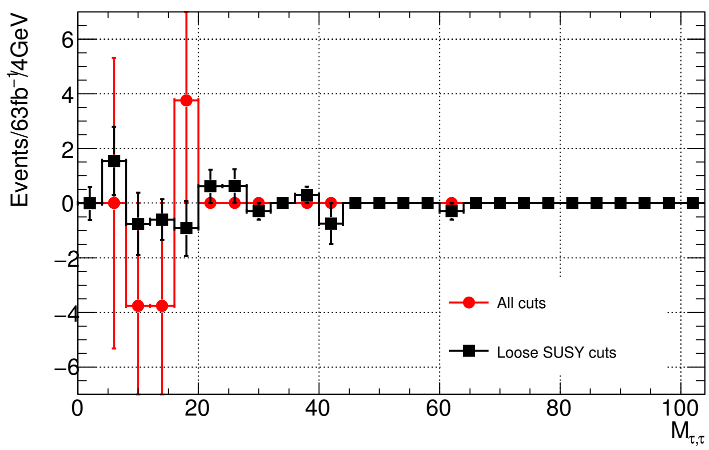

FIGURE 6.9: $Z \rightarrow \nu, \nu$ contribution to the $M_{\tau,\tau}$ spectrum. The red line shows the shape with all of the selection cuts imposed while the black line shows the shape with the loosened selection.

The shape of the $Z \rightarrow \nu, \nu$ $M_{\tau,\tau}$ contribution is flat as expected, since again there should not be any correlated pairs, true tau or fake tau, in such events.

6.5.2 The SUSY combinatorial background contribution

Table 6.4 shows the proportion of the main SUSY background processes which survive the selection procedure. Unfortunately correlation between true and fake tau combinations is much more prevalent in the SUSY background compared to the SM background, due to the other decay modes of the $\tilde{\chi}_2^0$ which produce opposite sign leptons, the possibility of correlated stop-top pairs from gluino decay which can go to opposite sign leptons, and from $\tilde{\chi}_1^{\pm}$ pair production.

Figure 6.10 shows the various contributions from the SUSY background to the $M_{\tau,\tau}$ spectrum. In order to maintain statistics only a lepton veto was applied for this plot [3] . We can see that the contribution from the misidentified golden decay chain is flat,

[3] The $M_{\tau,\tau}$ contribution from the SUSY background used in the final $M_{\tau,\tau}$ spectrum will be the one which results after all of the selection cuts. The loose selection used here is only to illustrate the contributions to the OS-SS excess coming from each individual SUSY background process.

Side 1	Side 2	Opposite sign	Same sign
All squarks	All squarks	34	24
$\tilde{\chi}_2^0 \to \tilde{\tau}_1 \to \tilde{\chi}_1^0$	Anything	67	62
$\tilde{\chi}_2^0 \to \tilde{\tau}_2 \to \tilde{\chi}_1^0$	Anything	21	8
$\tilde{\chi}_2^0 \to \tilde{e} \to \tilde{\chi}_1^0$	Anything	9	3
Contains $\tilde{\chi}_1^{\pm}$	Contains $\tilde{\chi}_1^{\pm}$	36	27
Contains $\tilde{\chi}_1^{\pm}$	All squarks	70	52
Other		18	20
TOTAL		255	196

TABLE 6.4: The breakdown of the SUSY background contribution.

albeit with a large statistical fluctuation in each bin. This fluctuation is due to the large statistical error arising from the OS-SS subtraction. We can see that there is a significant contribution from the process $\tilde{\chi}_2^0 \to \tilde{\tau}_2, \tau \to \tilde{\chi}_1^0, \tau, \tau$, which has a cross section a factor 8 smaller than the similar golden decay chain. The $M_{\tau,\tau}$ endpoint for this process is at 56GeV. The most significant contribution to the excess though comes from the processes with jets for which the above-mentioned contribution from correlated stop-top pairs is expected to dominate.

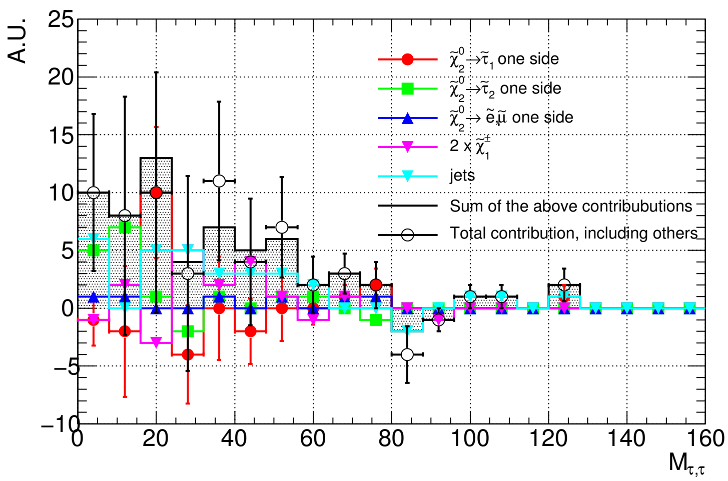

FIGURE 6.10: Contributions to the $M_{\tau,\tau}$ spectrum from the various processes in background SUSY events.

6.6 Final $M_{\tau,\tau}$ analysis

Finally each of the BG contributions are added to the signal to form the complete $M_{\tau,\tau}$ spectrum. Figure 6.11 shows the individual contributions from each process. We can see that by far the most significant background contribution comes from the SUSY combinatorial BG. This is due to both the large statistic which remain after the selection, and also the OS-SS excess which exists from the remaining SUSY processes. We can see that the signal dominates the background in the lower $M_{\tau,\tau}$ region, though it has comparable statistics to the background near the endpoint. For this analysis, the endpoint of the spectrum is found by a linear fit of the entire falling edge, so that the significance of the signal near the endpoint is not absolutely critical, though it will play a significant role.

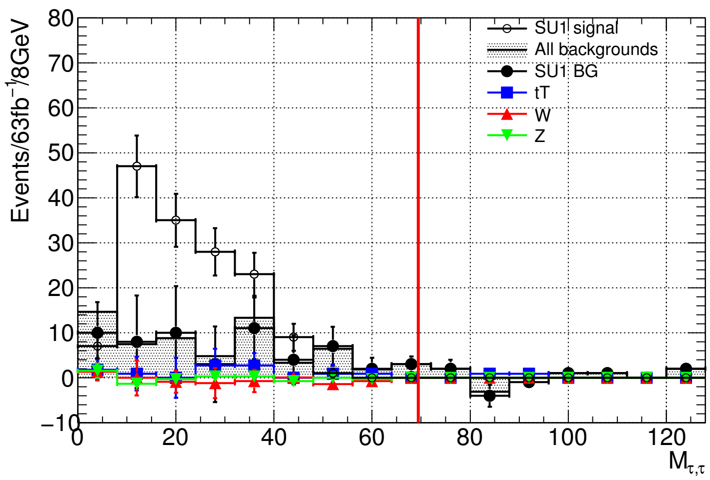

FIGURE 6.11: The contributions to the $M_{\tau,\tau}$ spectrum from the coannihilation signal, and each of the background processes.

Figure 6.12 show the combined $M_{\tau,\tau}$ spectrum which is fit by minimising the χ^2 of the fitting function with respect to the spectrum. The spectrum is fitted with the following function using the `MINUIT` package

$$f(x) = (x < -\frac{p_1}{p_0})(p_0 x + p_1) + (x > -\frac{p_1}{p_0}) \times 0 \tag{6.1}$$

where the inequality terms are logical booleans (equal to 0 or 1). The first summand defines a first degree polynomial which crosses the x-axis at $-p_1/p_0$, and only exists for $x < -p_1/p_0$, *i.e.* only below the x crossing. The second summand defines the function $f(x) = 0$, and only exists for $x > -p_1/p_0$, *i.e.* only above the x crossing. By fitting with this function we also take account of the $M_{\tau,\tau}$ spectrum above the x crossing of the linear function, and the point where the two pieces of the function join is the position of the $M_{\tau,\tau}$ endpoint $x = -p_1/p_0$.

The fit to this function in the region 8GeV $< M_{\tau,\tau} <$ 80GeV yields an $M_{\tau,\tau}$ endpoint of

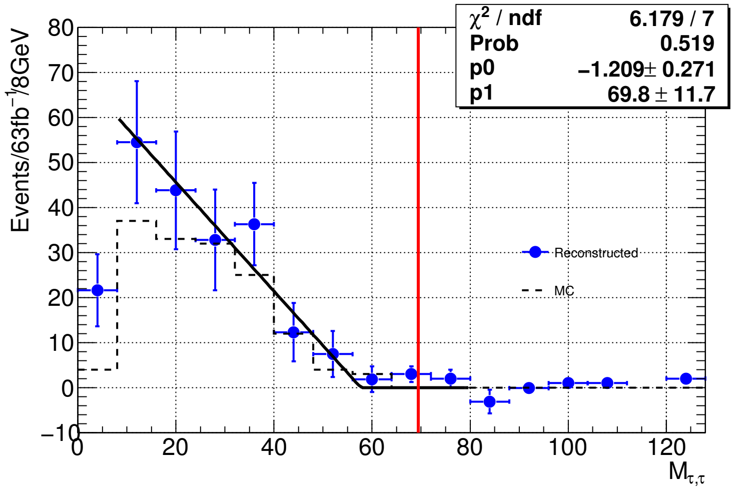

FIGURE 6.12: The fit of the final $M_{\tau,\tau}$ spectrum, with the function of Equation 6.1.

$$M_{\tau,\tau\,endpoint} = 58 \pm 16\,(\text{stat})\ \text{GeV} \tag{6.2}$$

with a minimised χ^2/d.o.f. of 6.2/7. This is consistent with the theoretical endpoint of 69 GeV.

The systematic studies of this fit, and studies of fitting with other functions will be discussed in the next chapter.

Chapter 7

Systematic Studies, Discussion and Outlook

In this chapter the systematic uncertainties of this $M_{\tau,\tau}$ endpoint analysis will be discussed, and an estimate of the systematic error in the final result will be made. Comparisons of the derived $M_{\tau,\tau}$ spectrum with the spectrum derived from an analysis using only `tauRec` will then be made. There will then be a discussion of attempts to fit the $M_{\tau,\tau}$ spectrum with a more sophisticated functional form. This will be followed by the application of the soft tau analysis to a different coannihilation SUSY point. Finally an outline of the possible future direction of this study will be given.

Here we note that a number of the plots for for this chapter have been relegated to Appendix C with only the results from the plots (fitting of the histograms etc.) shown within the actual chapter text.

7.1 Systematic studies

7.1.1 Systematic study of the linear fit

As a continuation of the fitting result of the previous chapter, this section will estimate the systematic uncertainty arising from the fit of the $M_{\tau,\tau}$ spectrum.

Table 7.1 shows the result of fitting the spectrum with the function of Equation 6.1, while varying the fit range, and the binning of the spectrum. The largest systematic effects on the reconstructed endpoint are $\approx^{+3.1\text{GeV}}_{-0.6\text{GeV}}$.

Range [GeV]	Endpoint [GeV]	$\chi^2/d.o.f.$
8 GeV bins		
8 - 80	57.7	6.3/7
16 - 80	57.6	6.4/6
24 - 80	57.1	6.3/5
8 - 72	57.7	5.4/6
8 - 64	57.7	2.4/5
4 GeV bins		
8 - 80	58.8	10.3/16
16 - 80	58.6	9.6/14
24 - 80	58.8	9.2/12
8 - 72	58.8	9.0/14
8 - 64	58.8	6.0/12
16 GeV bins		
16 - 80	60.8	3.7/2
16 - 64	60.8	0.15/1

TABLE 7.1: The variation in the result of the linear $M_{\tau,\tau}$ fit when the fit range and the binning are altered.

7.1.2 Systematic study of tau fake rate

Two of the significant systematic uncertainties arising from the Monte Carlo simulation are the fake rate from the hard tau selection and the fake rate from the soft tau selection. In order to estimate the effect of an increase in these fake rates on the $M_{\tau,\tau}$ endpoint derivation, both of these fake rates were increased in the simulation by hand.

Hard tau fake rate

The estimation of the fake rate arising from the likelihood cut in `tauRec` is dependant on the knowledge of the shower shapes of taus and jets in the calorimeter. There are inherent limitations to the accuracy of the simulation of such complex processes, and also inherent limitations to the basic knowledge of QCD jet production processes. For example Monte Carlo simulation pion showers are slightly narrower and shorter than the showers measured in calorimeter beam tests. A detailed study of the systematic error arising from such uncertainties may involve altering such things as the Monte Carlo simulation fragmentation parameters, but here we simply increase the tau fake rate by hand.

In order to study the effect that such an increase in the hard tau selection fake rate may have on the $M_{\tau,\tau}$ spectrum, the likelihood cut at which *fake* tau were allowed to "pass" was reduced. For the $M_{\tau,\tau}$ analysis the "medium" likelihood cut is used for discrimination. For this systematic study, fake taus were allowed to pass if they passed only the "loose" likelihood cut, while true taus were still required to pass the "medium" cut. This loosening increases the fake tau rate by a factor of $\approx 2-3$ in a QCD sample. This is a rather conservative estimate of the increase and the real fake rate is not expected to change to this extent from the simulation, once the detector is well understood.

The result of this procedure is a 30% increase in the background statistics from SUSY combinatorial processes, a 50% increase for $t\bar{t}$, no change for $W \rightarrow \tau, \nu$ (though the statistics are very limited) and a 50% increase for $Z \rightarrow \nu, \nu$.

Plots showing the contributions to the $M_{\tau,\tau}$ distribution from the signal and the various backgrounds, along with the final fit of the spectrum can be found in Appendix C, Figure C.1. The fit results in an endpoint of

$$M_{\tau,\tau\,endpoint} = 57 \pm 16\,\mathrm{GeV(stat)} \tag{7.1}$$

Soft tau fake rate

Again the estimation of the fake rate arising from the soft tau search algorithm likelihood cut is dependant on the knowledge of the shower shapes of taus and jets in the calorimeter. In order to study the effect that an increase in the soft tau selection fake rate may have on the $M_{\tau,\tau}$ spectrum, the $p_{T,track}$ and likelihood cuts of section Section 6.3 were de-optimised:

- $p_{T,track} > 2.5\mathrm{GeV} \rightarrow p_{T,track} > 2.0\mathrm{GeV}$
- $LLH > 0 \rightarrow LLH > -2$

The result of this procedure is a factor 1.3 increase in the background statistics from SUSY combinatorial processes, a factor 1.4 increase for $t\bar{t}$, a doubling of $W \rightarrow \tau, \nu$ (though the statistics are again very limited) and a factor 5.7 increase for $Z \rightarrow \nu, \nu$.

Plot showing the contributions to the $M_{\tau,\tau}$ distribution from the signal and the various backgrounds, along with the final fit of the spectrum can be found in Appendix C, Figure C.2. The fit results in an endpoint of

$$M_{\tau,\tau\,endpoint} = 54 \pm 17\,\mathrm{GeV(stat)} \tag{7.2}$$

Source	Recommended effect	$M_{\tau,\tau}$ endpoint [GeV]
Tau energy scale overestimation	$E \to 0.95E$	56.1
Tau energy scale underestimation	$E \to 1.05E$	56.8
Tau energy resolution overestimation	$E \to$ smear with $\sigma = 0.45\sqrt{E}$	56.9
Jet energy scale overestimation	$E \to 0.93E$ $(\lvert\eta\rvert < 3.2)$ $E \to 0.85E$ $(\lvert\eta\rvert > 3.2)$	61.9
Jet energy scale underestimation	$E \to 1.07E$ $(\lvert\eta\rvert < 3.2)$ $E \to 1.15E$ $(\lvert\eta\rvert > 3.2)$	55.9
Jet energy resolution overestimation	$E \to$ smear with $\sigma = 0.45\sqrt{E}$ $(\lvert\eta\rvert < 3.2)$ $E \to$ smear with $\sigma = 0.63\sqrt{E}$ $(\lvert\eta\rvert > 3.2)$	55.6

TABLE 7.2: Sources of energy scale systematic uncertainties and their effects on the $M_{\tau,\tau}$ endpoint determination.

We can see that, with these increases in the tau fake rate for both hard tau and the soft tau algorithms, the $M_{\tau,\tau}$ endpoint estimation changes by $\approx_{-4}$ at the most. This decrease is due to an increase in the statistics of the bins below the $M_{\tau,\tau}$ endpoint, which tends to increase the slope of the linear fit.

7.1.3 Systematic study of tau and jet energy scales

There are a number of systematic uncertainties in the tau and jet energy reconstruction in the Monte Carlo simulation that may affect the final result of the $M_{\tau,\tau}$ spectrum fit. One of the major uncertainties is the ability to correctly scale the hadronic contributions in taus and jets to the correct level. Furthermore, there are uncertainties arising from the accuracy of the estimations of dead material effects, transverse energy losses from the energy collection area, lateral energy loss from punch through, and losses from low energy tracks bending away from the calorimeter in the solenoid magnetic field. For this systematic study the recommendations from the 2008 ATLAS CSC study were followed. These systematic effects, and their results on the final $M_{\tau,\tau}$ endpoint determination are summarised in Table 7.2. The plots of the resulting contributions to the $M_{\tau,\tau}$ spectrum, and the final fits of the spectrum can be found in Appendix C. We note that the E_T^{miss} for each event has also been corrected for each systematic uncertainty.

We can see that the $M_{\tau,\tau}$ analysis is fairly robust against the systematic uncertainties in the tau and jet energy scales, with a maximum deviation in the endpoint determination of $\approx^{+4}_{-2}$.

For the total systematic uncertainty, the contributions from the above considerations were assumed to be independent, and each contribution is added in quadrature. The final estimation of the systematic uncertainty in the $M_{\tau,\tau}$ endpoint analysis is

$$\sigma_{systematic,total} =^{+5}_{-5} \text{GeV} \tag{7.3}$$

and the final result of the $M_{\tau,\tau}$ spectrum endpoint becomes

$$M_{\tau,\tau\,endpoint} = 58 \pm 16\ (\text{stat})\ \pm 5\ (\text{sys})\text{GeV} \tag{7.4}$$

We note that these systematics errors will be reduced when the Monte Carlo shower shapes and energy calibrations are validated using real data.

7.2 Comparison of soft tau search method with other methods

7.2.1 Comparison with `tauRec`

In Section 5.2 a comparison between the performance of the soft tau likelihood method, and the `tauRec` likelihood method was presented. It was shown that the overall performance of the soft tau likelihood method for reconstructing the signal soft tau, was superior to that of the `tauRec` likelihood method, when an appropriate cut was made on the seed track p_T. For the final $M_{\tau,\tau}$ analysis though, the p_T cut of the soft tau search method was reduced to $p_{T,track} > 2.5$GeV in order to optimise the signal soft tau signal to background ratio. We would then like to check how the soft tau search method $M_{\tau,\tau}$ spectrum with this lower p_T cut compares with the $M_{\tau,\tau}$ spectrum obtained using `tauRec` to reconstruct the signal soft tau.

Since the seed thresholds for the `tauRec` algorithm are much higher than that of the soft tau search algorithm ($p_{T,track} > 6$GeV and $E_{T,topojet} > 10$GeV), the numbers of both signal and background surviving the above SUSY selection, *and* a `tauRec` soft tau selection, are very small. Because the absolute level of the background decreases with the `tauRec` thresholds, looser SUSY cuts are possible for the `tauRec` method. Thus only the following cuts were made for the `tauRec` SUSY selection [1]:

1. $P_T^{jet1} > 100\text{GeV}$
2. $P_T^{jet2} > 50\text{GeV}$
3. $E_T^{miss} > 100\text{GeV}$
4. $M_{eff} > 400\text{GeV}$
5. Exactly 2 `tauRec` objects with the same identification cuts as Table 6.1, except no p_T cut is imposed on either. $\Delta R_{\tau,\tau}$ is required to be less than 2.

Unfortunately these cuts fall below the generator filter cuts used to create a number of the SM backgrounds, so inclusion of the SM backgrounds would not be meaningful. Thus only the SUSY combinatorial background is included. Figure 7.1 shows the contributions to the $M_{\tau,\tau}$ spectrum using this method.

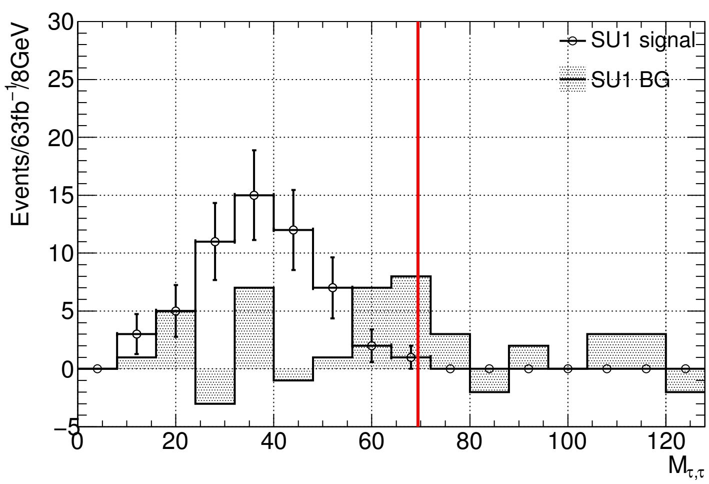

FIGURE 7.1: The contributions to the $M_{\tau,\tau}$ spectrum from the coannihilation signal and the SUSY background when `tauRec` is used for both taus' selections.

There are a couple of differences between this spectrum and the spectrum of the soft tau analysis to note. The first is that the signal $M_{\tau,\tau}$ distribution exhibits higher values than for the soft tau method. This is a result of a couple of effects. The first is that `tauRec` reconstruction includes π^0 energy in the calculation, which results in a better quality signal soft tau reconstruction and higher $M_{\tau,\tau}$ values. The second is the relatively high `tauRec` seed thresholds imposing a bias on the signal soft tau. For similar reasons the

[1]These are very similar cuts to those used in the $M_{\tau,\tau}$ study of the 2008 ATLAS CSC note [21]. This was a study performed at a collision energy of 14TeV

SUSY background spectrum is located at higher values of $M_{\tau,\tau}$ also. This results in more background being located near to the theoretical $M_{\tau,\tau}$ endpoint. We can see that indeed the background dominates around the theoretical endpoint. It is obvious from this level of background near the endpoint, that the endpoint determination of the soft tau selection method is superior to that using only `tauRec`, when, for the latter, the events are selected in the way described above.

7.2.2 Comparisons with simple geometric methods

Now in order to observe the effect of the soft tau search likelihood selection on the $M_{\tau,\tau}$ spectrum, we compare our result with two simple geometric methods for selecting the soft tau. For these methods, exactly the same procedure is followed as for the soft tau search method, except that rather than applying the likelihood cut and selecting the most tau-like candidate, we simply

1. Choose the closest soft tau candidate to the hard tau candidate in the soft tau search cone OR
2. Choose the hardest soft tau candidate in the soft tau search cone.

Figure 7.2 shows the individual contributions to the $M_{\tau,\tau}$ spectrum arising from these methods. Comparing with Figure 6.11 we can see that although the relative level of OS-SS excess in the background is similar to the soft tau likelihood method, the statistical fluctuation arising in each bin from the OS-SS method is greater. This is because, for these simple geometric methods, *every* hard tau candidate is paired with a soft tau candidate. Table 7.3 compares the signal and background statistics which remain for each of the methods for an integrated luminosity of 63 fb^{-1}. The final column shows the value of $S/\sqrt{N}$, where S is the number of signal events for which the signal hard and soft taus have been correctly selected by their respective algorithms, and N is the total number of events which remain with both a hard and soft tau candidate. As described in Section 6.3, this parameter gives an estimate of the level of the signal above the statistical fluctuation when the OS-SS is used. We can see that the soft tau likelihood method gives a higher value of $S/\sqrt{N}$ due to the fact that it rejects a large proportion of the fake soft tau candidates.

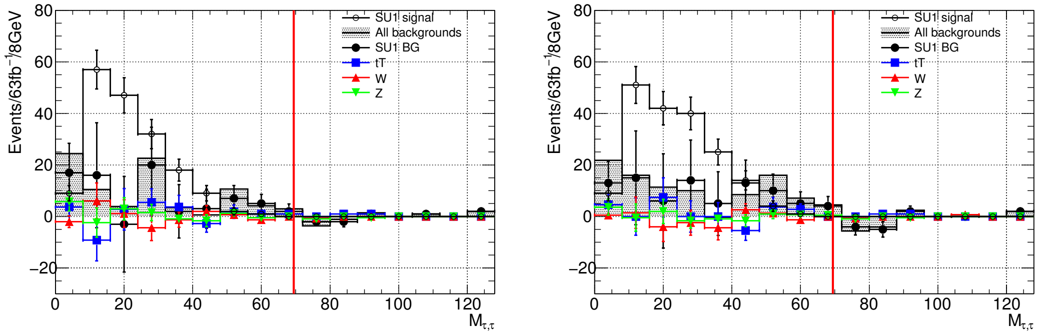

FIGURE 7.2: Left: The contributions to the $M_{\tau,\tau}$ spectrum from the coannihilation signal, and each of the background processes when the "closest candidate" method is used for the soft tau selection. Right: The contributions to the $M_{\tau,\tau}$ spectrum when the "hardest candidate" method is used for the soft tau selection.

Method	Signal	BACKGROUND				$S/\sqrt{N}$
		SUSY	$t\bar{t}$	W	Z	
Likelihood	150 ± 12	451 ± 21	75 ± 17	54 ± 54	19 ± 8	5.48 ± 0.57
Closest	175 ± 13	1327 ± 36	248 ± 27	161 ± 93	122 ± 22	3.88 ± 0.09
Hardest	186 ± 14	1316 ± 36	248 ± 27	161 ± 93	122 ± 22	4.13 ± 0.10

TABLE 7.3: Comparison of the statistics remaining after all cuts for the signal and each BG, and the level of the signal above the statistical fluctuation after all cuts and the OS-SS subtraction, when using the soft tau likelihood selection method, the "closest candidate" method and the "hardest candidate" method. Statistics are normalised to 63 fb^{-1}.

7.3 Analysis of a different coannihilation point

As another check of the robustness of this method it was applied to a coannihilation region sample with slightly different parameters.

- $m_0 = 50\text{GeV}$
- $m_{1/2} = 225\text{GeV}$
- $\tan\beta = 10$ (7.5)
- $A = 0$
- $\mu > 0$

Only m_0 and $m_{1/2}$ are reduced making it a lighter mass SUSY sample. It should be noted that while this sample is in the coannihilation region, it is actually excluded by the limit on the Higgs mass. The sample used corresponds to an integrated luminosity of 5.7fb^{-1}. The theoretical endpoint for this SUSY point is 58GeV.

The left hand plot of Figure 7.3 shows the individual contributions to the $M_{\tau,\tau}$ spectrum from the signal and various backgrounds. The right hand plot shows the fit using Equation 6.1. The result is

$$M_{\tau,\tau\, endpoint} = 42 \pm 11\,\mathrm{GeV(stat)} \tag{7.6}$$

which is agreement with the theoretical value of 58GeV. The $\chi^2/d.o.f.$ is 16.5/7.

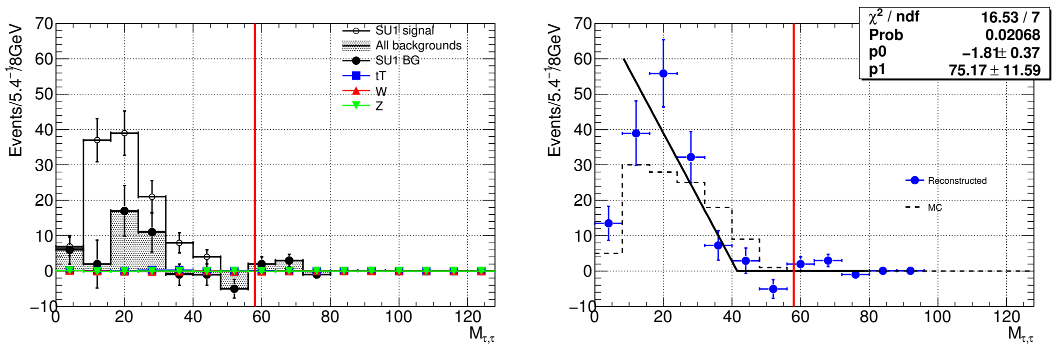

FIGURE 7.3: Left: The contributions to the $M_{\tau,\tau}$ spectrum from the lighter mass point coannihilation signal, and each of the background processes. Right: The fit of this $M_{\tau,\tau}$ spectrum, with the function of Equation 6.1.

7.4 Discussion of the form of the $M_{\tau,\tau}$ spectrum fitting function

As can be seen from the truth level $M_{\tau,\tau}$ distribution in Figure 3.5 the functional form of the falling edge of the $M_{\tau,\tau}$ spectrum is not exactly linear. A linear function is only a first approximation of the shape. In fact the high end of the truth spectrum tails off very slowly which makes the accurate determination of the endpoint very difficult, and an *accurate* estimation of the endpoint with a linear function virtually impossible. The underestimation of the endpoint using the linear function is evidence that this high end tail is not being accounted for in the linear fit.

In order to attempt to take account of the gradual high end tail of the spectrum it was attempted to fit it with the following function

$$f(x) = C \exp\left(\frac{(x - x_0)^2}{2\sigma^2}\right) + (p_0 x + p_1) \tag{7.7}$$

which is simply the sum of a gaussian and a linear function, with the linear function forcing the gaussian to cross the x axis. Again the crossing of the x axis of this function is to be identified with the $M_{\tau,\tau}$ endpoint.

Figure 7.4 shows the result of this fit with the slope of the linear part of the function constrained to be less than -0.3. It is interesting to see how the gaussian part of the function takes account of the $M_{\tau,\tau}$ tail. Unfortunately the fit does not behave as desired unless the slope of the linear part of the function is constrained to be less than zero (unless this slope is less than zero the function will not cross the x axis in the way that is desired). The slope of the linear part of the fit always settles at the maximum allowed slope. Thus this fitting procedure was not deemed to be robust, and the simple linear function of Equation 6.1 was settled for.

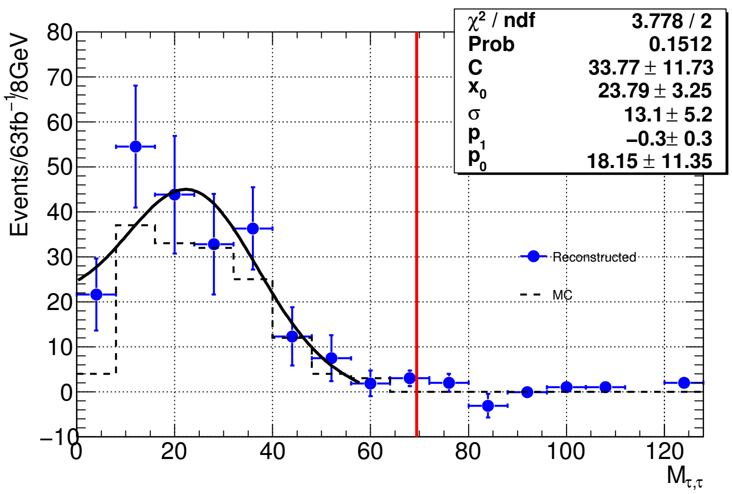

FIGURE 7.4: The fit of the final $M_{\tau,\tau}$ distribution with a gaussian + linear function.

7.5 Outlook

Here we discuss two possible extensions to this study. The first is the use of a different endpoint determination method. The second is the possible improvement from including soft tau π^0 energy in the $M_{\tau,\tau}$ distribution.

7.5.1 A new endpoint determination method

As discussed in the previous section the linear function that has been used to fit the edge of the $M_{\tau,\tau}$ spectrum is only a first approximation and does not take account of the gradual tail of the actual spectrum. In [21] the $M_{\tau,\tau}$ spectrum is fit with a so-called "log-normal" function which is of the form

$$f(x) = \frac{p_0}{x} \exp\left(-\frac{1}{2p_2^2}(\ln(x) - p_1)^2\right) \tag{7.8}$$

The fit of the log-normal function to $M_{\tau,\tau}$ spectrum is shown in Figure 7.5. We can see that the tail structure of the spectrum is much better described with this function compared to the simple linear fit. This function does not explicitly contain the $M_{\tau,\tau}$ endpoint but approaches the x axis asymptotically. Thus the endpoint must be found by a calibration procedure where the correlation between the inflection point of the function

$$m_{IP} = \exp\left(-\frac{1}{2}p_2^2\left(3 - \sqrt{1 + \frac{4}{p_2^2}}\right) + p_1\right) \tag{7.9}$$

and the theoretical endpoint is used.

This method then requires that samples for a number of different points in the coannihilation region are created, in order for the correlation to be determined. For the study mentioned above, ATLFAST was used to create these samples. Unfortunately for this study, more detailed calorimeter information is required (ESD level) and so the CPU time necessary is rather large. It is planned that full simulation of some number of points will be made, and a similar calibration procedure used to determine the endpoint more accurately.

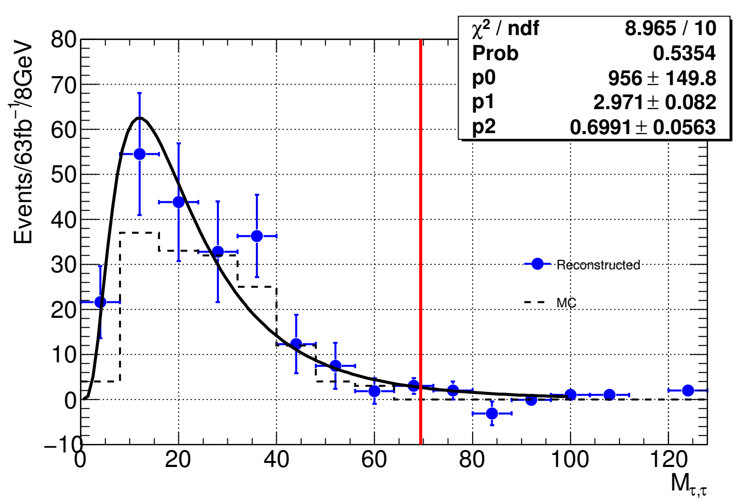

FIGURE 7.5: The fit of the final $M_{\tau,\tau}$ distribution with a log-normal function.

7.5.2 Including the signal soft tau π^0 information in the $M_{\tau,\tau}$ distribution

For this study, the final $M_{\tau,\tau}$ distribution was created using only the $\pi^\pm$ component of the signal soft tau. Thus any π^0 information is not included which will degrade the endpoint of the $M_{\tau,\tau}$ distribution. There are a number of reasons why inclusion of π^0 information was found to be difficult. The first and most immediately obvious reason is that the discrimination of π^0 clusters around the $\pi^\pm$ track is very difficult, as can be seen by the rather poor performance of the decay mode classification algorithm (see Table 5.3). As mentioned previously, at these small energies the $\pi^\pm$ energy tends to be split amongst a number of small clusters in the calorimeter and a number of these look like, and can be misidentified as, EM-like clusters. Also π^0 clusters often overlap $\pi^\pm$ clusters, making their discrimination difficult. Thus a simple addition of π^0 clusters to the $\pi^\pm$ track will not be sufficient to correctly recover the π^0 energy.

Another approach is to use a method similar to the ones used in `tauRec`. The first one that we consider is the `tauRec` track seed algorithm energy-flow method, which was described in Section 4.2.7.2. This method attempts to subtract the $\pi^\pm$ energy from the calorimeter, and then add the neutral calorimeter components to the track energy. We saw in Figure 4.3 that, at low tau energies, there is the danger of double counting and event contamination, which leads to an overestimation of the tau energy. This may result in a systematic overestimation of the $M_{\tau,\tau}$ endpoint so care would have to be taken.

The second `tauRec` energy reconstruction method to consider is the calorimeter seed algorithm method (again, refer Section 4.2.7.2). This simply adds the calorimeter energy in a cone around some seed, and corrects it to the hadronic scale. Again we can see from Figure 4.3 that at low energies the tau energy is overestimated, likely due to event contamination. Thus we would again need to be careful not to end up with a systematic overestimation of the $M_{\tau,\tau}$ endpoint, especially since the soft tau is often very close to the hard tau.

For reference Figure 7.6 shows the difference in the $M_{\tau,\tau}$ distribution when the π^0 energy is included in the calculation at the truth level. For this plot only the single prong modes of the signal soft tau are included, and a $p_{T,track} > 2.5$GeV cut is applied to the $\pi^\pm$ track. This cut means that the same bias towards lower multiplicity π^0 modes exists as for this study (see Table 5.2). We can see that the quality of the endpoint is certainly significantly improved if the π^0 information is included. Whether or not this information can be correctly included at the reconstruction level is a matter for further study.

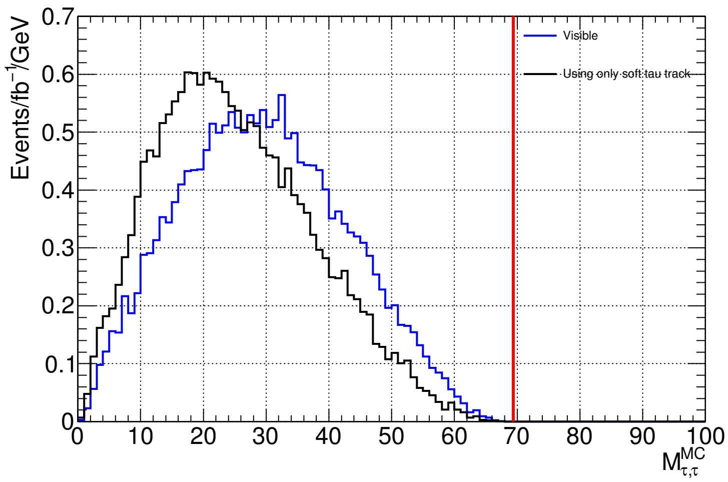

FIGURE 7.6: The truth level $M_{\tau,\tau}$ distribution for the case that only the signal soft tau single prong modes are considered. The blue line shows the visible distribution. The black line shows the distribution when only the $\pi^{\pm}$ component of the signal soft tau is used. A $p_{T,track} > 2.5$GeV cut is imposed on the signal soft tau $\pi^{\pm}$.

Chapter 8

Conclusion

The LHC detector has recently come online and high energy collisions have been successfully achieved. It is expected that the coming years of LHC data will reveal extensions to the SM of particle physics which are assumed necessary to explain a number its anomalies. One of the most promising theoretical extensions to the SM is supersymmetry, and in particular the mSUGRA model. The allowed phase space of this model is severely constrained by a number of experimental measurements. One of the open regions of the phase space is the so-called coannihilation region, which can explain the observed density of dark matter in the universe. The masses of the LSP ($\tilde{\chi}_1^0$) and the NLSP ($\tilde{\tau}_1$) are near degenerate in this region, which allows for their efficient coannihilation in the early universe. Such coannihilation results in a density of the LSP which is consistent with current dark matter density measurements.

In order to confirm the validity of the mSUGRA model and to check whether the coannihilation region is the region of the phase space which correctly describes the universe, exclusive measurements of particular decay chains must be performed. The ATLAS detector at the LHC is expected to be able to perform such measurements, and in this thesis we study its capability to measure the signal above the vast background using Monte Carlo simulations. The signal which is studied arises from the so-called coannihilation region "golden" decay chain:

$$\tilde{q} \rightarrow q\tilde{\chi}_2^0 \rightarrow q\tau\tilde{\tau}_1 \rightarrow q\tau\tau\tilde{\chi}_1^0 \tag{8.1}$$

where in this study we focus on measuring the endpoint of the $M_{\tau,\tau}$ distribution. The measurement of this endpoint, along with other invariant mass distribution endpoints arising from this decay chain, allow for the calculation of the masses of the sparticles in the chain.

Standard methods of reconstructing the $M_{\tau,\tau}$ endpoint require that each event has two well reconstructed taus. Unfortunately for the coannihilation region the second tau of the decay chain is particularly soft due to the near degenerate mass of the $\tilde{\chi}_1^0$ and the $\tilde{\tau}_1$. As a result the standard ATLAS reconstruction algorithm does not reconstruct the soft tau very efficiently due to its relatively high seed thresholds and stringent identification requirements.

In light of this we have developed a new method for tagging this soft tau. We have implemented a number of optimisations for reconstructing taus in the low energy region, and some novel analysis specific techniques. For example we exploit the separation of the low-boost tau decay products in the calorimeter for identification, and take account of the contamination from the other harder tau when calculating the soft tau likelihood variables.

We have shown that this method has a better performance than the standard ATLAS tau reconstruction algorithm for reconstructing the soft tau. We have also shown that using this method in conjunction with the ATLAS algorithm has a superior performance for reconstructing the $M_{\tau,\tau}$ endpoint of the decay chain, compared to using the ATLAS algorithm for reconstructing both taus. We obtain a final result of

$$M_{\tau,\tau\, endpoint} = 58 \pm 16\,(\text{stat})\ \pm 5\,(\text{sys})\ \text{GeV} \tag{8.2}$$

at the ATLAS coannihilation reference point with $E_{CM} = 10$TeV and an integrated luminosity of 63 fb^{-1}.

Appendix A

Plots of `tauRec` discrimination variables

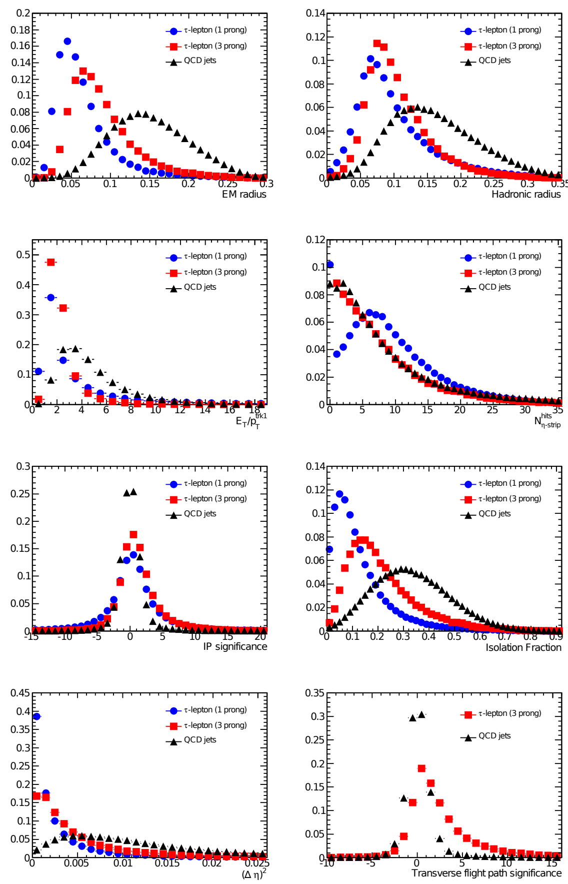

FIGURE A.1: The distributions of `tauRec` discrimination variables for the calorimeter seeded algorithm for the process $W \rightarrow \tau, \nu$, and for J2 background, as referred to in section 4.2.7.3. Distributions for 1-prong and 3prong taus are shown separately. [22]

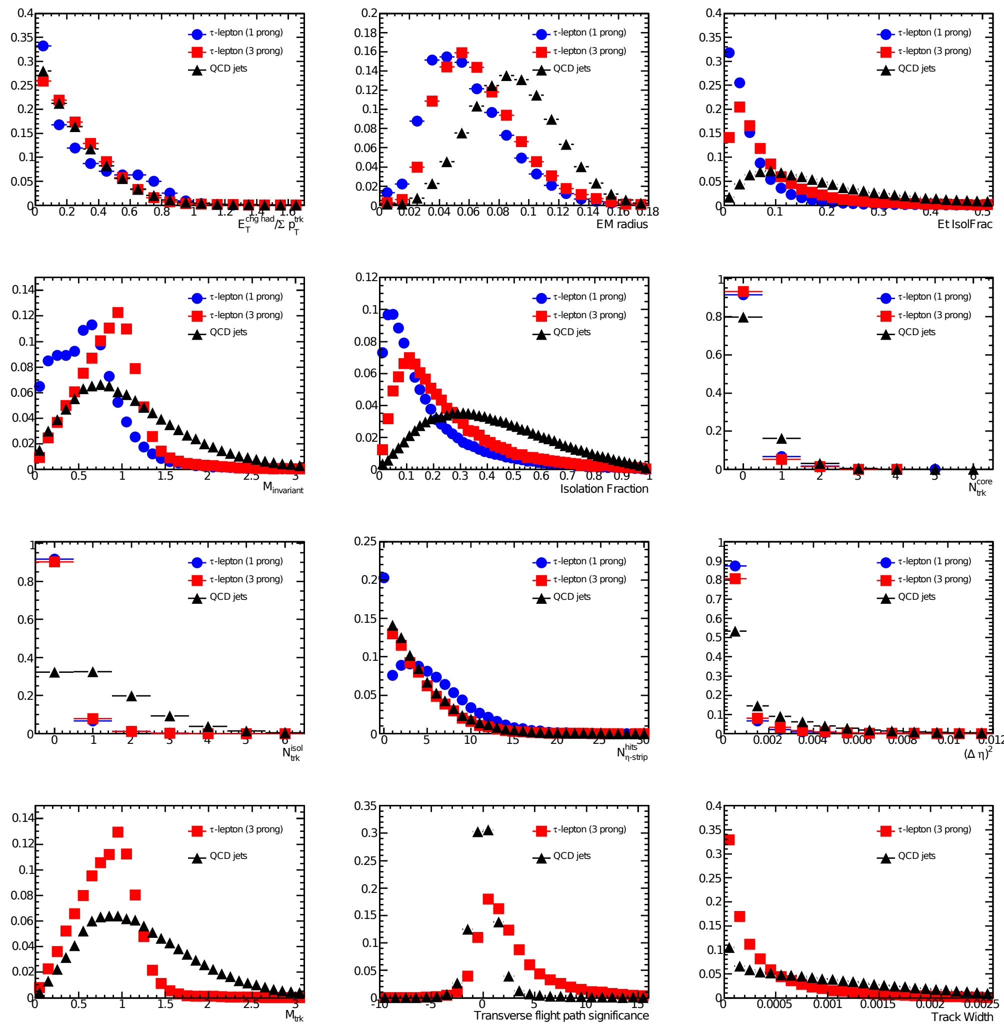

FIGURE A.2: The distributions of `tauRec` discrimination variables for the track seeded algorithm for the process $W \to \tau, \nu$, and for J2 background, as referred to in section 4.2.7.3. Distributions for 1-prong and 3prong taus are shown separately. [22]

Appendix B

Plots of PDFs used for the soft tau likelihood method

The plots in this appendix show the PDFs used for the soft tau likelihood method of Section 5.2. They are divided by decay mode classification (single prong 0-π^0, 1-π^0, and 2-π^0), and then further divided by the seed track momentum range (2GeV $< p_{track} <$ 5GeV, 5GeV $< p_{track} <$ 10GeV and $p_{track} >$ 10GeV).

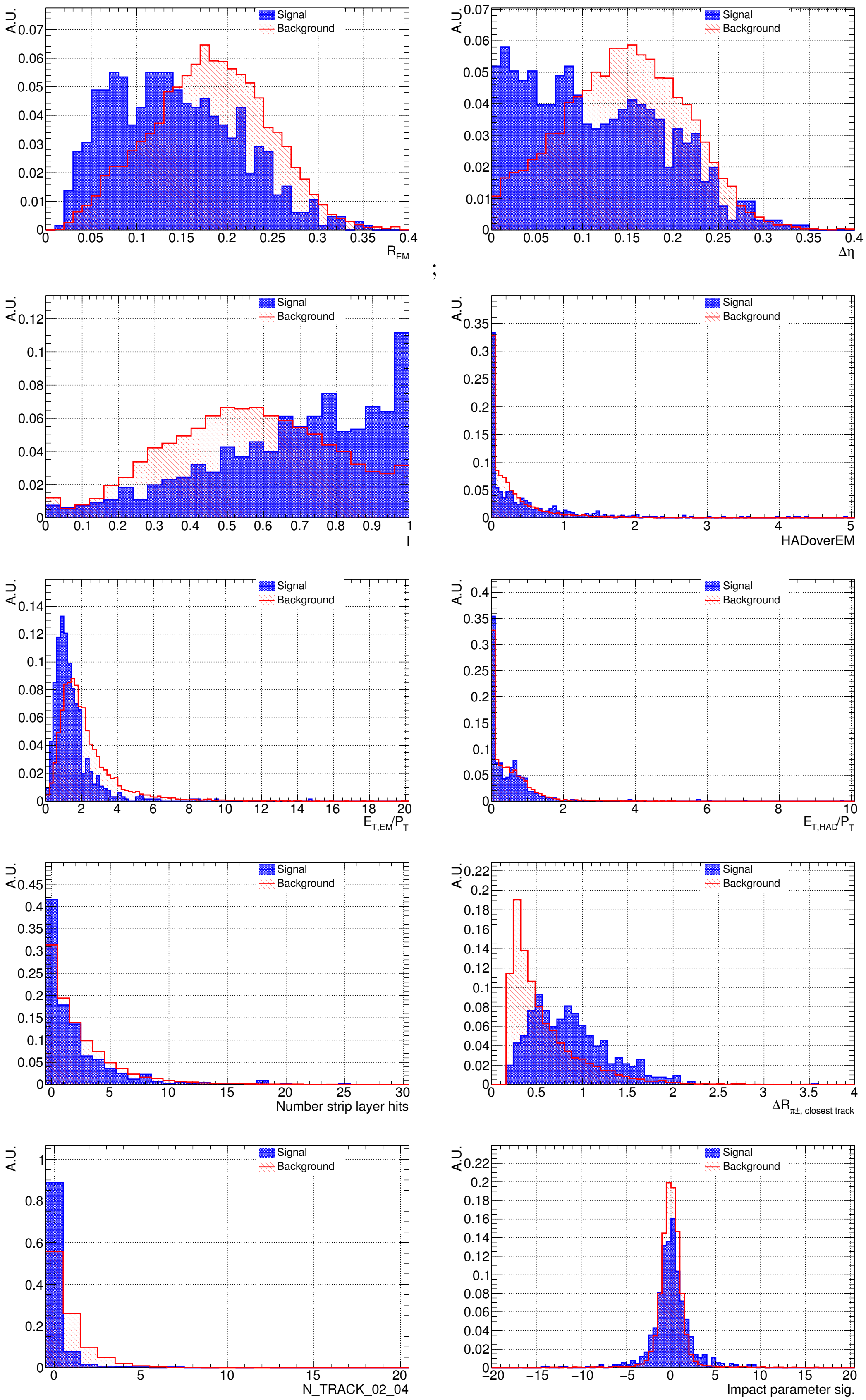

FIGURE B.1: The PDFs used to form the soft tau algorithm likelihood, for the 0-π^0 mode, when the seed track is in the range 2GeV $< p_{track} <$ 5GeV.

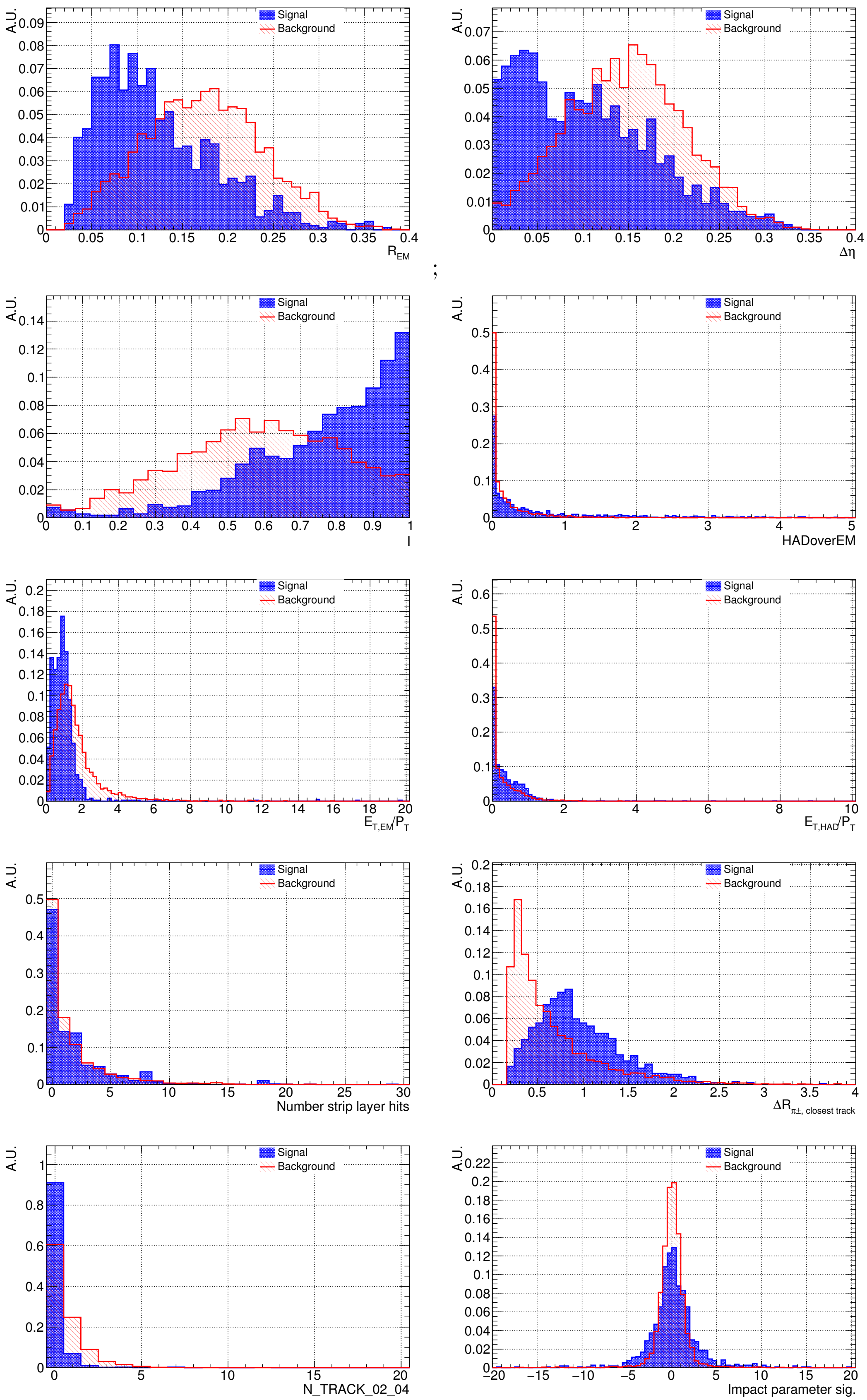

FIGURE B.2: The PDFs used to form the soft tau algorithm likelihood, for the 0-π^0 mode, when the seed track is in the range 5GeV < p_{track} < 10GeV.

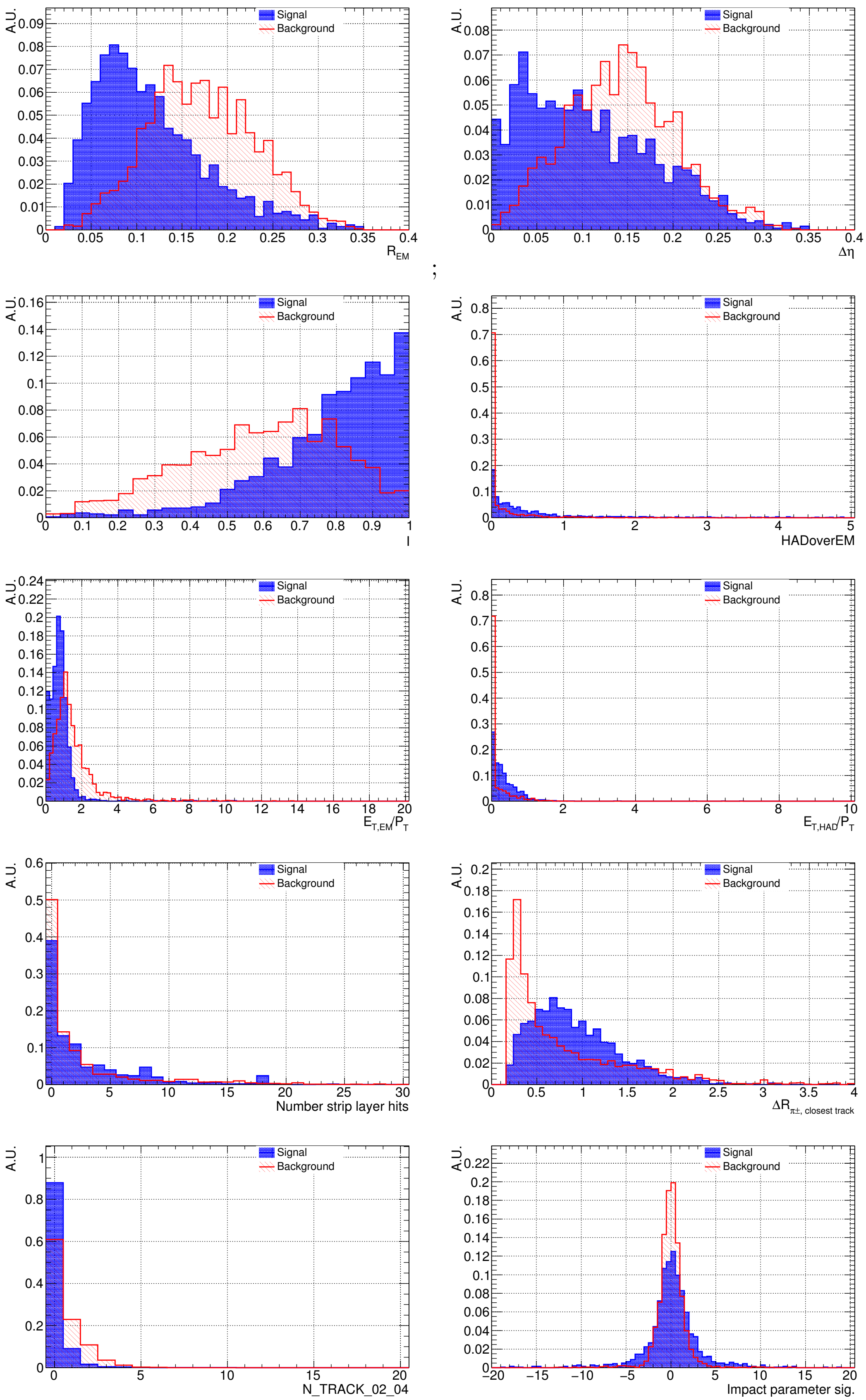

FIGURE B.3: The PDFs used to form the soft tau algorithm likelihood, for the 0-π^0 mode, when the seed track is in the range $p_{track} > 20$GeV.

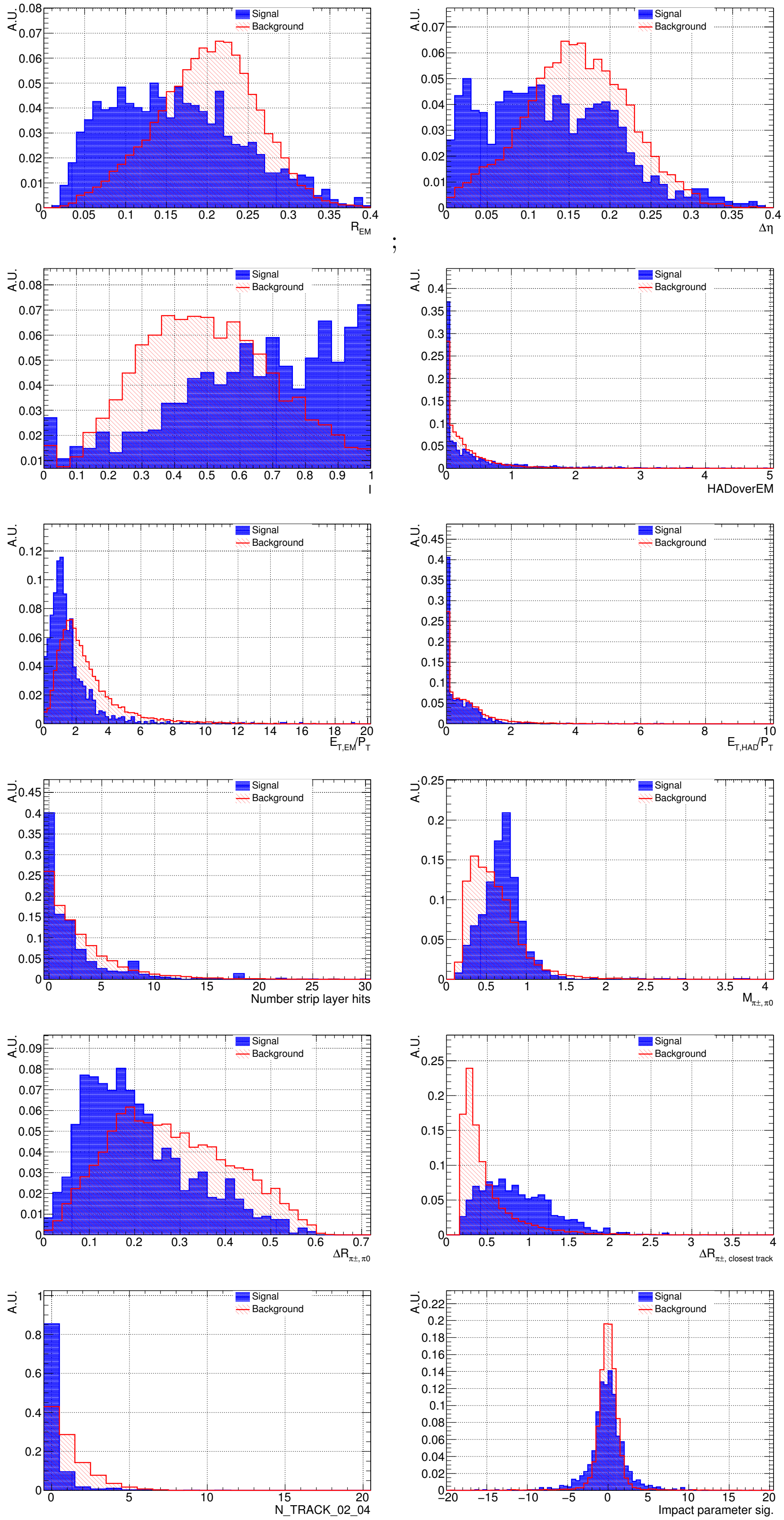

FIGURE B.4: The PDFs used to form the soft tau algorithm likelihood, for the 1-π^0 mode, when the seed track is in the range 2GeV $< p_{track} <$ 5GeV.

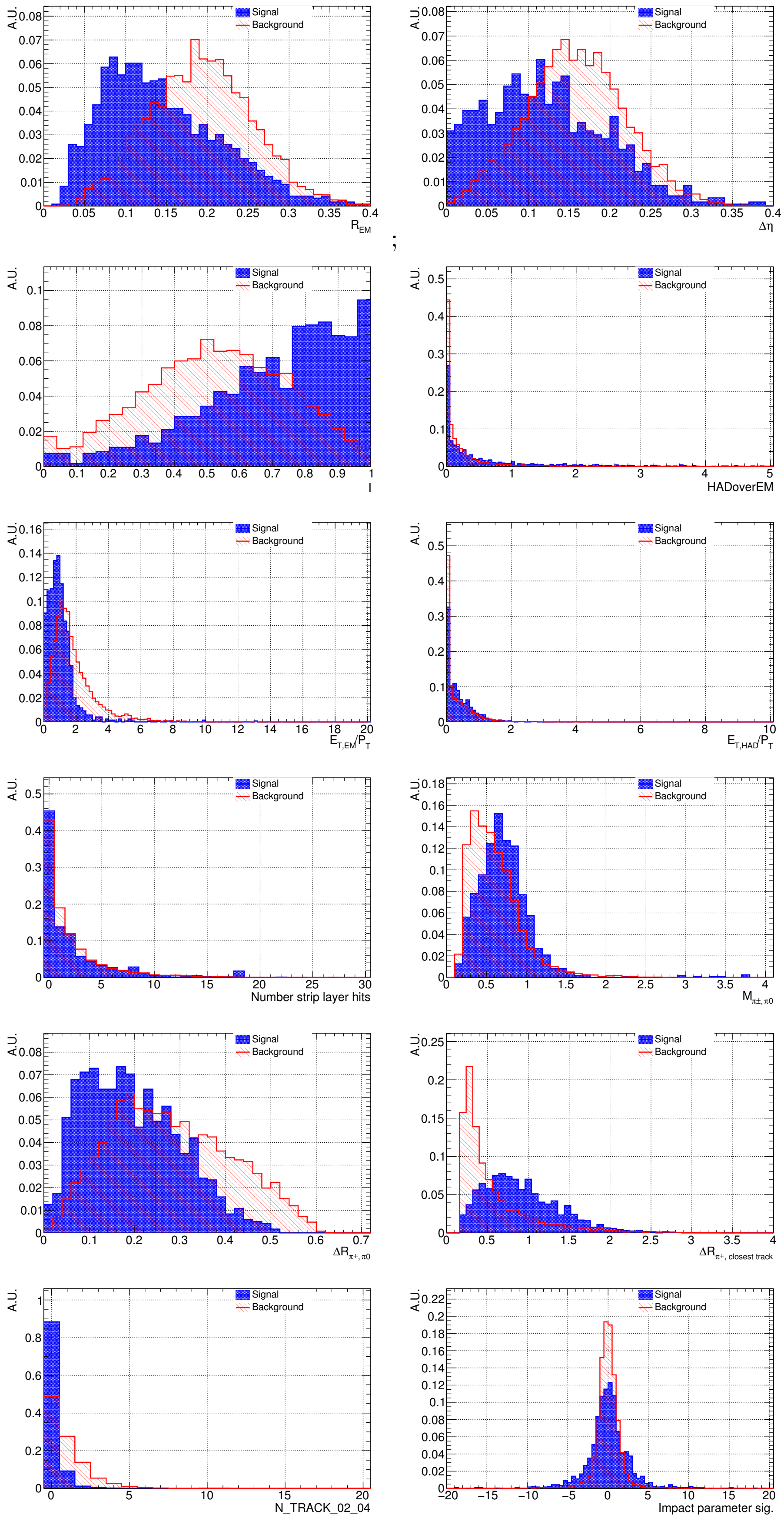

FIGURE B.5: The PDFs used to form the soft tau algorithm likelihood, for the 1-π^0 mode, when the seed track is in the range 5GeV $< p_{track} <$ 10GeV.

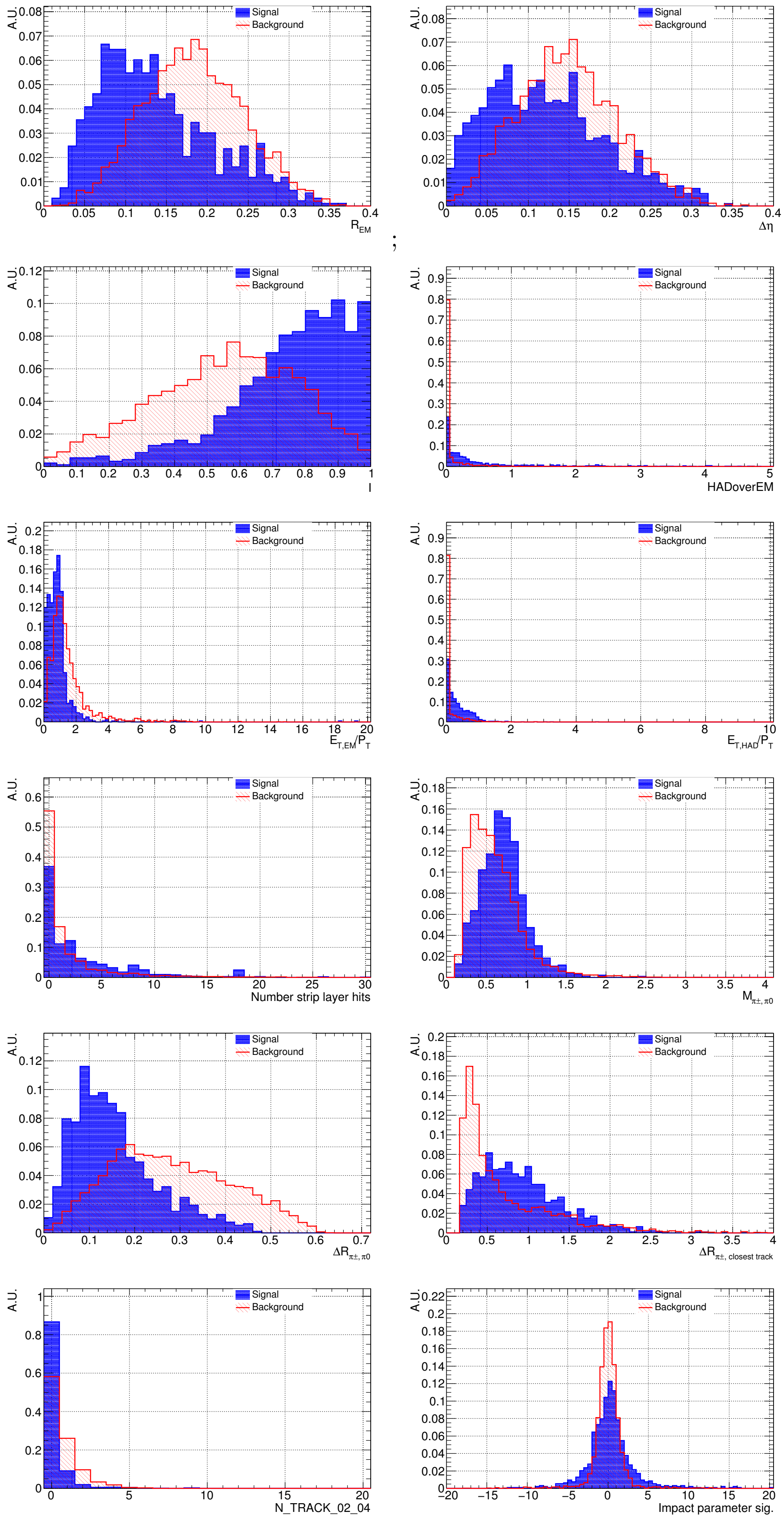

FIGURE B.6: The PDFs used to form the soft tau algorithm likelihood, for the 1-π^0 mode, when the seed track is in the range $p_{track} > 20$GeV.

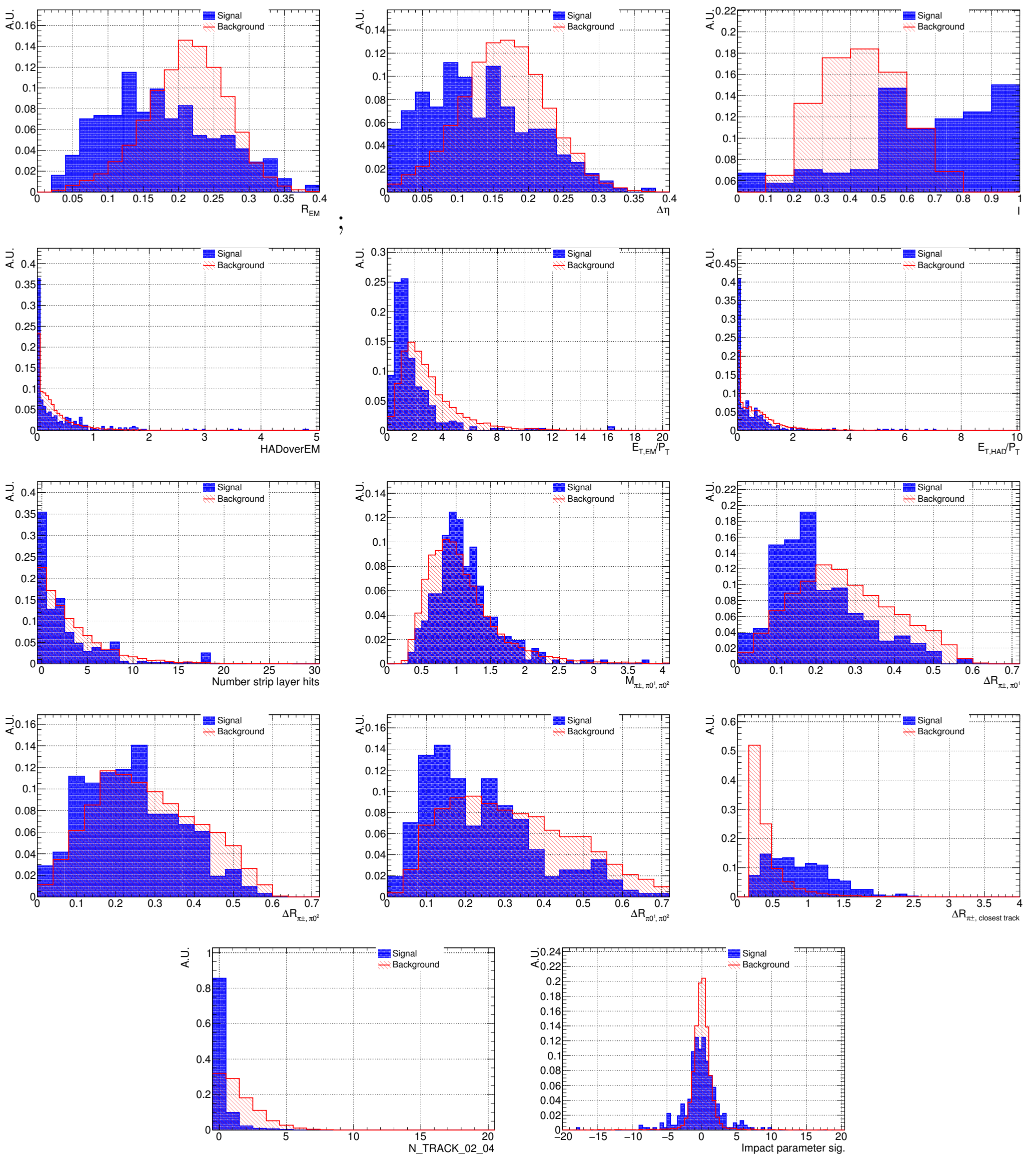

FIGURE B.7: The PDFs used to form the soft tau algorithm likelihood, for the 2-π^0 mode, when the seed track is in the range 2GeV $< p_{track} <$ 5GeV.

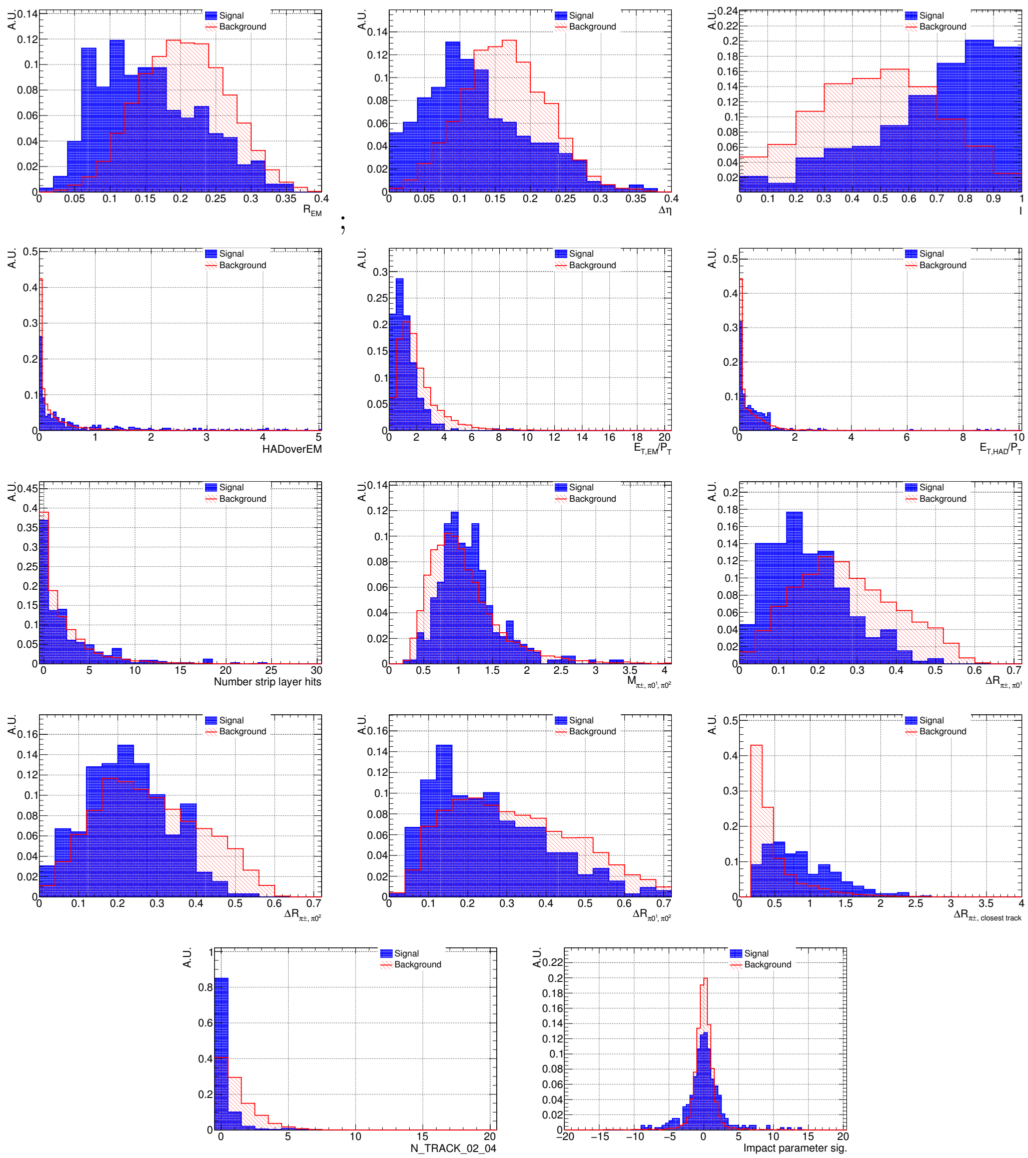

FIGURE B.8: The PDFs used to form the soft tau algorithm likelihood, for the 2-π^0 mode, when the seed track is in the range 5GeV $< p_{track} <$ 10GeV.

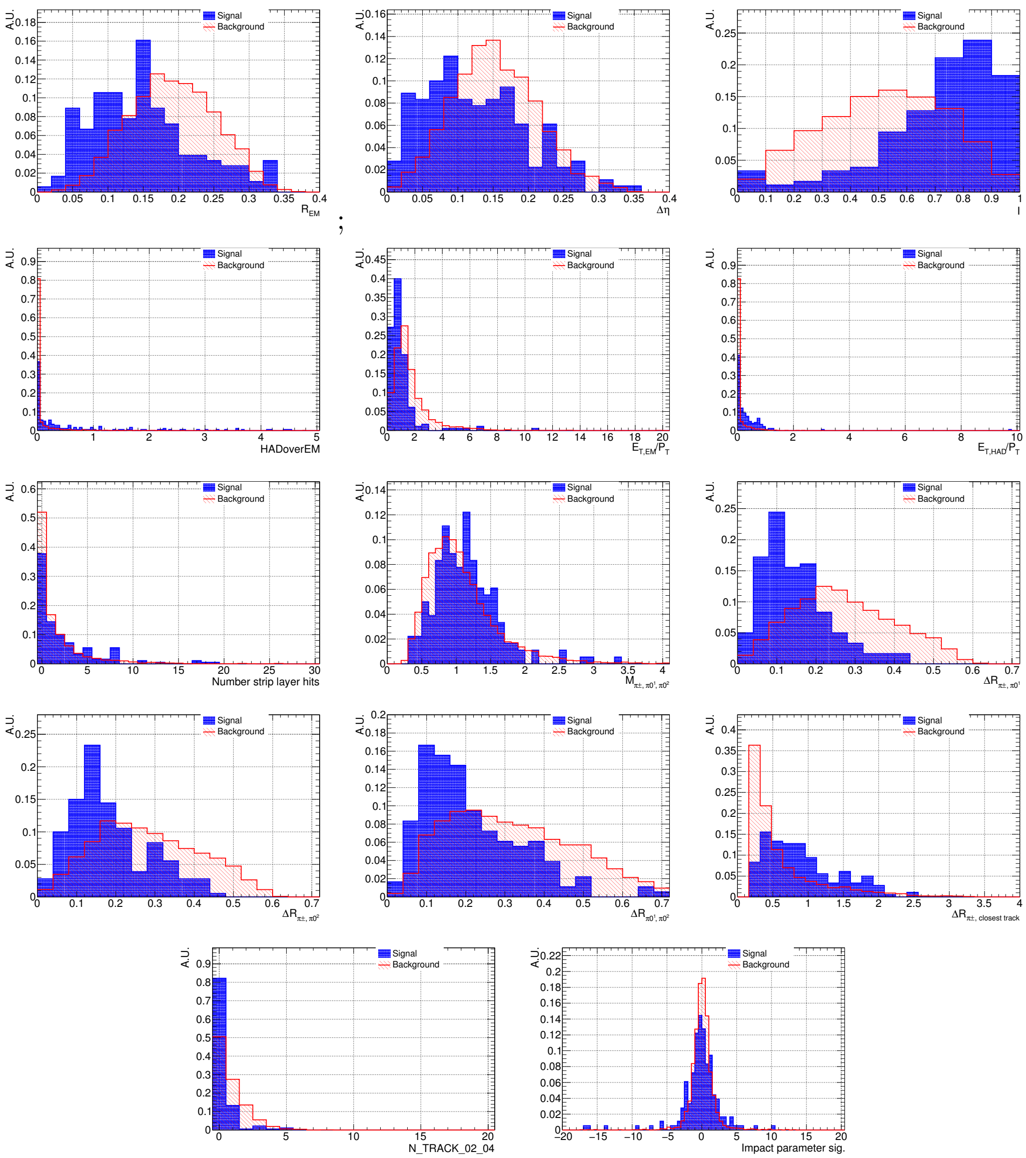

FIGURE B.9: The PDFs used to form the soft tau algorithm likelihood, for the 2-π^0 mode, when the seed track is in the range $p_{track} > 20$GeV.

Appendix C

Systematic study plots

The plots of this appendix relate to the systematic studies of Chapter 7.

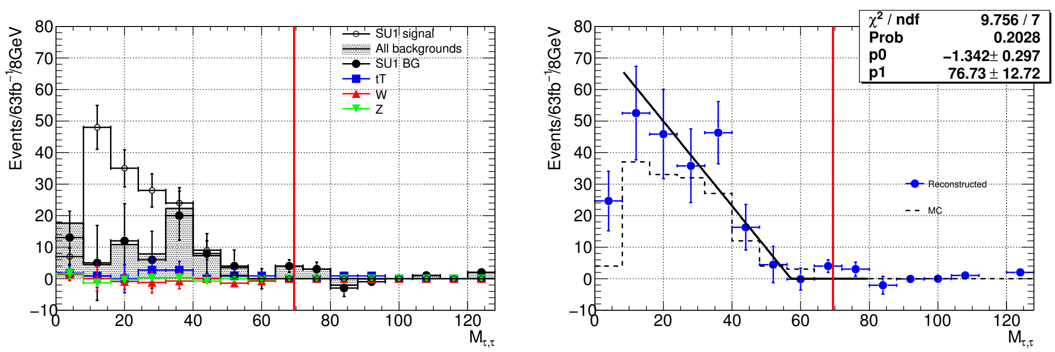

FIGURE C.1: Left: The contributions to the $M_{\tau,\tau}$ spectrum from the signal and each of the background processes when the fake rate for the signal hard tau selection is increased as described in Section 7.1.2. Right: The linear fit of the $M_{\tau,\tau}$ distribution.

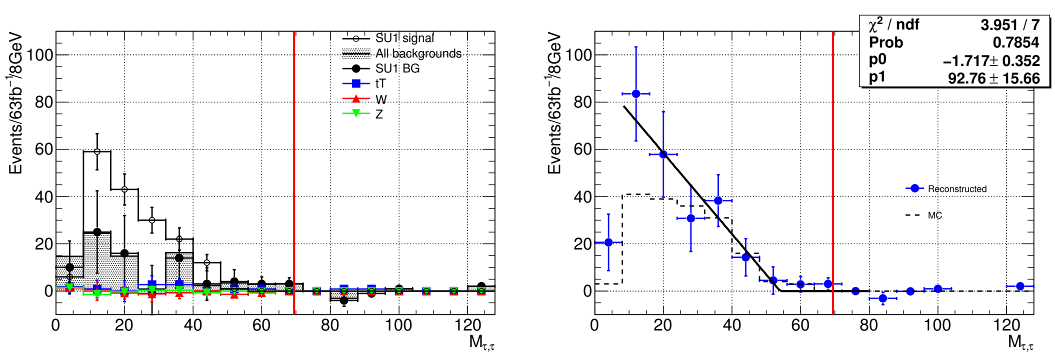

FIGURE C.2: Left: The contributions to the $M_{\tau,\tau}$ spectrum from the signal and each of the background processes when the fake rate for the signal soft tau selection is increased as described in Section 7.1.2. Right: The linear fit of the $M_{\tau,\tau}$ distribution.

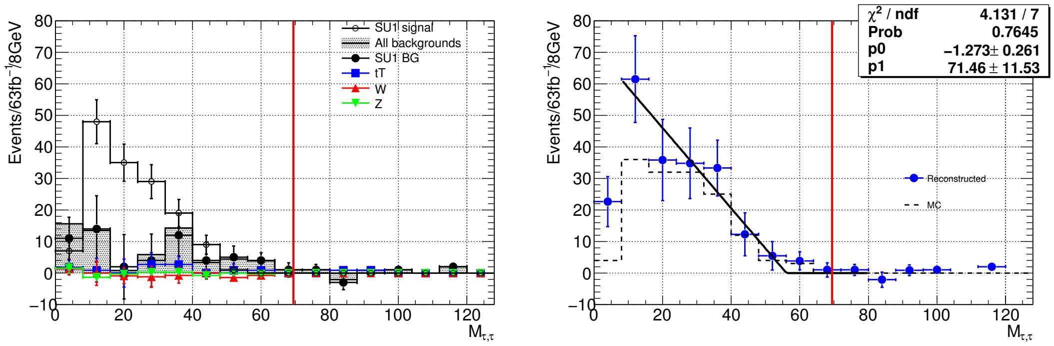

FIGURE C.3: Left: The contributions to the $M_{\tau,\tau}$ spectrum from the signal and each of the background processes when the tau energy scale is decreased as described in Section 7.1.3. Right: The linear fit of the $M_{\tau,\tau}$ distribution.

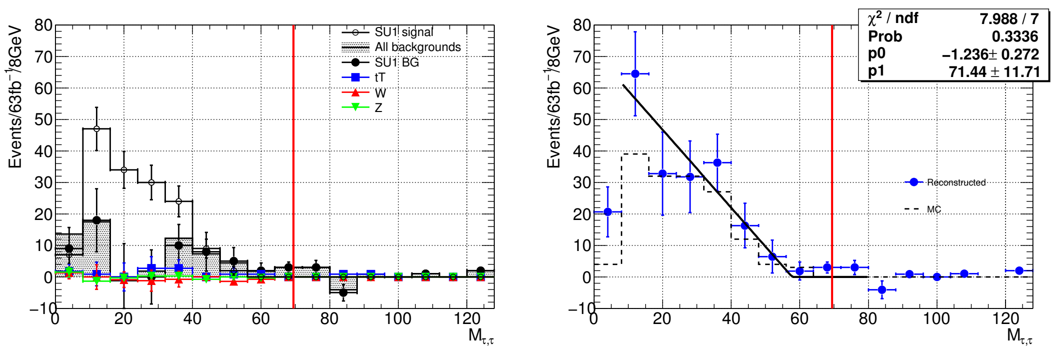

FIGURE C.4: Left: The contributions to the $M_{\tau,\tau}$ spectrum from the signal and each of the background processes when the tau energy scale is increased as described in Section 7.1.3. Right: The linear fit of the $M_{\tau,\tau}$ distribution.

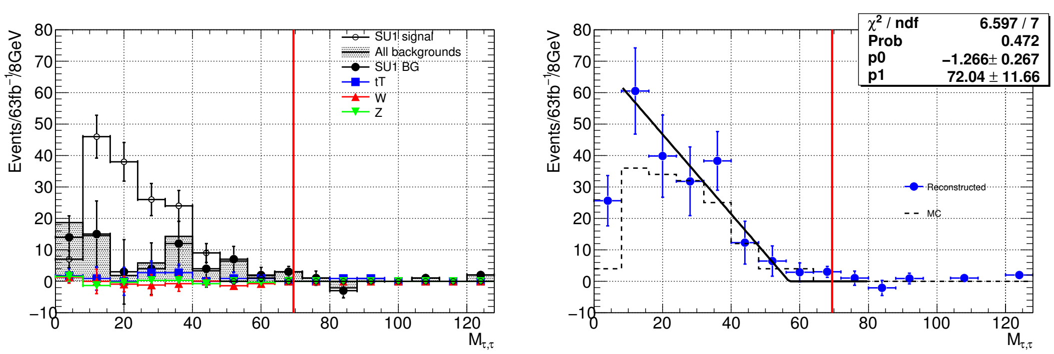

FIGURE C.5: Left: The contributions to the $M_{\tau,\tau}$ spectrum from the signal and each of the background processes when the tau energy resolution is decreased as described in Section 7.1.3. Right: The linear fit of the $M_{\tau,\tau}$ distribution.

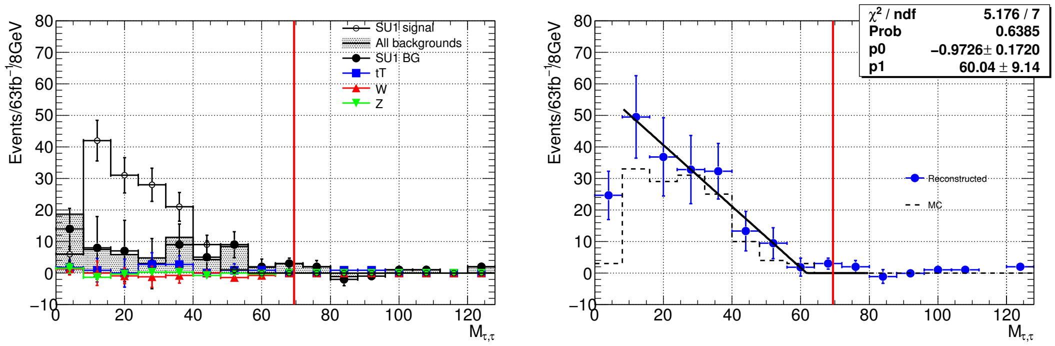

FIGURE C.6: Left: The contributions to the $M_{\tau,\tau}$ spectrum from the signal and each of the background processes when the jet energy scale is decreased as described in Section 7.1.3. Right: The linear fit of the $M_{\tau,\tau}$ distribution.

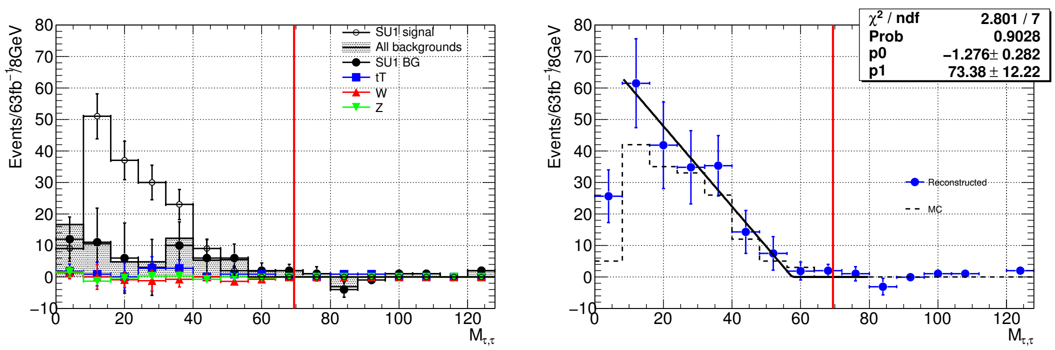

FIGURE C.7: Left: The contributions to the $M_{\tau,\tau}$ spectrum from the signal and each of the background processes when the jet energy scale is increased as described in Section 7.1.3. Right: The linear fit of the $M_{\tau,\tau}$ distribution.

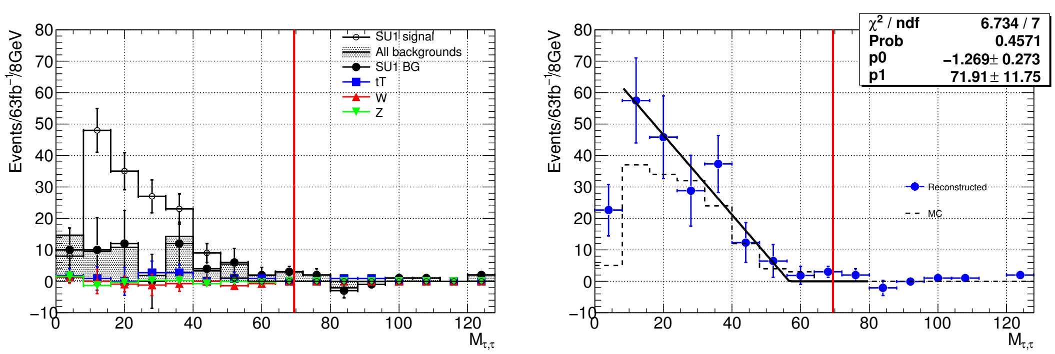

FIGURE C.8: Left: The contributions to the $M_{\tau,\tau}$ spectrum from the signal and each of the background processes when the jet energy resolution is decreased as described in Section 7.1.3. Right: The linear fit of the $M_{\tau,\tau}$ distribution.

Bibliography

[1] Particle Data Group and Kaoru Hagiwara. The review of particle physics. 2009(31 December 2009).

[2] M. L. Perl, G. S. Abrams, A. M. Boyarski, M. Breidenbach, D. D. Briggs, F. Bulos, W. Chinowsky, J. T. Dakin, G. J. Feldman, C. E. Friedberg, D. Fryberger, G. Goldhaber, G. Hanson, F. B. Heile, B. Jean-Marie, J. A. Kadyk, R. R. Larsen, A. M. Litke, D. Lüke, B. A. Lulu, V. Lüth, D. Lyon, C. C. Morehouse, J. M. Paterson, F. M. Pierre, T. P. Pun, and P. A. Rapidis. Evidence for anomalous lepton production in $e + -e-$ annihilation. *Phys. Rev. Lett.*, 35(22):1489–1492, Dec 1975.

[3] S P Martin. A supersymmetry primer. Technical Report hep-ph/9709356, Sep 1997.

[4] C. L. Bennett, M. Halpern, G. Hinshaw, N. Jarosik, A. Kogut, M. Limon, S. S. Meyer, L. Page, D. N. Spergel, G. S. Tucker, E. Wollack, E. L. Wright, C. Barnes, M. R. Greason, R. S. Hill, E. Komatsu, M. R. Nolta, N. Odegard, H. V. Peirs, L. Verde, and J. L. Weiland. First year wilkinson microwave anisotropy probe (wmap) observations: Preliminary maps and basic results. *The Astrophysical Journal*, 148:1, 2003. URL doi:10.1086/377253.

[5] J. Ellis, K. A. Olive, Y. Santoso, and V. C. Spanos. Supersymmetric dark matter in light of wmap. *Physics Letters B*, 565:176, 2003. URL doi:10.1016/S0370-2693(03)00765-2.

[6] . URL http://cdsweb.cern.ch/record/842700.

[7] . URL http://www.atlas.ch/photos/lhc.html.

[8] . URL http://cdsweb.cern.ch/record/843195.

[9] The ATLAS Collaboration and G Aad et al. The atlas experiment at the cern large hadron collider. *Journal of Instrumentation*, 3(08):S08003, 2008. URL http://stacks.iop.org/1748-0221/3/S08003.

[10] ATLAS detector and physics performance. Technical design report. Vol. 2. . CERN-LHCC-99-15.

[11] Dominique J Mangeol and Ulrich Goerlach. Search for neutralino2 decays to tau-stau and susy mass spectrum measurement using di-tau final states. Technical Report CMS-NOTE-2006-096. CERN-CMS-NOTE-2006-096, 2006.

[12] Martin J White and M A Parker. *Searching for Supersymmetry with the ATLAS detector. oai:cds.cern.ch:1112359*. PhD thesis, Cambridge, University of Cambridge, Cambridge, 2006. Presented on 15 Dec 2006.

[13] C G Lester and M A Parker. *Model independent sparticle mass measurements at ATLAS*. PhD thesis, Cambridge Univ., Geneva, 2001. Presented on 12 Dec 2001.

[14] B. K. Gjelsten, 2 Miller, D. J., and P. Osland. Measurement of SUSY masses via cascade decays for SPS 1a. *JHEP*, 12:003, 2004.

[15] *ATLAS computing: Technical Design Report*. Technical Design Report ATLAS. CERN, Geneva, 2005. revised version submitted on 2005-06-20 16:33:46.

[16] W Lampl, S Laplace, D Lelas, P Loch, H Ma, S Menke, S Rajagopalan, D Rousseau, S Snyder, and G Unal. Calorimeter clustering algorithms: Description and performance. Technical Report ATL-LARG-PUB-2008-002. ATL-COM-LARG-2008-003, CERN, Geneva, Apr 2008.

[17] . URL https://twiki.cern.ch/twiki/bin/view/Atlas/SlidingWindowClustering.

[18] . URL https://twiki.cern.ch/twiki/bin/view/Atlas/TopologicalClustering.

[19] T Barillari, E Bergeaas Kuutmann, T Carli, J Erdmann, P Giovannini, K J Grahn, C Issever, A Jantsch, A Kiryunin, K Lohwasser, A Maslennikov, S Menke, H Oberlack, G Pospelov, E Rauter, P Schacht, F Span, P Speckmayer, P Stavina, and P Strzenec. Local hadronic calibration. Technical Report ATL-LARG-PUB-2009-001. ATL-COM-LARG-2008-006, CERN, Geneva, Jun 2008.

[20] . URL https://twiki.cern.ch/twiki/bin/view/Atlas/CalorimeterCalibration.

[21] The ATLAS Collaboration. Expected performance of the atlas experiment: detector, trigger and physics. Technical Report arXiv:0901.0512. CERN-OPEN-2008-020, Geneva, 2009.

[22] A Christov, Z Czyczula, M Janus, L Janyst, A Kaczmarska, A Kalinowski, S Lai, N Meyer, E Richter-Was, and Ch et al. Ruwiedel. Performance of the tau reconstruction and identification algorithm with release 14.2.10. Technical Report ATL-COM-PHYS-2008-196, 2008.

[23] P Bechtle, A C Le Bihan, M Bischofberger, S Brunet, M Bosman, S Cabrera-Urban, D Cavalli, M P Casado, E Coniavitis, D Ct, Z Czyczula, M Dam, W Davey,

S Demers, L Fiorini, D Froidevaux, M Flechl, S Fleischmann, K Grosse-Knetter, M Heldmann, O Igonkina, L Janyst, S Johnert, A Kaczmarska, A Kastanas, S Lai, S Laplace, A Lipniacka, L M Mir, N Moeser, C Osuna, M T Perez Garcia-Estan, E Prez, C Pizio, A Phillips, K Prokofiev, E Richter-Was, Ch Ruwiedel, A Saavedra, T Sjursen, J Tanaka, E Torrence, S Tsuno, A Tonoyan, J B de Vivie de Regie, S Xella, T Vickey, A Watson, P Wienemann, M Wolter, and C Zendler. Identification of hadronic tau decays with atlas detector. Technical Report ATL-PHYS-INT-2008-003. ATL-COM-PHYS-2007-066, CERN, Geneva, Sep 2007.

[24] P.Nevski D.Froidevaux and E.Richter-Was. Energy flow studies for hadronic τs with dc1 data samples. Technical Report ATL-COM-PHYS-2005-024, 2005.

[25] Ola Kristoffer Oye and Anna Lipniacka. Atlas soft tau reconstruction performance in the msugra stau coannihilation region. Technical Report ATL-PHYS-PUB-2006-021. ATL-COM-PHYS-2006-030, CERN, Geneva, May 2006.

[26] K Desch, T Nattermann, P Wienemann, and C Zendler. Measuring the endpoint of the di-tau mass spectrum in neutralino2 decays with the atlas detector at the lhc. Technical Report ATL-PHYS-INT-2008-008. ATL-COM-PHYS-2008-038, CERN, Geneva, Mar 2008.